# DEVELOPMENT OF AN UNDERWATER GLIDER EQUIPPED WITH AN AUXILIARY PROPULSION MODULE

BRIAN CLAUS

# DEVELOPMENT OF AN UNDERWATER GLIDER EQUIPPED WITH AN AUXILIARY PROPULSION MODULE

by

© Brian Claus
Bachelor of Engineering

A thesis submitted to the
School of Graduate Studies
in partial fulfillment of the
requirements for the degree of
Master of Engineering.

Faculty of Engineering and Applied Science
Memorial University of Newfoundland

September 15, 2010

St. John's Newfoundland

# Contents

# Abstract

A low power propeller based propulsion module has been developed to complement the buoyancy engine of a 200 m Slocum electric glider. This device is introduced to allow new behaviours such as horizontal flight and faster overall speeds to expand the existing operational envelope of underwater gliders. The design goal is to match typical horizontal glider speeds of 0.3 m/s while minimising the impact of the module on the performance of the unmodified glider. After careful selection of the propeller and motor candidates the stand-alone propulsion module has been tested in a small flume tank to verify the system's performance. Since the desired flight trajectory is restricted to the horizontal plane the validity of a previously published hydrodynamic model of the glider at zero angle of attack was verified by conducting drag measurements at various flow velocities at full scale in a larger flume tank. Self propulsion tests were also performed to establish the performance of the glider with the new propulsion module in a larger flume tank and in a towing tank. Open water tests were performed in a large test tank to show the stability of the platform for horizontal flight. The results from these tests show that the new propulsion module is capable of driving the vehicle horizontally while matching the performance of the conventional glider.

# Acknowledgements

I would like to thank my supervisor, Dr. Ralf Bachmayer, Paul Winger, George Legge and Tara Perry from the Marine Institute, Jack Foley and Craig Mitchell from Memorial University of Newfoundland (MUN), Chris Williams, Joswin Jeyasuyra and Moqin He of the National Research Council Canada, Paul Lacroix and the Canadian Centre for Ocean Gliders for use of the glider and the Physical Oceanography Department at MUN for providing additional instrumentation and experimental support. This project is supported through funding provided by Natural Sciences and Engineering Research Council, Memorial University of Newfoundland and Suncor-Petro Canada.

# List of Figures

# List of Tables

# Nomenclature

| | |
|---|---|
| $\alpha$ | Angle of attack [$^o$] |
| $\Delta_{bp}$ | Ratio of time ballast pump is active to total profile time [-] |
| $\delta_{bp}$ | Ballast pump delta value [cc/s] |
| $\Delta_{prop}$ | Ratio of time propeller is active to total profile time [-] |
| $\dot{x}$ | Horizontal glider velocity [m/s] |
| $\dot{z}$ | Steady state depth rate [m/s] |
| $\dot{z}_f$ | Nominal depth rate [m/s] |
| $\dot{z}_h$ | Hovering depth rate [m/s] |
| $\dot{z}_{in}$ | Input maximum hovering depth rate [m/s] |
| $\eta_d$ | Propulsive efficiency [%] |
| $\eta_h$ | Hull efficiency [%] |
| $\eta_I$ | Ideal actuator disk efficiency [%] |
| $\eta_{bph}$ | Hydrodynamic efficiency of the buoyancy driven glider [%] |
| $\eta_{bpm}$ | Mechanical efficiency of the ballast pump [%] |

$\eta_{gb}$ Gear box efficiency [%]

$\eta_{mc}$ Magnetic coupling efficiency [%]

$\eta_m$ Motor efficiency [%]

$\eta_p$ Propeller efficiency [%]

$\eta_{sys}$ System efficiency [%]

$\hat{\eta}_{sys}$ Measured system efficiency [%]

$\Omega_m$ Motor speed [RPM]

$\Omega_p$ Propeller speed [RPM]

$\phi$ Vehicle roll [$^o$]

$\rho$ Fluid density [kg/m$^3$]

$\tau_m$ Motor torque [Nm]

$\tau_p$ Propeller torque [Nm]

$\theta$ Pitch angle [$^o$]

$\xi$ Glide-path angle [$^o$]

$A$ Cross sectional area [m$^2$]

$A_p$ Propeller disk area [m$^2$]

$c_0$ Graver lift coefficient linear term [$deg^{-1}$]

$c_1$ Graver lift coefficient square term [$deg^{-2}$]

$c_2$ Graver drag coefficient constant term [-]

$c_3$ Graver drag coefficient square term $[deg^{-2}]$

$c_4$ Williams drag coefficient constant term [-]

$c_5$ Williams drag coefficient square term $[deg^{-2}]$

$C_D$ Drag coefficient [-]

$C_L$ Lift coefficient [-]

$d_p$ Propeller diameter [m]

$d_v$ Vehicle hull diameter [m]

$d_{prop}$ Distance propeller is active during profile [m]

$E$ Energy available [J]

$E_{bpe}$ Electrical energy consumed per up and down profile [J]

$F_B$ Buoyant force [N]

$F_D$ Drag force [N]

$F_g$ Gravitational force [N]

$F_L$ Lift force [N]

$F_m$ Force measured [N]

$F_o$ Force due to measurement aparatus [N]

$F_T$ Thrust force [N]

| | |
|---|---|
| $g$ | Gravitational constant [m/s$^2$] |
| $H$ | Righting moment arm [m] |
| $i$ | Electrical current [A] |
| $i_o$ | No-load electrical current [A] |
| $k_1$ | Torque constant [Nm/A] |
| $k_2$ | Speed constant [RPM/V] |
| $k_3$ | Motor constant [RPM/Nm] |
| $K_\tau$ | Propeller torque constant [-] |
| $p$ | Pressure at depth [kPa] |
| $P_0$ | Ballast pump power linear term [W/m] |
| $P_1$ | Ballast pump power constant term [W] |
| $P_2$ | Electrical propeller power linear term [kg m/s] |
| $P_3$ | Electrical propeller power square term [kg/s] |
| $P_4$ | Electrical propeller power cubic term [kg/m] |
| $P_h$ | Power for vehicle hotel power [W] |
| $P_l$ | Power for vehicle sensor load [W] |
| $p_o$ | Atmospheric pressure [kPa] |
| $P_{bpe}$ | Time averaged electrical power for ballast pump [W] |

$P_{bpi}$ Instantaneous ballast pump power [W]

$P_{bpm}$ Measured ballast pump power [W]

$P_{hyd}$ Hydrodynamic power [W]

$P_{prop}$ Electrical power to the propeller [W]

$Q$ Volumetric rate [$m^3$/s]

$Q^+$ Volumetric rate when volume is increasing [$m^3$/s]

$Q^-$ Volumetric rate when volume is decreasing [cc/s]

$q_0$ Positive volumetric rate constant term [$m^3$/s]

$q_1$ Positive volumetric rate linear term [$m^2$/s]

$q_2$ Negative volumetric rate constant term [$m^3$/s]

$q_3$ Negative volumetric rate linear term [$m^2$/s]

$R_{bp}$ Range for buoyancy driven glider [m]

$R_{hybrid}$ Range for hybrid glider [m]

$R_{prop}$ Range for propeller driven glider [m]

$t$ Thrust deduction factor [-]

$t_{bp}$ Total profile time for ballast driven glider [s]

$t_{prop}$ Time propeller is active during profile[s]

$u$ Electrical voltage [V]

| | |
|---|---|
| $V$ | Volume [$m^3$] |
| $v_A$ | Advance velocity [m/s] |
| $V_B$ | Total ballast pump volume change [$m^3$] |
| $V_o$ | Initial x-hover-ballast [$m^3$] |
| $w$ | Wake fraction [-] |
| $z$ | Vehicle depth [m] |
| $C_{D0}$ | Drag coefficient for zero pitch [-] |
| $C_{Dw}$ | Drag coefficient from Williams et. al [2] [-] |
| $F_{D0}$ | Drag force for zero pitch [-] |

# Chapter 1

# Introduction

## 1.1 Literature Review

### 1.1.1 Underwater Gliders

The conception of underwater gliders was initially motivated by the scientific drive to better understand the subsurface layers of the world's oceans. This desire was shown through initial development of ocean floats by Stommel and Swallow [4], [5]. These floats, through many iterations, developed into the Autonomous Lagrangian Circulation Explorer (ALACE) floats as a part of the world ocean circulation project [6], [7]. Slightly before this, Douglas Webb, who had been heavily involved in the float development, conceived the original concept for an underwater glider as a type of controllable profiling float. Discussions of this concept with Henry Stommel led to their vision of the glider's role in oceanographic research as a portrayal of a future world control centre for gliders [8].

Several years later the first revision of what later became the Slocum glider was developed as a variation of a profiler with controllable fins which allowed for gliding

motions and therefore, a horizontal motion component in addition to the vertical motion component [9]. Webb's original plan was to develop a glider with a thermal engine, capable of harnessing the sharp temperature gradient found in much of the oceans to cause buoyancy differences large enough to sustain gliding motion [10]; however, due to the complicated nature of the thermal engine, electric versions of the Slocum gliders were developed to expedite product development [11], [12], [13]. Concurrent to this development, other notable gliders were developed including the Spray glider at the Scripps Institute for Oceanography and the Sea Glider at the University of Washington [14], [15]. The Spray glider was originally developed as an autonomous profiling float and the Seaglider as a virtual mooring capable of long term monitoring of critical locations. These three gliders were the first commercially available underwater gliders and several articles can be found that outline and compare their abilities [16], [17], [18], [19], [20].

A number of other underwater gliders have been developed for research and development purposes. One of the earliest of these gliders was the ALBAC vehicle designed at University of Toyko [21], [22]. This vehicle uses a drop weight to glide to a maximum depth of 300m where the vehicle releases the drop weight and glides back to the surface. Another glider project at this lab is a simple machine based Mini Underwater Glider (MUG) [23]. This glider is used as an undergraduate student education platform. A more recent research based project from the Osaka Prefecture University is the ALEX vehicle [24], [25]. This vehicle uses independently controllable main wings to achieve a high degree of maneuverability and to increase the glide performance by controlling the angle of attack to the control surfaces.

The ROGUE vehicle was also developed as a laboratory scale glider at Princeton University to validate stability and control models [26], [27]. Additional modelling of control algorithms was based off the ROGUE vehicle in which a model based

feedback control method was developed and tested [28]. Dynamic, stabilisation and coordination mathematical models were also developed using the ROGUE glider [29], [30]. This simulated dynamic model was later extended to the Slocum vehicle using field data to generate a hydrodynamic model [3]. Bachmayer et al., using this model and some recorded data from field trials with the Slocum glider, tuned several of the control loops within the vehicle [31]. A summary of the dynamic modelling work on the Slocum and ROGUE gliders may be found in Graver's thesis [1]. Additional stability and non-linear control methods for underwater gliders from the Princeton University Dynamics and Control Systems group may be found in [32], [33].

A larger hybrid gliding vehicle named STERNE was developed at ENSIETA in France [34]. The plans detailed a vehicle substantially larger than the Slocum gliders, around 1000 kg, capable of travelling faster than many of the other underwater gliders to date and having both ballast control and a propeller. For testing, a 1/3 scale laboratory version of the vehicle was built which was around the same size as the Slocum gliders.

Several other hybrid glider developments include the AUV-glider and the Folaga glider [35], [36], [37]. The AUV-glider was developed at the Florida Institute for Technology as hybrid between the long endurance buoyancy driven gliders and propeller based Autonomous Underwater Vehicles (AUVs). This vehicle weighs about 300 kg with an endurance of approximately 150 hrs and an optimal speed of 2 knots. The Folaga glider was developed as a very low cost system which drives at or near the surface using a propeller with intermittent profiles using a ballast system. The Folaga vehicle weighs about 30 kg with an endurance of around 8 hrs and a top speed of 2 knots. Additional work has been done with the Folaga vehicle for multi-vehicle cooperative missions, adaptive environmental sampling missions as well as hull optimisation for near surface operation of submerged vehicles in waves [38], [39], [40].

A more recent commercial glider development is the Sea Explorer by ACSA Underwater GPS. The Sea Explorer is an underwater glider with acoustic navigation that has an optional propeller based propulsion module to make a hybrid type glider [41]. The vehicle is still in development and expected to have an endurance on the order of months and weigh about 60 kg.

The Liberdade/X-ray is another glider configuration that is in development. This vehicle is a blended wing/body type glider that makes use of the flying wing concept [42], [43]. To generate sufficient lift for this configuration the wing must be larger than that of vehicles mentioned previously making this glider the largest at a wingspan of 6 m. The vehicle is to be capable of speeds of up to 3 knots with an endurance of months and a range of over 1000 km.

Another variation on a gliding vehicle is the Wave Glider by Liquid Robotics. The wave glider uses a surface buoy coupled to a large gliding submerged body to harvest wave motion and propel itself forwards. In this way the vehicle has no electric propulsive load and maintains a speed relative to the mean wave height [44]. A recent application of this technology in the form of a buoy replacement was met with success where the Wave Glider was able to stay on station at all times with the exception of extreme winds. In this situation the vehicle was still able to recover its position after the weather event [45].

Throughout the development cycle of these first underwater gliders there has been significant interest by the Navies in various countries. In 2003, directly after the three Office of Naval Research (ONR) funded Slocum, Sea Glider and Spray glider programs finished, a glider systems study was performed and compiled for ONR [20]. Shortly after the completion of this study, ONR announced a contract for over a hundred gliders prompting iRobot to exclusively license the Sea Glider, Teledyne to purchase Webb Research and Bluefin Robotics to license the Spray [46]. In early

2009 Teledyne Webb Research announced that it had been successful in its bid for the contract [47]. This contract has lead to significant developments with the Slocum glider to harden the system to military specifications leading to the second generation of Slocum gliders, the Slocum G2.

Another primary motivator for development of gliders and glider related technologies has been the scientific community [48]. The most prevalent uses in science have been in Physical Oceanography where they have been used as profilers, gathering salinity, density and temperature information through conductivity, temperature and density (CTD) sensors. Many publications have been dedicated to the correction and interpretation of this data as the vehicles use a non-pumped CTD sensor which presents time-lag errors and challenges with dynamic measurements which vary in space and time [49]. Additional popular sensors include dissolved oxygen sensors, backscatter sensors, turbulence meters, Acoustic Doppler Current Profilers, various sonar devices and hydrophones to name a few.

### 1.1.2 Long Range AUVs

It is interesting to note that Autonomous Underwater Vehicles (AUVs) and gliders developed to meet different needs and markets while still being underwater vehicles. Only recently have some of the roles of AUVs and underwater gliders begun to merge. One notable example of this is the Long Range Autosub (LRA) 6000 AUV which extends the Autosub 6000 architecture to a version with a range of 6000 km [50], [51]. Previously, vehicles with a range of over 1000 km were exclusively the domain of underwater gliders. This transition is motivated by the desire to push the boundaries of the types of missions possible with underwater vehicles. The LRA is scheduled for field testing in January 2011 with some possible missions including traversing

beneath the arctic ice cap and in the strong current region of the drake passage between Antarctica and South America [52]. Additional work comparing gliders and AUVs is presented in Steinberg et. al's work in which an analytical comparison between the normalised transit efficiencies is presented [53].

### 1.1.3 Under-Ice AUVs

There have been a small number of AUVs which have specialised in under-ice missions. The most notable of these from a Canadian perspective is the Theseus AUV from International Submarine Engineering [54]. The Theseus vehicle was developed on contract from the Defense Research Establishment Atlantic of the Canadian Department of National Defense to lay fibre-optic cables in ice covered waters [55]. Initially developed to have a range of around 400 km, it has evolved to being capable of a range of over 1360 km with a depth rating of 2000 m [56]. The Theseus vehicle remains one of the few AUVs specifically designed and successfully used in under-ice deployments. The success of the Theseus vehicle has prompted under-ice missions with the MUN-Explorer vehicle in 2009 [57]. These missions came as a precursor to two additional explorer class vehicles being contracted by the Canadian government for use in under-ice survey of the Canadian arctic ridge to establish Canada's claim to the Commission on the Limits of the Continental Shelf through the United Nations Convention on the Law of the Sea [58]. These vehicles are presently doing survey work to meet the deadline for claims of 2013.

The Autosub Under-Ice program is another notable under-ice AUV exploration program. The Autosub under-ice program was a 5-year program funded by the National Environment Research Council in the United Kingdom to bring together scientists and engineers to study ice-shelf and ocean interactions and the impact they

have on the climate. This program has collected the most data to date on under-ice properties in arctic waters [59], [60]. The use of the Autosub platform for under-ice missions also prompted significant investigation into under-ice AUV risk of loss assessment after the loss of one of the Autosub vehicles [61].

### 1.1.4 The Autonomous Ocean Systems Lab

The Autonomous Ocean Systems Lab (AOSL) at Memorial University of Newfoundland (MUN) focuses on the development of ocean technologies related to scientific and industrial needs. Current research projects include a highly maneuverable yet stable AUV platform for high resolution sonar bathometry being developed in conjunction with Marport Canada and the National Research Council Institute for Ocean Technology [62]; the hybrid glider and the subject of this thesis [63]. [64]; the integration and data correction for a glider outfitted with an acoustic doppler current profiler (ADCP) [65]; using an upwards facing altimeter for ice profiling work with an underwater glider [66]; an autonomous surface vessel for glider launch and recovery and a glider outfitted with acoustic transponders for localisation. These projects bring together many of the different specialised commercial, provincial and federal interests in ocean technology in Canada and help to generate public interest and awareness of ocean related issues.

## 1.2 Motivation and Scope of Work

Over the last ten years autonomous underwater gliders have become increasingly useful for oceanographic research because of their ability to lower operational expenses, increase range and endurance [18]. Gliders use an active buoyancy control system combined with a set of fixed wings to move vertically and horizontally, in a saw tooth

like pattern through the water column [15], [14], [10]. The endurance of these underwater vehicles varies from weeks to several months and even longer in the case of the thermal glider [10]. In contrast, currently available propeller driven autonomous underwater vehicles (AUVs) achieve an endurance ranging from hours to days. This stark contrast can mostly be attributed to a purpose built system and to the low speed at which the gliders move [67] and [68]. Gliders typically move at horizontal speeds of about 0.3 m/s compared to propeller driven AUVs which typically move at average speeds greater than 1.0 m/s. The low speed capability can create significant problems when operating in areas of strong water currents which exceed the glider's maximum forward speed. If the direction of the currents is known *a priori* or measured *in situ* [69] the missions can be designed to either avoid these areas or to take advantage of them. In this case the operator must redirect the glider to better deal with the current by moving away from that region or, in the case of significant vertical stratification, try to operate below/above the expected layer of highest lateral velocities. However, in the case of unknown currents they can pose a significant risk to the successful execution of the mission plan. These issues have given rise to the idea of the hybrid glider which combines the gliding behaviours of traditional underwater gliders with the propeller driven behaviours of AUVs.

This thesis addresses the design and testing of an auxiliary propulsion module for the Slocum class of underwater gliders. The objectives of the project are to enable the glider to move horizontally at the nominal glider speed of 0.3 m/s and, for short periods of time, to double its horizontal speed to approximately 0.6 m/s. To this end a simplified mathematical model of underwater gliders as well as a model for the Slocum 200 m glider ballast pump power consumption based on experimental data are described. These two models are used to develop design constraints and initial component selection. The design and testing process for the propeller and motor

are presented during which the final configuration is shown. Following this, the mechanical, electrical and software integration of the module into the existing glider is discussed. The system testing and evaluation including experimental results from full-scale tests in the Marine Institute (MI) of Memorial University of Newfoundland (MUN), tow tank self-propulsion tests in the Ocean Engineering Research Centre at MUN and open water flight tests in the Ocean Engineering Basin (OEB) at National Research Council's Institute for Ocean Technology are presented. A range model for a hybrid glider is developed based on the combination of an AUV range model and the hydrodynamic model for the glider. The last section summarises the results of the design and evaluation phase of the hybrid glider and gives an overview of the next steps in the development of the hybrid glider towards a fully operational system.

# Chapter 2

# Vehicle Modelling

A model of the vehicle is presented to facilitate the design and analysis of the new propulsion module. The hydrodynamic model is based on a previously published hydrodynamic model and the ballast pump model is derived using experimental data.

## 2.1 Hydrodynamic Modelling

The full six degree of freedom hydrodynamic model for an underwater glider is simplified due to the assumption of steady state conditions for the vehicle. This assumption is justified as a well ballasted gliding underwater vehicle spends the majority of its time at steady state. Most of the hydrodynamic modelling to date for underwater gliders has assumed steady-state glides and extrapolated parameters based on a combination of measured data and theoretical calculations. For a glider with angles and forces as defined in Fig. 2.1 the simplified steady state equations of motion in the vertical plane may be written as

$$\begin{pmatrix} F_L\cos(\xi) + F_D\cos(\xi) \\ F_L\sin(\xi) + F_D\sin(\xi) + F_g - F_B \end{pmatrix} = \begin{pmatrix} 0 \\ 0 \end{pmatrix} \tag{2.1}$$

where $\xi$ is the glide-path angle, $F_L$ is the hydrodynamic lift, $F_D$ is the hydrodynamic drag, $F_g$ is the gravitational force and $F_B$ is the buoyant force. The lift and drag force may then be defined as [3]

$$F_L = \frac{1}{2}\rho A C_L(\alpha) v_A^2 \tag{2.2}$$

$$F_D = \frac{1}{2}\rho A C_D(\alpha) v_A^2 \tag{2.3}$$

where $\alpha$ is the angle of attack, $\theta$ is the pitch angle defined as $\theta = \xi - \alpha$, $\rho$ is fluid density, $A$ is the cross sectional area and $v_A$ is the advance velocity. In [3] the authors present the hydrodynamic model parameters for a Slocum 200 m underwater glider. From (2.2) the lift coefficient $C_L(\alpha)$ based on frontal area is determined as

$$C_L = c_0\alpha + c_1\alpha|\alpha| \tag{2.4}$$

and similarly from (2.3) the drag coefficient $C_D(\alpha)$ as

$$C_D = c_2 + c_3\alpha^2 \tag{2.5}$$

where the coefficients from (2.4) and (2.5) are defined as in Tab. 2.1

For the purposes of the propulsion module design the glider was assumed to be ballasted neutrally buoyant, trimmed for level flight at pitch angle $\theta = 0^o$ and moving at a constant speed. These assumptions do not hold for regular glider operations but for the initial design purpose they provide a starting point while significantly simplifying the lateral plane hydrodynamic model of gliders as presented in [28]. As a result of the assumed pitch angle $\theta = 0^o$, the glide-path angle $\xi = 0^o$ and

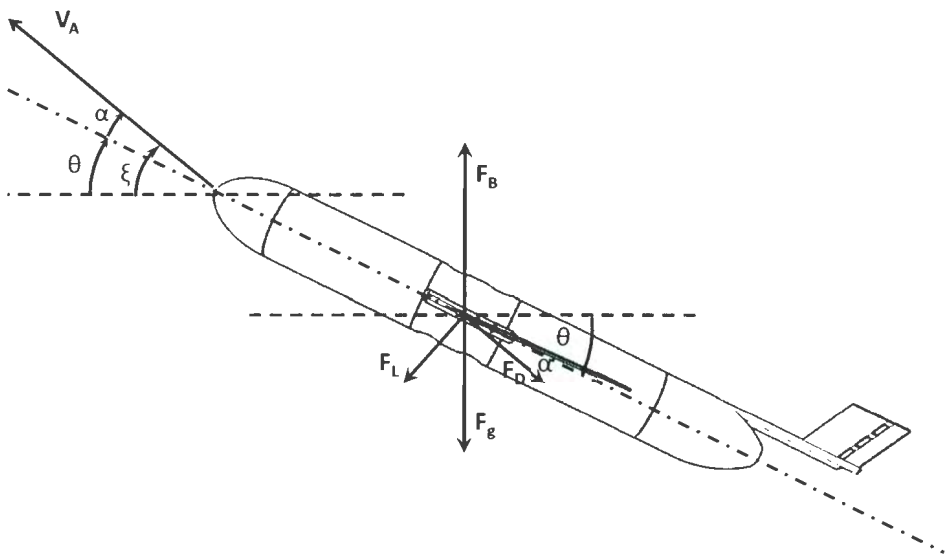


Figure 2.1: Schematic of an autonomous underwater glider in the vertical plane defining the angles relevant to the glider's path during steady state glides.

| | |
|---|---|
| $c_0$ | 11.76 $deg^{-1}$ |
| $c_1$ | 4.6 $deg^{-2}$ |
| $c_2$ | 0.214 |
| $c_3$ | 32.3 $deg^{-2}$ |

Table 2.1: Hydrodynamic lift and drag coefficients for the model taken from Graver et al. [3]

therefore the angle of attack $\alpha = 0^o$ as well. Under the assumption of constant velocity, there is no acceleration, therefore added mass effects can be neglected and the equation of motion (2.1) is reduced to the balance of the drag force $F_D$ and the thrust generated by the propulsion module. Due to the assumption of a zero angle of attack ($\alpha = 0^o$) the hydrodynamic model simplifies to a drag only model. From (2.5) $C_D(\alpha = 0) = C_{D0} = c_2$ such that

$$F_{D0} = \frac{1}{2}\rho A C_{D0} v_A^2 \tag{2.6}$$

This simplified hydrodynamic model provides the vehicle drag force for a given advance velocity to the propulsion module design cycle, establishing the operating parameters for the propeller and motor. Additionally, the model provides an estimate of the hydrodynamic power requirements. The hydrodynamic power may be coupled with the electrical input power of the ballast system and propulsion module to give a measure of the transport efficiency. The transport efficiency for the buoyancy driven glider may then be compared with the propeller driven glider.

## 2.2 Ballast Pump Modelling

The ballast pump is the device responsible for changing the volume of the glider, causing the net buoyancy to be positive or negative and subsequently causing the vehicle to glide upwards or downwards. It is the propulsive motive force for a gliding vehicle. In this section a model is developed for the buoyancy engine based on experimental data that captures the electrical and mechanical changes. This model is used for a comparison between the buoyancy driven vehicle and the propeller driven vehicle. To establish the power usage of a buoyancy driven glider, the power to the ballast pump was monitored during a mission with a variety of depths of profiles. A

subset of the data recorded in this mission is shown in Fig. 2.2.

During a mission the ballast pump turns on only at the inflection points of a profile, at either the deepest or shallowest points of the profile. From these measurements the instantaneous electrical power for a given depth may be plotted as in Fig. 2.3, establishing the load line for the pump as a function of depth as in

$$P_{bpi} = P_0 z + P_1 \tag{2.7}$$

where $z$ is the glider depth and the coefficients for (2.7) are defined as in Tab. 2.2

| | |
|---|---|
| $P_0$ | 0.3 W/m |
| $P_1$ | 8.2 W |

Table 2.2: Instantaneous ballast pump power coefficients

The mechanical power output by the ballast pump $P_{bpm}$ may be defined as

$$P_{bpm} = p(z)Q \tag{2.8}$$

where $p$ is the pressure at depth and $Q$ is the volumetric rate. The volumetric rate is found by taking the time derivative of the volume of ballast pumped $V$ as in

$$Q = \frac{d}{dt}V \tag{2.9}$$

The computed volumetric rate is plotted in Fig. 2.4 for the Bonavista 2009 mission where the volume is increasing. The rate is shown to decrease with depth when the volume is increasing, i.e., the glider is coming back to the surface.

$$Q^+ = q_0 - q_1 z \tag{2.10}$$

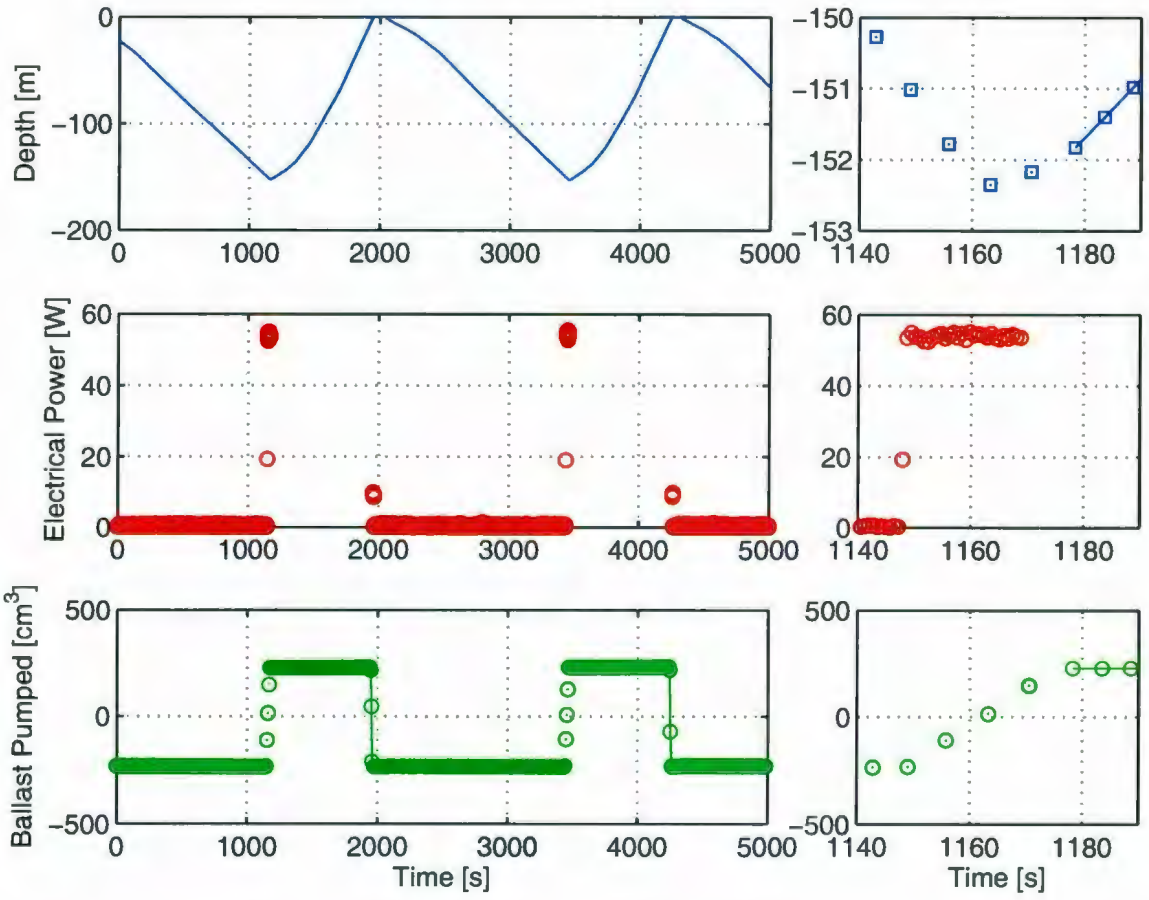


Figure 2.2: Ballast pump power monitoring from a mission out of Bonavista, Newfoundland on June 17th, 2009 where the left is a subset of the data showing the depth, ballast pump power and measured ballast pumped and the right is a close up of a deep inflection point where the ballast pump is on

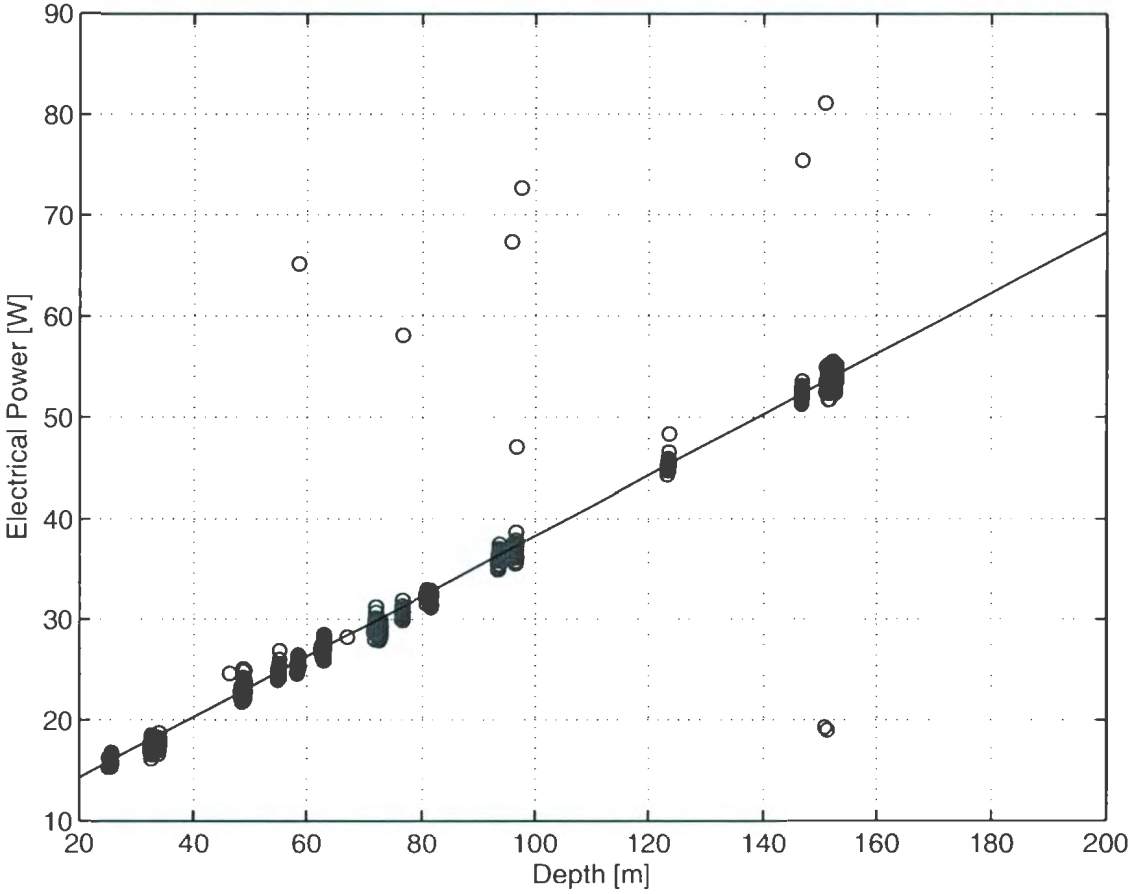


Figure 2.3: Instantaneous ballast pump power at given depth z. The outliers are due to the motor startup current.

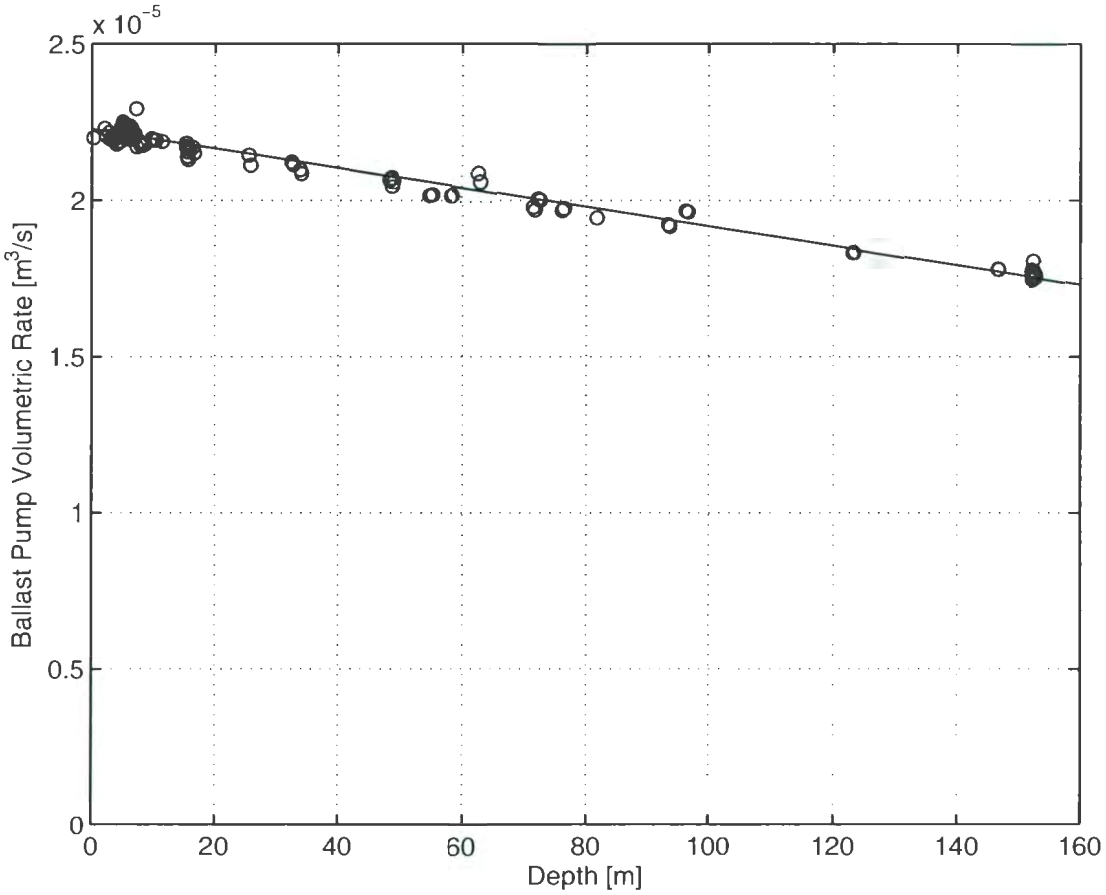


Figure 2.4: Ballast pump volumetric rate for a given depth computed from the Bonavista 2009 mission while at depth where the volume is increasing.

where $Q^+$ is the volumetric rate when the volume is increasing determined using a least squares fit. The coefficients for (2.10) are shown in Tab. 2.3

| | |
|---|---|
| $q_0$ | 2.228E-5 $m^3/s$ |
| $q_1$ | 3.1E-8 $m^2/s$ |

Table 2.3: Positive volumetric rate coefficients

The volumetric rate for the ballast system when the glider is decreasing its volume and at the surface, i.e., about to dive, may be extracted from Fig. 2.5 as in

$$Q = q_2 - q_3 z \tag{2.11}$$

where $Q^-$ is the volumetric rate when the volume is decreasing and the coefficients for (2.11) are shown in Tab. 2.4

| | |
|---|---|
| $q_2$ | 2.45E-5 $m^3/s$ |
| $q_3$ | 0 $m^2/s$ |

Table 2.4: Negative volumetric rate coefficients

The increase in volumetric rate at $z = 0$ for $Q^-$ over $Q^+$ is attributed to the internal vacuum in the vehicle as the ballast pump must work against it to expand the vehicle's volume. It is expected that $Q^-$ will take a form similar to $Q^+$; however, the glider's shallow inflection point was always set to be 3 m for these tests resulting in insufficient data to determine $q_3$. The pressure at depth is defined to be

$$p = p_o + \rho g z \tag{2.12}$$

where $p_o$ is atmospheric pressure, $g$ is the gravitational acceleration and $z$ is water depth defined as positive downwards. The time averaged electrical power $P_{bpc}$ is then

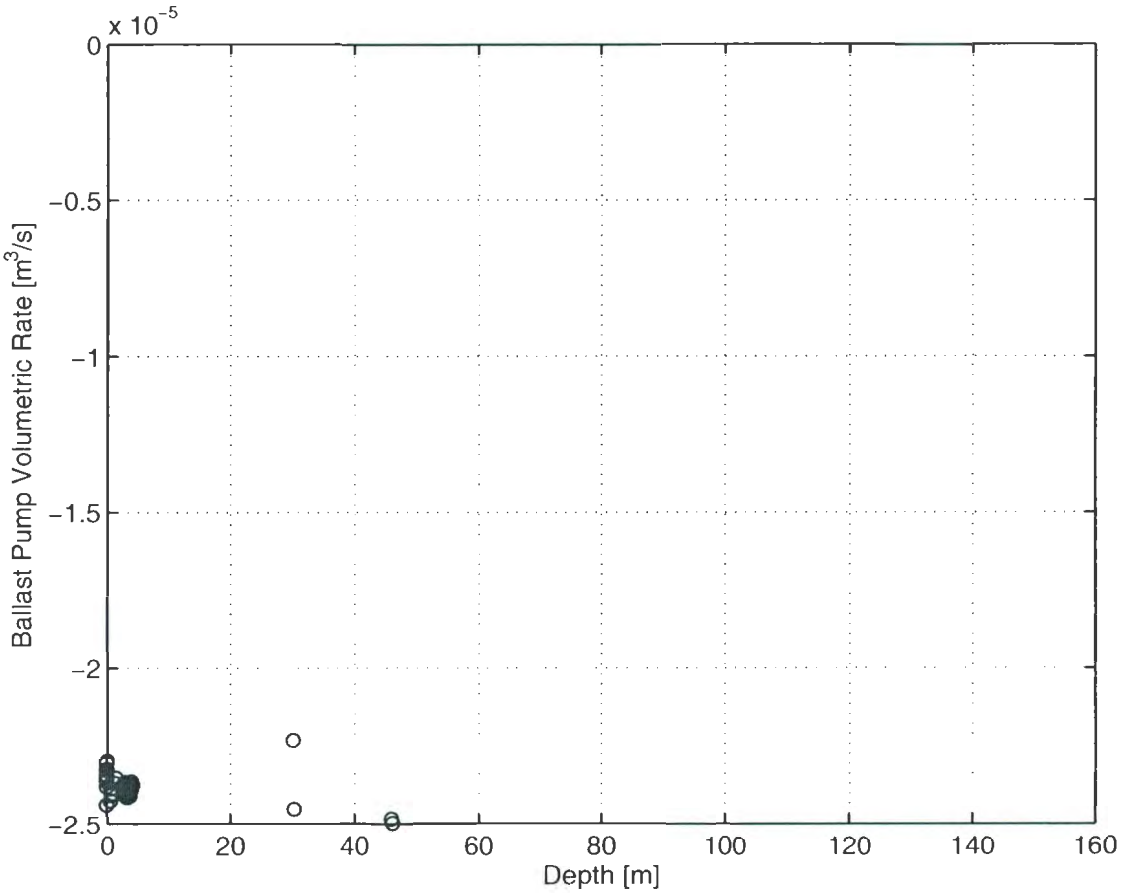


Figure 2.5: Ballast pump volumetric rate for a given depth computed from the Bonavista 2009 mission while at depth where the volume is decreasing.

given by converting the instantaneous power to energy consumed per up and down profile $E_{bpe}$ with one use of the buoyancy pump at the surface and one at depth, and dividing by the total profile time $t_{bp}$ as in

$$E_{bpe} = (P_0 z + P_1)\frac{V_B}{Q^+} + P_1\frac{V_B}{Q^-} \tag{2.13}$$

$$P_{bpe} = \frac{E_{bpe}}{t_{bp}} \tag{2.14}$$

Here the shallow inflection depth is assumed to always be at the surface $z = 0$ and the time used to compute the ballast pump electrical energy $E_{bpe}$ is found by dividing the total volume change $V_B$ by the volumetric rate $Q$ where $V_B$ = 4.50E-4 $m^3$. The on-time for the ballast pump was computed using the volumetric rate to remove the aliasing errors due to the slow sampling rate of the glider. The total cycle time $t_{bp}$ can be measured from the mission data, however, extended periods at the surface and the bottom for many of the profiles made it difficult to accurately estimate this value. Therefore, the steady state depth rate was used to estimate the glide time as a function of depth for half a profile as in

$$t_{bp} = \frac{\dot{z}}{z} \tag{2.15}$$

where the steady state depth rate $\dot{z}$ was calculated from the measured values shown in Fig. 2.6.

From Fig. 2.6 it is evident that there is a significant miss-trim in the vehicle due to the difference between the descending and ascending steady state depth rates of $\dot{z} = 0.1187$ m/s and $\dot{z} = 0.2657$ m/s. To calculate the depth rate the average between the descending and ascending steady state depth rates of $\dot{z} = 0.1187$ m/s and $\dot{z} = 0.2657$ m/s was taken to give $\dot{z} = 0.1922$ m/s. From a plot of the steady state

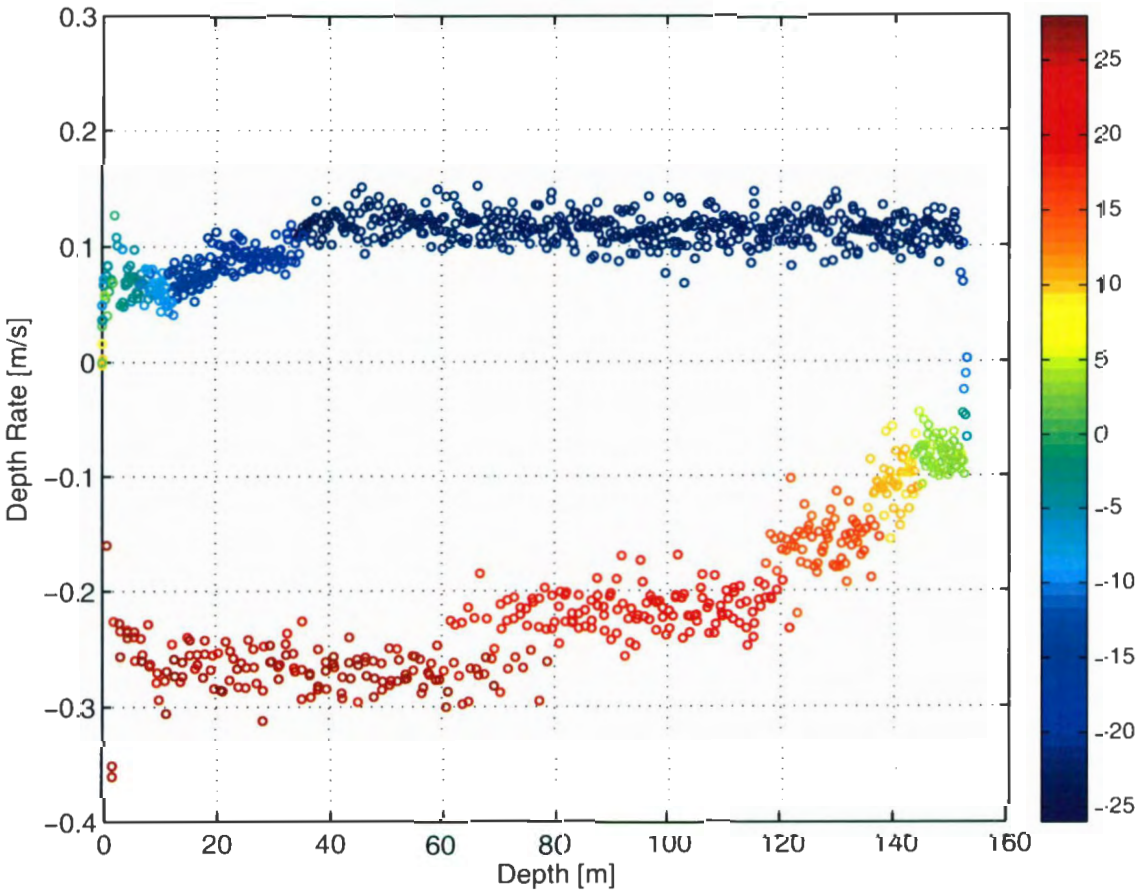


Figure 2.6: Depth rate $\dot{z}$ for a given depth $z$ with the pitch shown as the marker colour gradient for five profiles to 150 m taken from the Bonavista 2009 mission

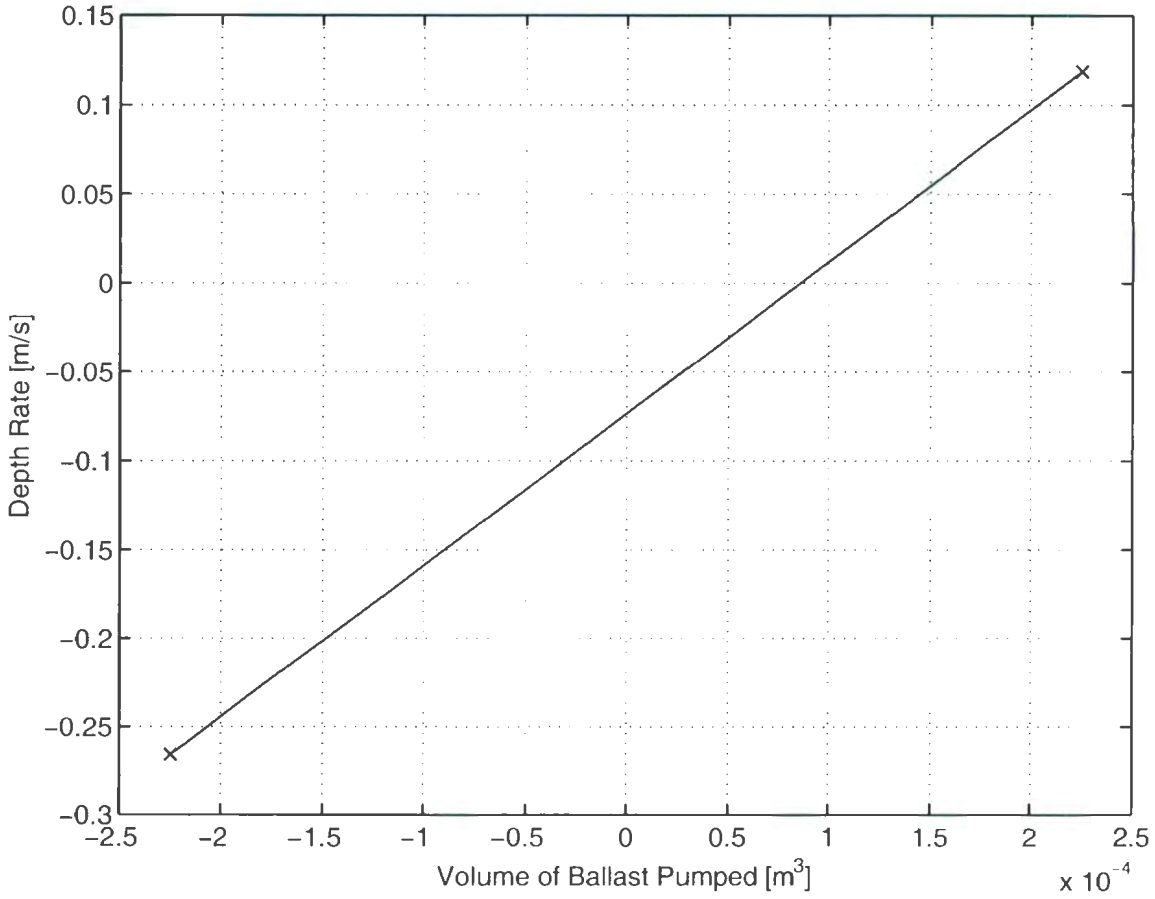


Figure 2.7: Line connecting the ascending and descending steady-state depth rate as a function of the ballast pumped showing the ballast adjustment required.

depth rate and the ballast pumped the mass change required for an ideally trimmed vehicle may be obtained as in Fig. 2.7. An ideally ballasted vehicle has zero depth rate for zero ballast pumped, therefore, the ballast change required is found where the depth rate is zero and is equal to 8.6E-5 $m^3$ for the Bonavista mission.

The resultant time averaged ballast pump electrical power $P_{bpe}$ is shown in Fig. 2.8. The focus in developing the ballast pump model has been on the time averaged electrical power rather than the energy consumption. This focus on the time averaged power is presented for ease of comparison to a continuous load.

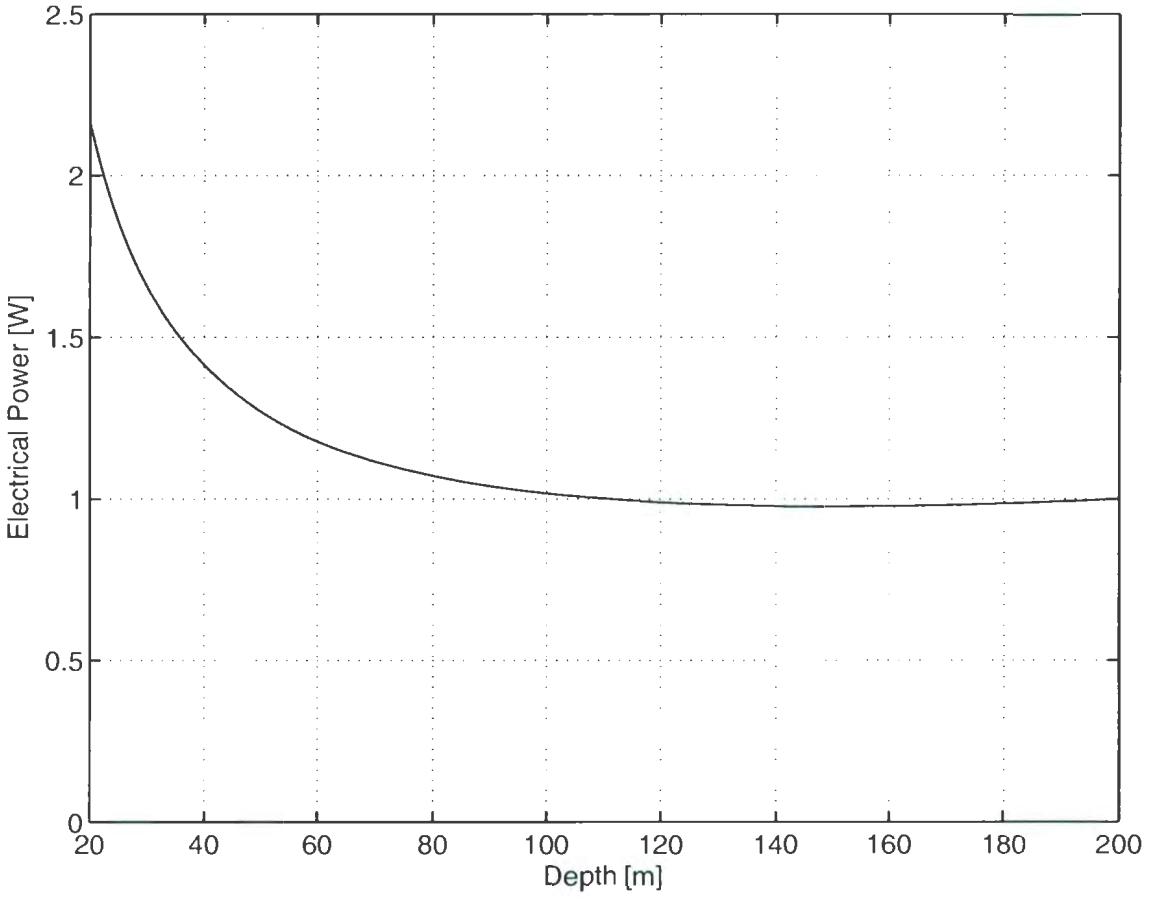


Figure 2.8: Time averaged electrical input power to the ballast pump for a given depth of profile.

## 2.3 Glider Efficiency Modelling

The transport efficiency is an effective way of comparing the overall effectiveness of the buoyancy and the propeller based propulsive methods. To estimate the efficiency of the glider we can use the geometric relationship defined in Fig. 2.1 between the glide path angle $\xi$ and the vertical velocity of the glider $\dot{z}$ to determine the advance velocity $v_A$ as

$$v_A = \frac{\dot{z}}{sin(\xi)} \tag{2.16}$$

and the horizontal velocity $\dot{x}$ as

$$\dot{x} = \frac{\dot{z}}{tan(\xi)} \tag{2.17}$$

The hydrodynamic power may then be calculated using (2.3), (2.5) and (2.16) as in

$$P_{hyd} = F_D v_A \tag{2.18}$$

A measure of the hydrodynamic efficiency of the buoyancy driven glider $\eta_{bph}$ may be estimated using (2.14) and (2.18) as in

$$\eta_{bph} = \frac{P_{hyd}}{P_{bpe}} \tag{2.19}$$

Additionally, the mechanical efficiency of the ballast pump $\eta_{bpm}$ may be calculated using (2.14) and (2.8) as in

$$\eta_{bpm} = \frac{P_{bpm}}{P_{bpe}} \tag{2.20}$$

The efficiency and time averaged power results are plotted in Fig. 2.9 with an assumed angle of attack $\alpha = 2.9^o$ [3].

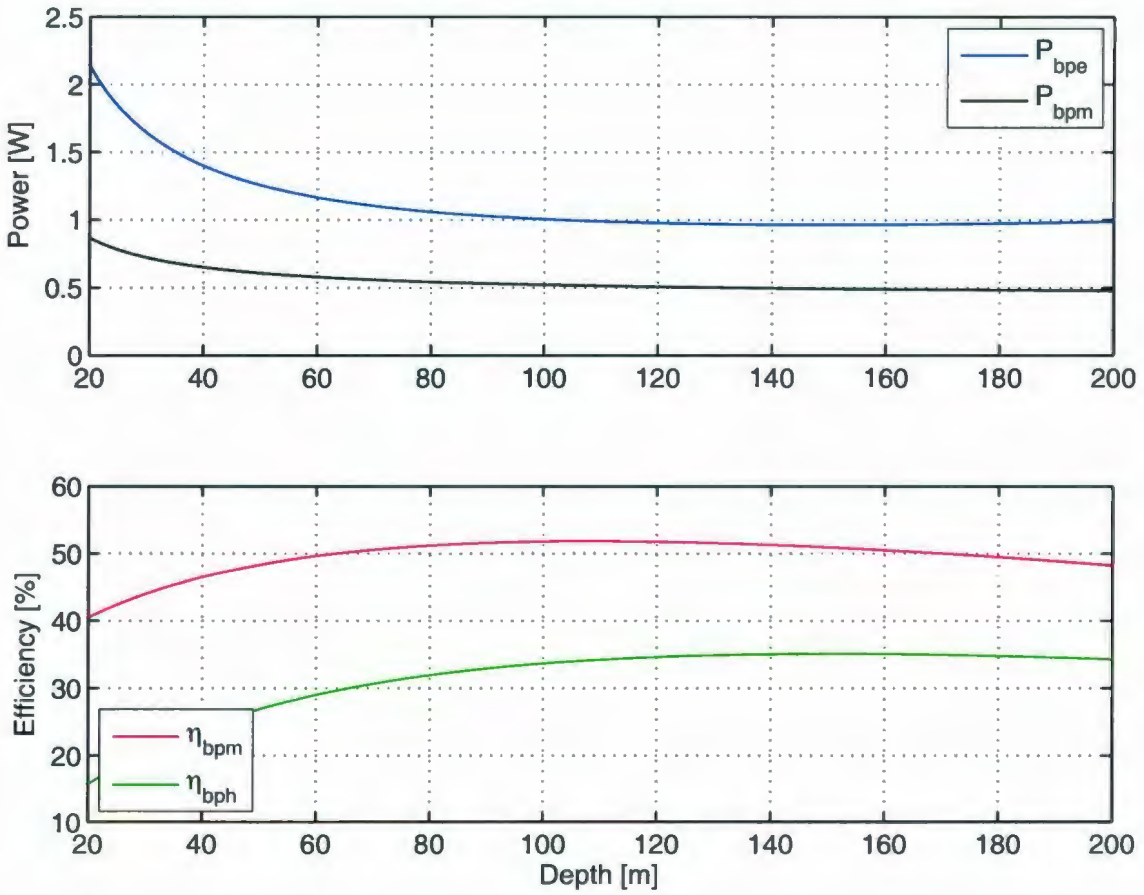


Figure 2.9: Ballast pump power and efficiency for Graver's Slocum glider hydrodynamic model [1]

| | |
|---|---|
| $c_4$ | 0.2175 |
| $c_5$ | 6.36 $deg^{-2}$ |

Table 2.5: Hydrodynamic drag coefficients for the model taken from Williams et al. [2]

An additional hydrodynamic model presented by Williams et. al [2] presents the drag coefficient from field data that is different from (2.5) as

$$C_{Dw} = c_4 + c_5\alpha^2 \tag{2.21}$$

where the coefficients for (2.21) are defined as in Tab. 2.5

The $c_4$ coefficient in this model is significantly less than $c_2$ in (2.5) due to the author assuming a larger angle of attack than in Graver's model [1]. The efficiency and time averaged power results for the Williams model are plotted in Fig. 2.10 with an assumed angle of attack $\alpha = 6.53^o$ [2].

The $\eta_{bph}$ is less in William's model than in Graver's model. This difference is attributed to the difference in the glide path angle $\xi$ due to the different assumed angle of attack $\alpha$. Since the depth rate $\dot{z}$ is fixed from the data from the Bonavista 2009 ballast pump power trials, the glider advance velocity $v_A$ is larger in the Graver model resulting in a larger drag force $F_D$ for the same electrical power. This difference also highlights the dependance of the drag coefficient from Graver and Williams on parameters other than $\alpha$.

To summarise, the mechanical efficiency of the ballast pump is presented as a function of depth and is independent of the hydrodynamic model. The hydrodynamic efficiency of the gliding vehicle is presented and is shown to be dependant on the hydrodynamic model used. Several hydrodynamic models have been presented to date, however, the two models used [3], [2] do not match well resulting in a different

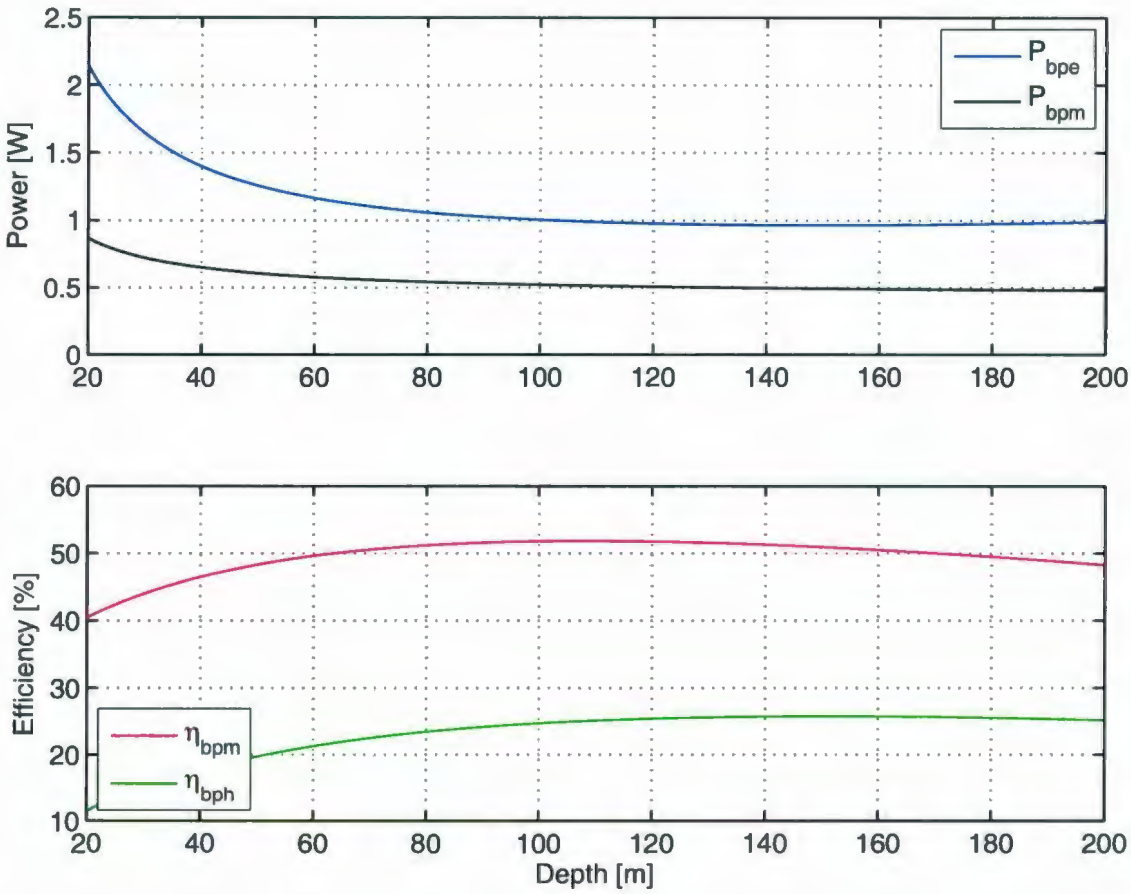


Figure 2.10: Ballast pump power and efficiency for the William's Slocum glider hydrodynamic model [2]

hydrodynamic efficiencies. The difference is mainly due the assumptions surrounding the glider's angle of attack $\alpha$. By measuring $\alpha$ directly a more accurate hydrodynamic model may be created.

# Chapter 3

# Propulsion Module Design

A design for an auxiliary propulsion module for an underwater glider is presented. The propulsion module is designed using an integrated approach where hydrodynamic, mechanical and electrical performances are considered as a whole to maximise the propulsive efficiency of the vehicle.

## 3.1 Design Constraints

To minimise the impact of the propulsion unit on the performance of the glider, certain constraints were placed on the design. The module should be able to be turned on and off to allow the glider to retain its normal buoyancy-driven method of operation. In light of this, during regular operations, the influence of the propulsion unit on the hydrodynamic performance of the glider should be minimised. The impact of the propulsion module on the glider's endurance and range when propelled for horizontal flight at typical glide speeds should be such that the propulsor should consume equal or less power than the buoyancy engine. Also, the module should be capable of providing enough thrust to enable a sprint mode to at least double the glider's typical

speed for short durations. These constraints provide a unique challenge in developing a high efficiency, low power propulsion module.

## 3.2 Design

To design a prototype device within these constraints an overall concept was chosen utilising an electric motor, magnetic coupling and folding propeller. These components require careful design matching to ensure that the peak operational regions overlap one another. To this end, electric motors provide the necessary energy density for a small low power device and provide good efficiency matching potential to peak propeller efficiencies. A magnetic coupling was selected to minimise frictional losses due to shaft seals.

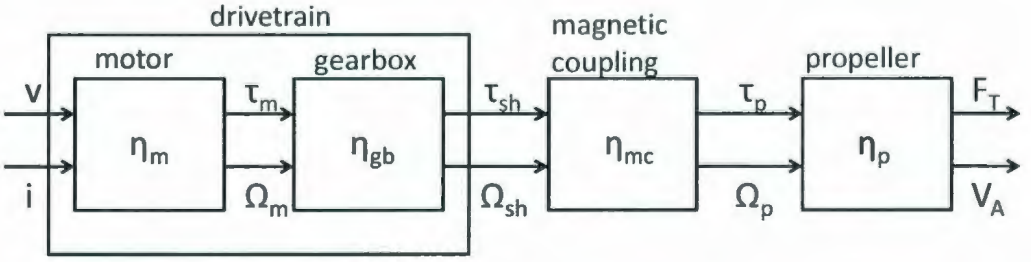


Figure 3.1: Energy flow diagram showing the inputs and outputs for each stage of energy conversion

Initial matching of the motor, gearbox and propeller was done using the simplified drag force model from section 2 and nominal glider operational parameters as a reference for design. The energy flow for the system is shown in Fig. 3.1, where the product of the inputs over the product of the outputs is equal to the efficiency of the particular subsystem. The system efficiency $\eta_{sys}$ is then given as the product of the subsystem efficiencies

$$\eta_{sys} = \eta_m \eta_{gb} \eta_{mc} \eta_p \tag{3.1}$$

where $\eta_m$ is the motor efficiency, $\eta_{gb}$ is the gear box efficiency, $\eta_{mc}$ is the magnetic coupling efficiency and $\eta_p$ is the propeller efficiency. The efficiency of the motor controller may be included in $\eta_{sys}$ as well. However, for this design a high quality brushed motor with precious metal brushes was chosen with the final design to be driven directly from the rail voltages of 14.4 V and 3.3 V to give a high and low speed operation point. The motor controller efficiency was therefore left out of the system efficiency definition. Also left out of the system efficiency definition is the battery performance which is a product of environmental conditions and the electrical load requirements. The effects of the environmental conditions are left out because they apply to buoyancy driven vehicles and propeller driven vehicles. The electrical load for the auxiliary propulsion module is a continuous load and intermittent for the buoyancy engine. This difference can impact the battery performance differently due to $I^2R$ losses. The instantaneous $I^2R$ losses for the auxiliary propulsion module are on the order of 0.001 W and for the buoyancy engine they are on the order of 0.01 W, where R, in this case, is the internal resistance of the batteries equal to 0.15Ω [70]. However, since the buoyancy engine use is intermittent, the $I^2R$ losses are reduced to a negligible level. Both $I^2R$ loss cases are therefore considered to be irrelevant when compared to the time averaged power consumption.

In general the motor efficiency may be given as [71]

$$\eta_m = \frac{\tau_m \Omega_m}{iu} \frac{2\pi}{60} \tag{3.2}$$

where the motor torque $\tau_m$ and the motor speed $\Omega_m$ are given by

$$\tau_m = k_1 (i - i_o) \tag{3.3}$$

$$\Omega_m = uk_2 - k_3\tau_m \tag{3.4}$$

with (3.3)

$$\Omega_m = uk_2 - k_3k_1(i - i_o) \tag{3.5}$$

Substituting (3.3) and (3.5) into (3.2) gives

$$\eta_m = \frac{k_1(i - i_o)[uk_2 - k_3k_1(i - i_o)]}{iu}\frac{2\pi}{60} \tag{3.6}$$

showing that the resulting motor efficiency depends on only the input voltage $u$ and current $i$ where $k_1$ is the torque constant, $k_2$ is the speed constant, $k_3$ is the motor constant and $i_o$ is the motor no-load current.

A propeller was modelled as a small blade area ratio propeller using the OpenPVL MATLAB scripting [72]. The gearbox was assigned a fixed efficiency due to mechanical losses as given by the data-sheet from the manufacturer. The magnetic coupling efficiency was assumed to be constant irrespective of motor or propeller selection and was therefore removed from the parameter space for the purposes of propeller, motor and gearbox matching. The propeller torque constant $K_\tau$ [73] may be written as

$$K_\tau = \frac{\tau_p}{\rho(\frac{\Omega_p}{60})^2 d_p^5} \tag{3.7}$$

which may be re-written to give the propeller torque $\tau_p$

$$\tau_p = K_\tau \rho(\frac{\Omega_p}{60})^2 d_p^5 \tag{3.8}$$

where $\tau_p$ is the propeller torque, $d_p$ is the propeller diameter and $K_\tau$ is the propeller torque constant. The propeller torque constant $K_\tau$ shaft speed $\Omega_p$ are outputs from the OpenPVL MATLAB scripting.

The peak efficiencies for electric motors generally occur for RPMs that are higher than the peak efficiency for propellers. Gearboxes are therefore used to match the RPM of a given motor to the peak operational region of the propeller. If the gearbox ratio is too small the motor efficiency will be small due to the propeller speed requirements being well below the motor's peak operational region. However, for each stage of gear reduction additional mechanical losses are accrued by the gearbox thus reducing its efficiency. These parameters compete against one another and by iterating the gearbox and motor parameters a motor and gearbox combination showing peak performance for the theoretical small blade-area-ratio propeller and nominal glider operational conditions may be chosen.

The propeller efficiency generated by the OpenPVL MATLAB script was plotted against the output of the motor model for different motor and gearbox combinations to match the peak efficiencies for a given shaft speed $\Omega_p$ and propeller torque $\tau_p$ as in Fig. 3.2 - 3.5. The script for these figures is included in Appendix A. The voltage input to the motors was limited to the vehicle battery voltage of 15V to maintain the operational region of the motors. The propeller design shaft speed was 100 RPM for an advance velocity of 0.35 m/s and 0.4 N of thrust resulting in a $K_\tau = 0.0051$.

The motor's considered in Fig. 3.2 - 3.5 have motor coefficients as defined in Tab. 3.1 with gearbox's having coefficients as defined in Tab. 3.2. This data is supplied from manufacturers data sheets [71].

From Tab. 3.1 and 3.2 the m1 motor and gb1 gearbox were selected. The predicted motor performance for this motor and gearbox combination is shown in Fig. 3.2. In this figure it is shown that the m5 motor results in a high motor efficiency for the design propeller speed of 100 RPM. However, this motor when combined with the gb1 gearbox was too long to fit inside of the motor housing and the m1 motor was selected instead.

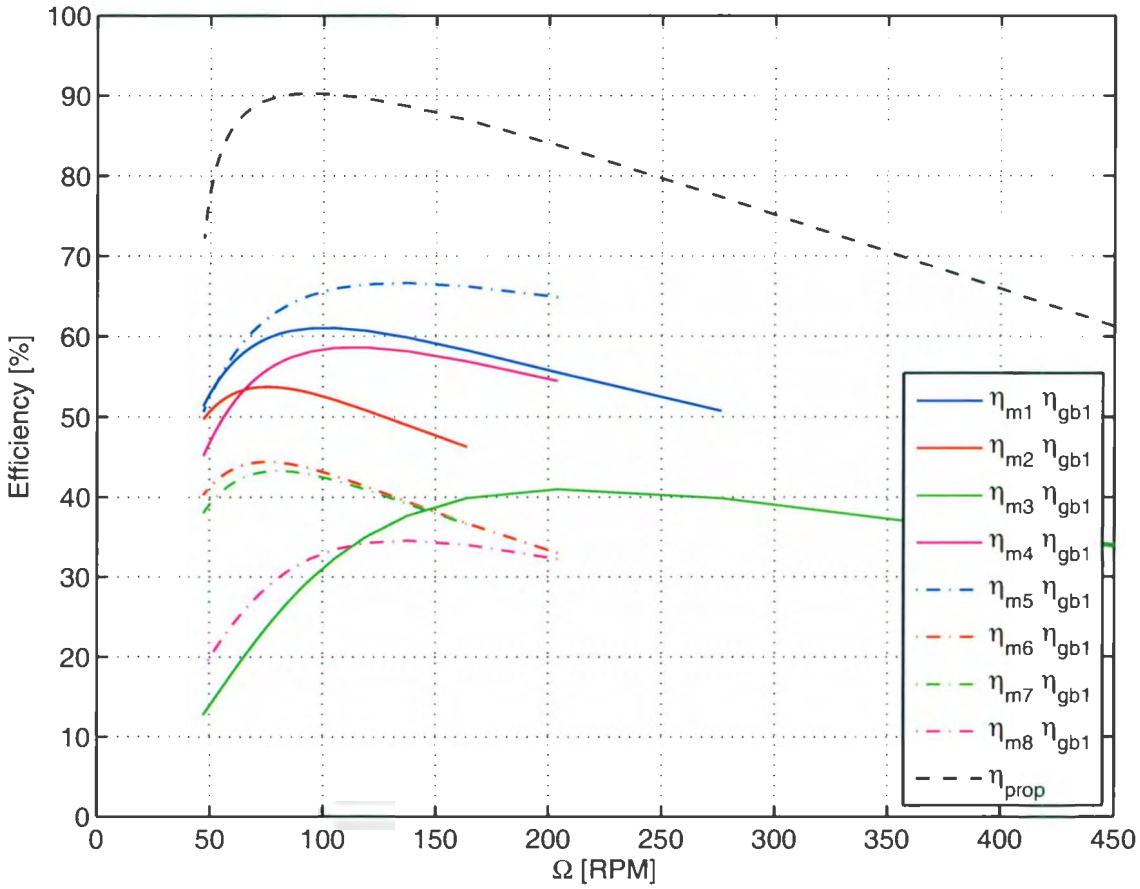


Figure 3.2: Motor and propeller efficiencies plot showing motors 1-8 combined with gearbox 1.

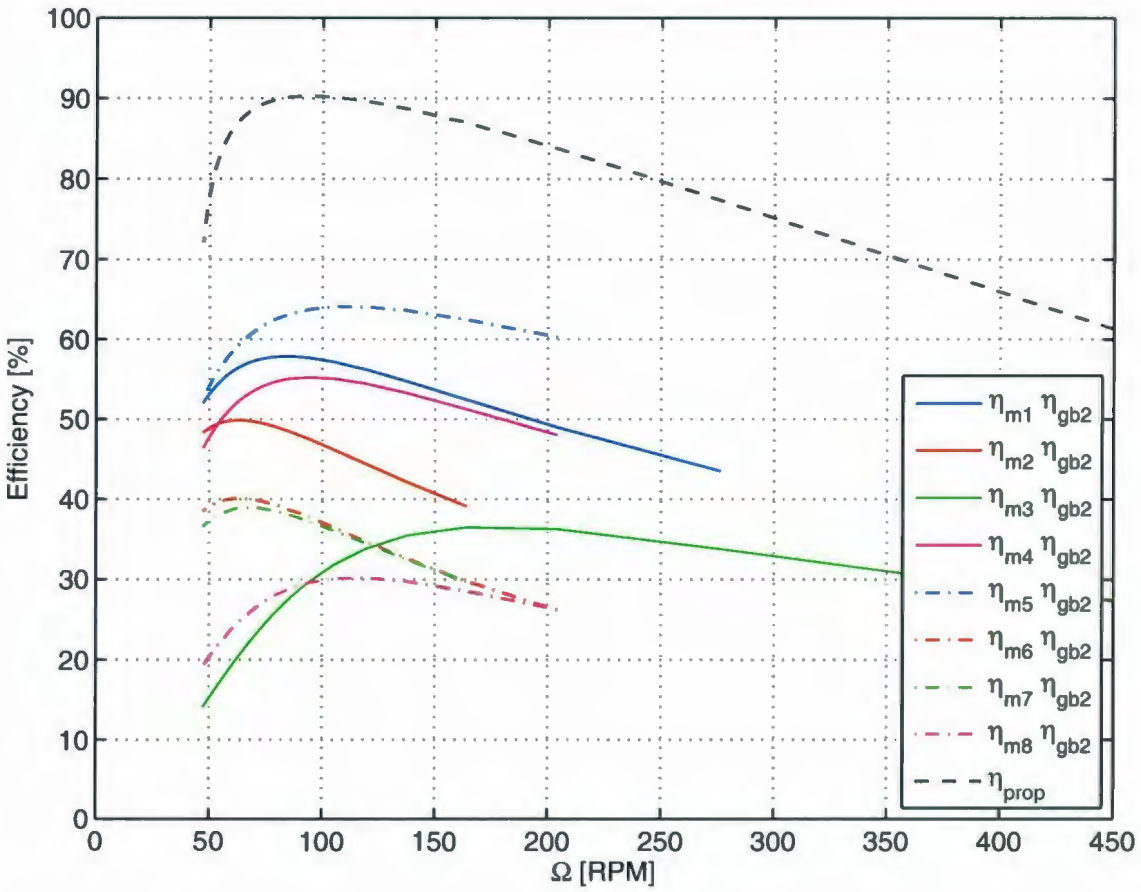


Figure 3.3: Motor and propeller efficiencies plot showing motors 1-8 combined with gearbox 2.

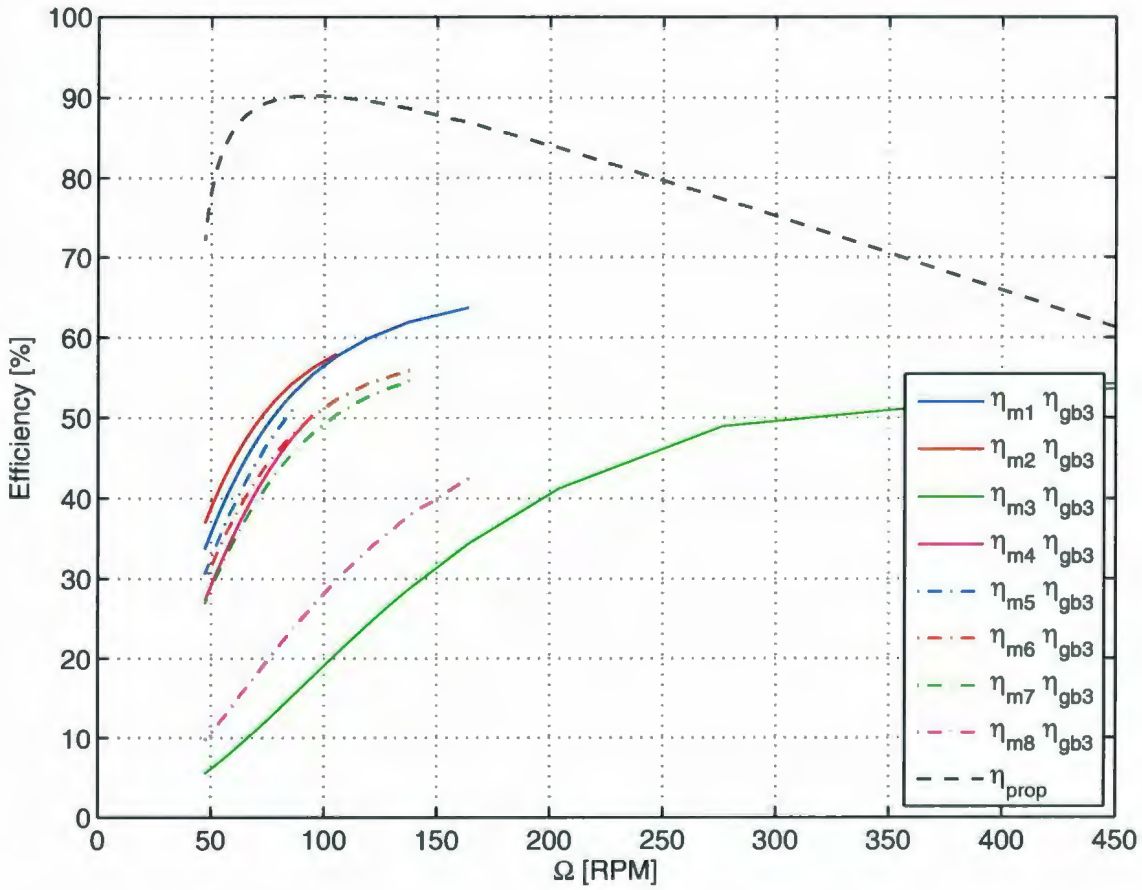


Figure 3.4: Motor and propeller efficiencies plot showing motors 1-8 combined with gearbox 3.

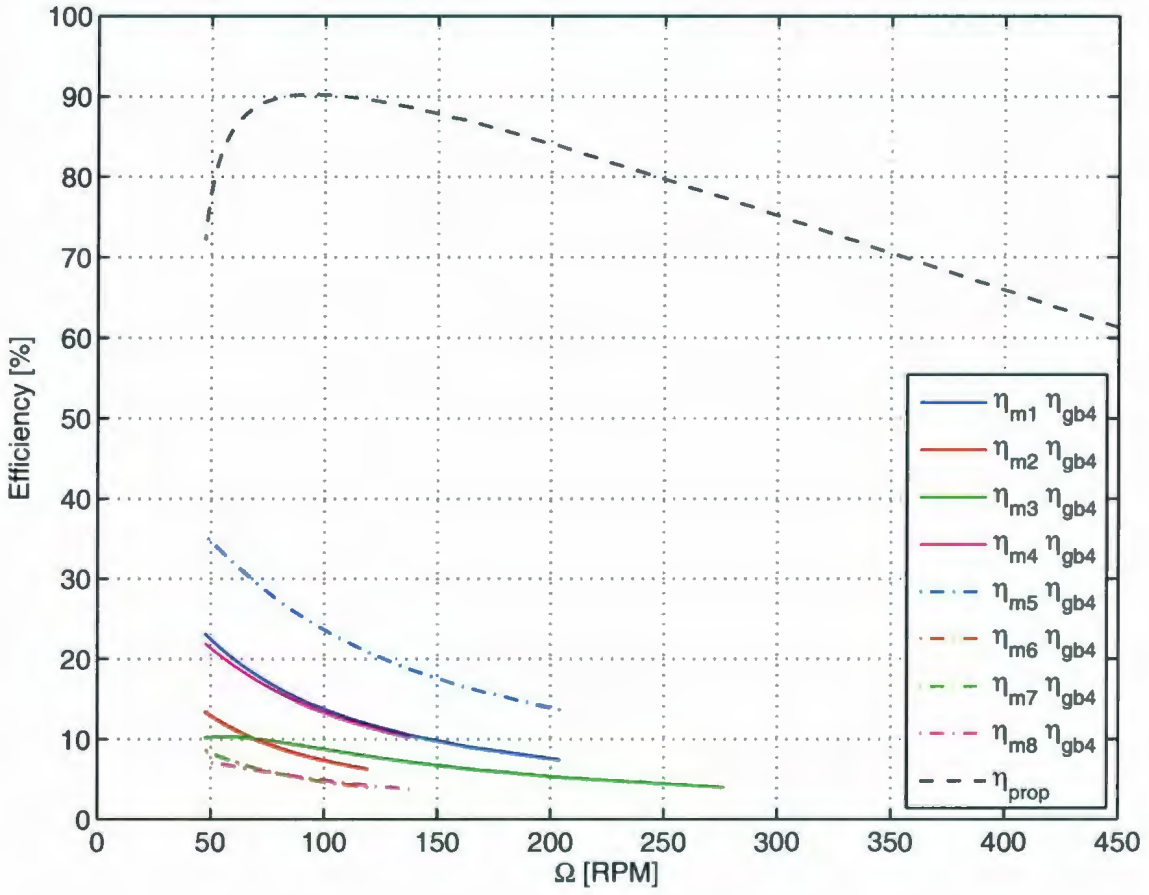


Figure 3.5: Motor and propeller efficiencies plot showing motors 1-8 combined with gearbox 4.

| | $k_1$ | $k_2$ | $k_3$ | $i_o$ |
|---|---|---|---|---|
| Units | [Nm/A] | [RPM/V] | [Nm/RPM] | [A] |
| **m1** | **9.92 E-3** | **9.62 E2** | **8.04 E5** | **7.35 E-3** |
| m2 | 1.39 E-2 | 6.85 E2 | 1.64 E6 | 4.27 E-3 |
| m3 | 3.33 E-3 | 2.9 E3 | 1.11 E6 | 2.34 E-1 |
| m4 | 1.63 E-2 | 5.84 E2 | 8.25 E5 | 6.45 E-3 |
| m5 | 1.9 E-2 | 5.02 E2 | 4.04 E5 | 4.63 E-3 |
| m6 | 9.17 E-3 | 1.04 E3 | 2.60 E6 | 9.54 E-3 |
| m7 | 1.07 E-2 | 8.93 E2 | 2.6 E6 | 9.69 E-3 |
| m8 | 8.23 E-3 | 1.16 E3 | 2.32 E6 | 4.88 E-2 |

Table 3.1: Motor coefficients for motors considered during selection. The selected motor is shown in bold.

| | **gb1** | gb2 | gb3 | gb4 |
|---|---|---|---|---|
| *Ratio* | **29** | 24 | 84 | 5.4 |
| $\eta_{gb}$ | **81** | 81 | 73 | 90 |

Table 3.2: Gearbox coefficients for gearboxes considered during selection. The selected gearbox is shown in bold.

Since the level of input energy is very low, on the order of 1W, all stages of energy conversion were considered and all losses were minimised. Shaft seal frictional losses, which in a more powerful system account for only a fraction of the total power, dominate in low power systems. To this end, a magnetic coupling was used and designed such that the pull-out torque was just beyond what the theoretical requirements were for the propeller to move the glider at a sprint speed of 0.75 m/s. Magnetic couplings often require additional bearings and the lubrication and seals on bearings consume a large portion of a single Watt system's power. Therefore, ultra-low friction, dry-lubricated, ceramic bearings were used to reduce these losses. The losses from the magnetic coupling and bearings were quantified through analysis of the motor input current before and after assembly. For the maximum voltage condition, this difference equates to a change in current of 3 mA resulting in less than 0.001 Nm frictional torque in the magnetic coupling assembly, which is 10 % of the no-load torque and 1 % of the full load torque. These losses are a result of frictional losses in the bearings as well as eddy current losses due to the rotating magnetic fields.

To summarise the motor selection process has been detailed showing the matching of motor and gearbox to a simulated propeller performance. A brief discussion of the sources of mechanical losses highlights the importance of careful component selection and tolerances.

## 3.3 Propeller Selection and Testing

In this section the propeller design process for the propulsion module is presented. This process takes the thrust requirements and advance velocity from the hydrodynamic model. As an initial estimate the ideal actuator disk efficiency $\eta_I$ may be

computed as in [73]

$$\eta_I = \frac{2}{1 + \sqrt{\frac{2F_T}{\rho A_p {v_A}^2} + 1}} \tag{3.9}$$

where $F_T$ is the thrust. This equation may be re-written to show the relationship between the hull diameter and propeller diameter at steady state and level flight by substituting (2.3) for $F_T$ as in

$$\eta_I = \frac{2}{1 + \sqrt{\frac{d_v^2 C_D}{d_p^2} + 1}} \tag{3.10}$$

where $d_v$ is the vehicle diameter and $d_p$ is the propeller diameter; for the Slocum 200m glider $d_v = 0.21$ m. The ideal efficiency for a given propeller diameter is plotted in Fig. 3.6

The ideal efficiency shows that for larger diameter propellers the propeller efficiency increases. Additionally, it gives the upper bound for expected efficiency for the propeller that is selected. In order to minimise the drag from the propeller while the propulsion module is not in use folding propellers were selected for use. However, no suitable folding propellers were found with published torque and thrust data for low advance velocities and low levels of thrust. Therefore, a propeller was designed using the OpenProp MATLAB code with a cord length to diameter ratio as shown in Fig. 3.7

Additional inputs include an advance velocity of $v_A = 0.35 m.s$, thrust of $F_T = 0.4N$ and $\Omega = 100 RPM$ for a two bladed propeller. The propeller efficiency for these parameters is shown in Fig. 3.2. The propeller was output into a 3-D CAD model and prototyped on a Fused Deposition Modelling (FDM) Machine. When tested however it was found that the blades suffered significant deformations resulting in efficiencies 60% less than predicted. Since the propeller design was not the focus

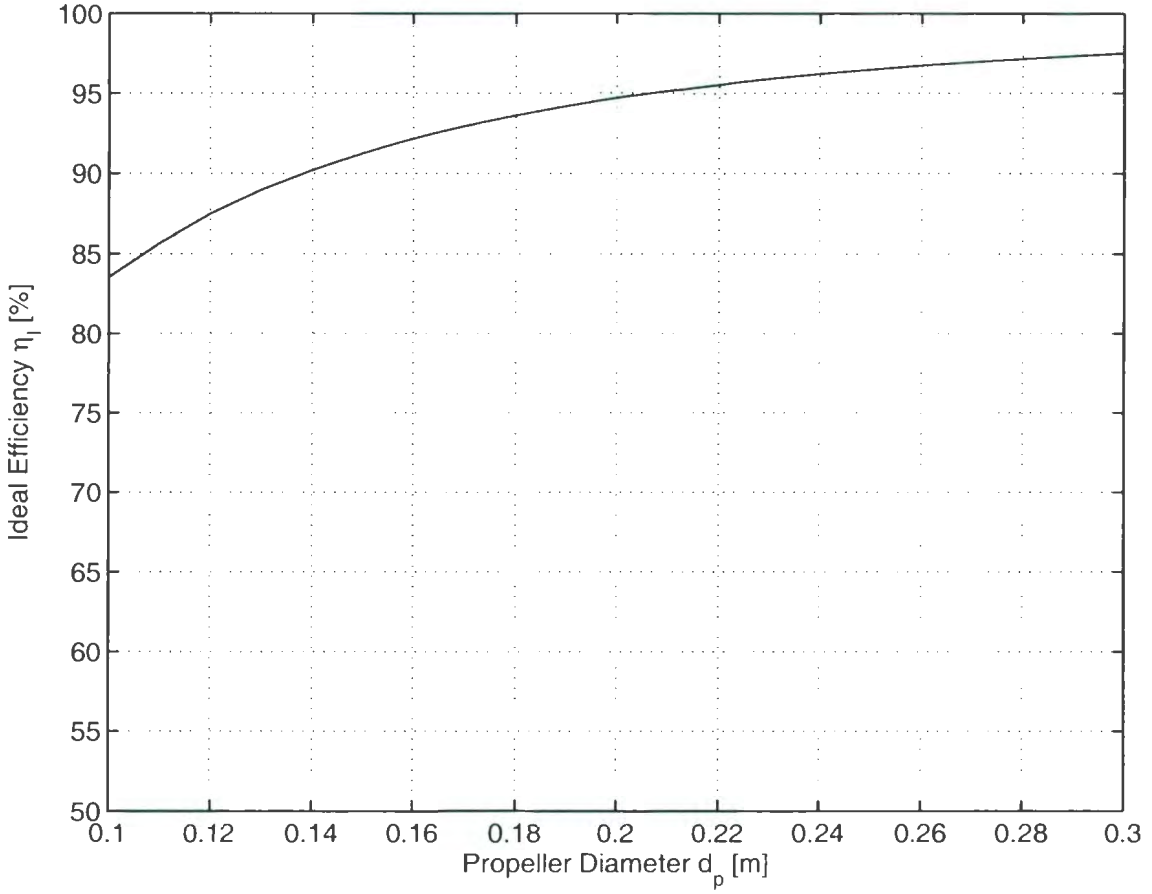


Figure 3.6: Ideal propeller efficiency for different propeller diameters with a propeller located at the rear of a Slocum 200m glider.

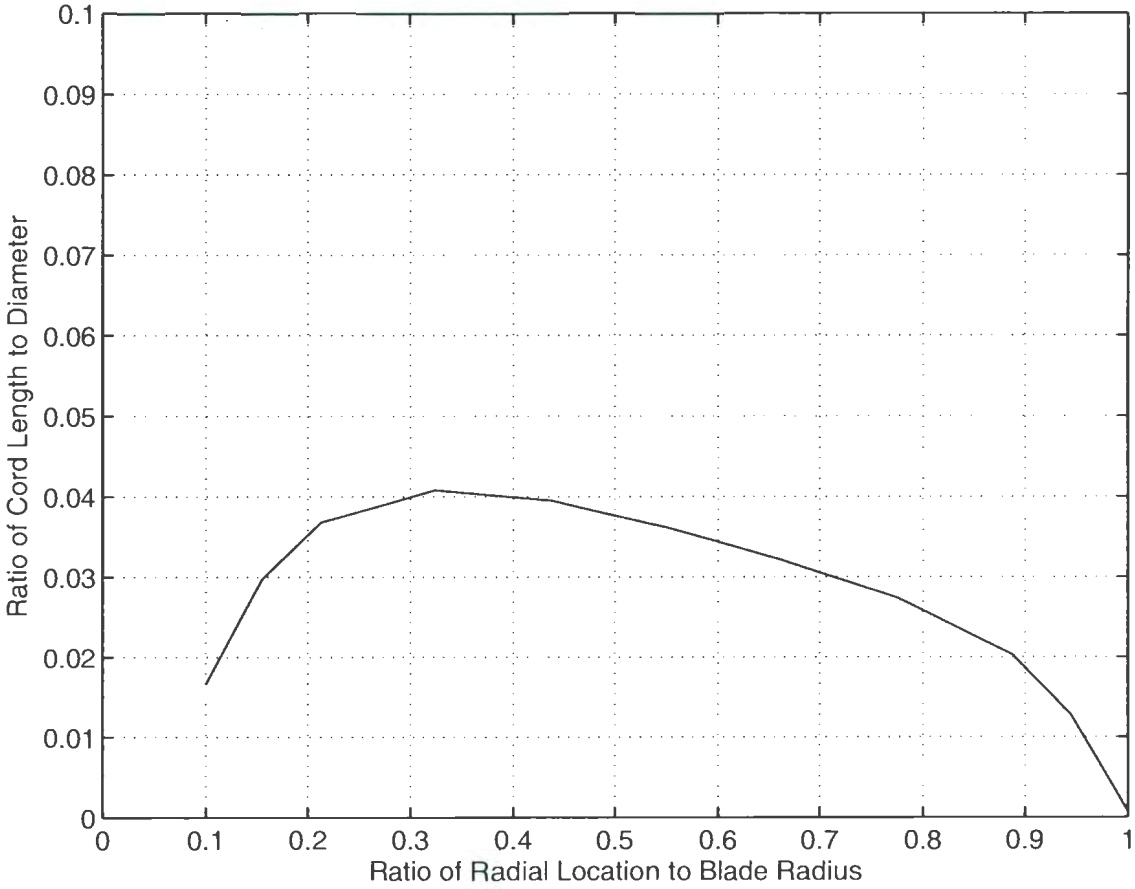


Figure 3.7: Input ratio of cord length to diameter for the propeller designed using the OpenProp MATLAB code

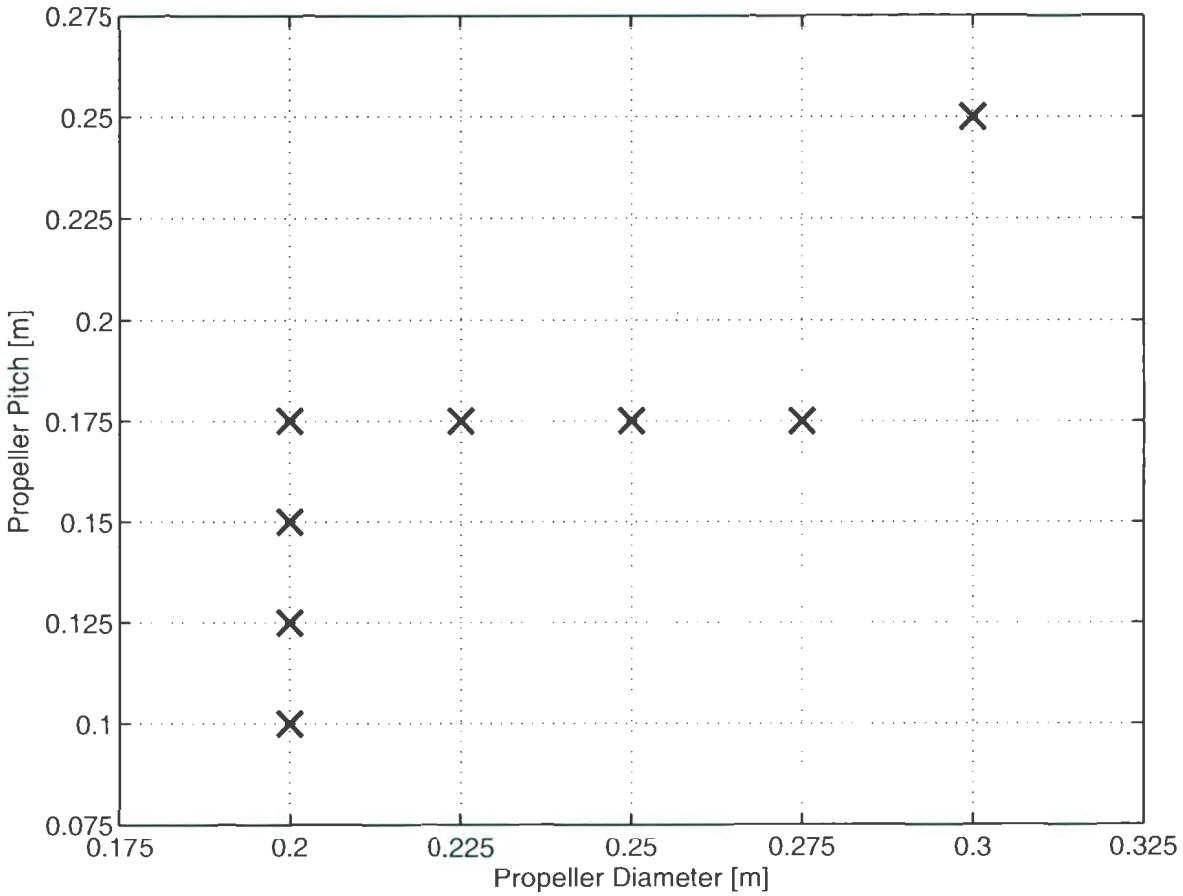


Figure 3.8: Selection of propellers tested in the Memorial University of Newfoundland flume tank.

of this work a series of RC folding model airplane propellers were selected to be tested experimentally to determine their operating parameters. These propellers use a graphite reinforced plastic which provides a good degree of stiffness for the loads under consideration. Propellers with varying diameters and pitch ratios were selected for tests as shown in Fig. 3.8.

To characterise these propellers $v_A$, $F_T$, $u$ and $i$ were measured in the 0.3 m x 0.5 m x 5 m flume tank at MUN using the experimental setup shown in Fig. 3.9. Electrical current and voltage were measured using a Hall Effect current sensor and a resistive

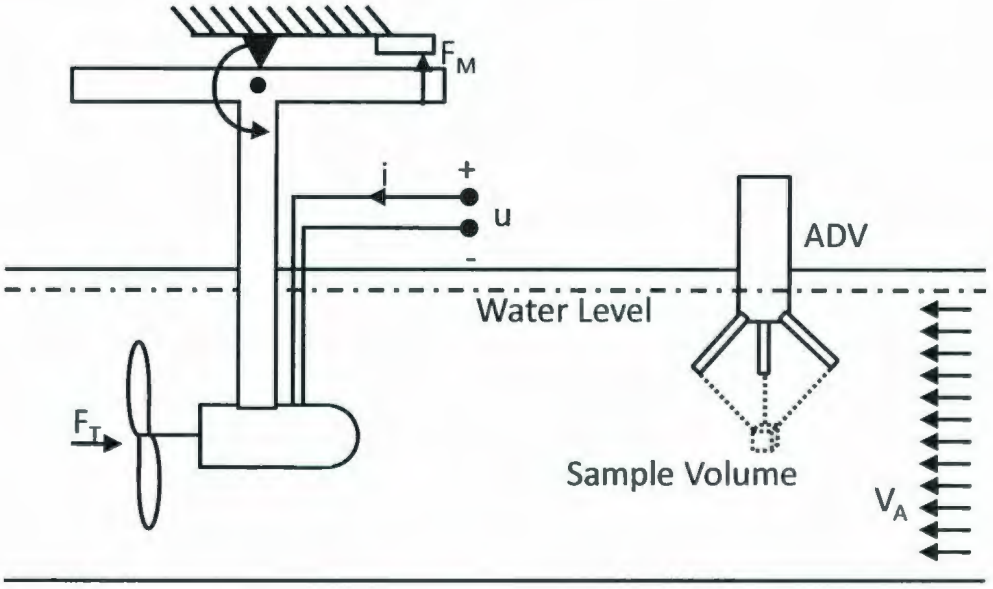


Figure 3.9: Memorial University of Newfoundland flume tank test schematic for propulsion system characterisation.

voltage divider. The thrust was measured using a lever to amplify the force and an Omega LCAE-6kg load cell with a Dataforth DSCA38-05 signal conditioner. The lever arm for thrust measurement $F_T$ was calibrated using known masses attached through pulleys to the centerline of the propulsion module as shown in Fig. 3.10 The resultant conversion formula is given by

$$F_T = 1.8715(F_M - F_o) \tag{3.11}$$

where 1.8715 is the lever ratio, $F_o$ is the drag force on the measurement apparatus and $F_M$ is the measured force. These values were read into MATLAB for further processing using the Data Acquisition Toolbox and a National Instruments USB-6211 data acquisition system. The advance velocity $v_A$ of the water was measured using a SonTek ADVOcean Acoustic Doppler Velocimeter (ADV). Tests were performed

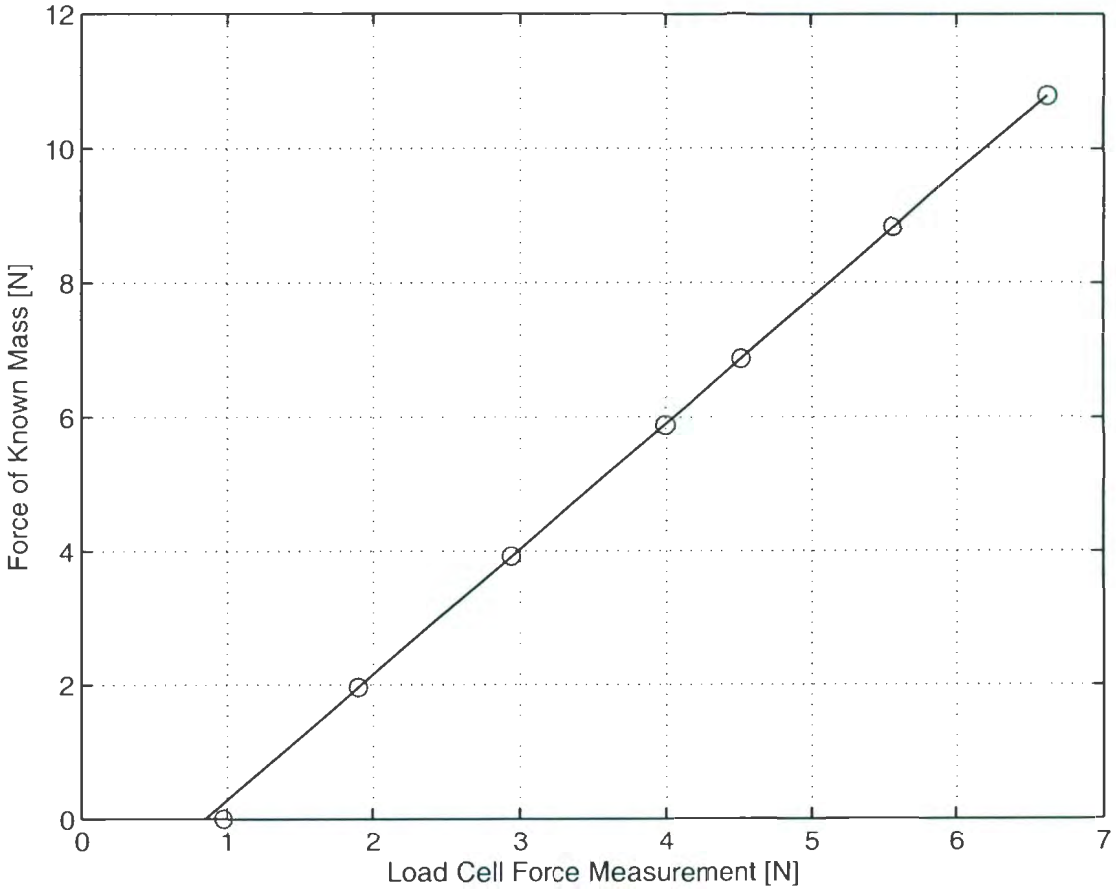


Figure 3.10: Calibration of the load cell in the Memorial University of Newfoundland flume tank experiment

for flow speeds of 0.3, 0.4 and 0.5 m/s where the input current to the motor was controlled from 0 A to the pull out torque at 0.3 A. The measured system efficiency $\hat{\eta}_{sys}$ is calculated as in

$$\hat{\eta}_{sys} = \frac{F_T v_A}{iu} \tag{3.12}$$

Using the motor model presented in (3.6), the propeller efficiency may be deduced from the system efficiency as in

$$\eta_p = \frac{F_T v_A}{\tau_m \Omega_m} \frac{60}{2\pi} \tag{3.13}$$

where $\tau_m$ is (3.3) and $\Omega_m$ is (3.4). The motor efficiency is also computed according to (3.6). It should be noted that the mechanical losses in the magnetic coupling and bearings are lumped in with the propeller efficiency. The results from these tests showing the system efficiency $\hat{\eta}_{sys}$, the thrust $F_T$ and the vehicle drag force $F_D$ at $v_A$ = 0.3, 0.4 and 0.5 m/s are shown in Fig's. 3.11 - 3.13.

A non-folding 0.2 m diameter propeller with a pitch of 0.15 m was also selected for testing to compare the performance of folding and fixed bladed propellers. The fixed propeller results are shown with the folding propeller results in Fig. 3.14. These results are shown only for advance velocities of 0.3 and 0.5 m/s as there was a loose connection on the electrical current sensing device for the tests with an advance velocity of 0.4 m/s and the data was unusable.

The fixed propeller efficiencies are higher than the efficiencies for the same size of folding propeller. This difference is attributed to the size of the hub for the folding propeller as well as the differences in the blade area ratio. The folding propeller has a larger hub size relative to the fixed propeller to accommodate the folding mechanism. The fixed propeller also has a larger blade area ratio when compared with the folding

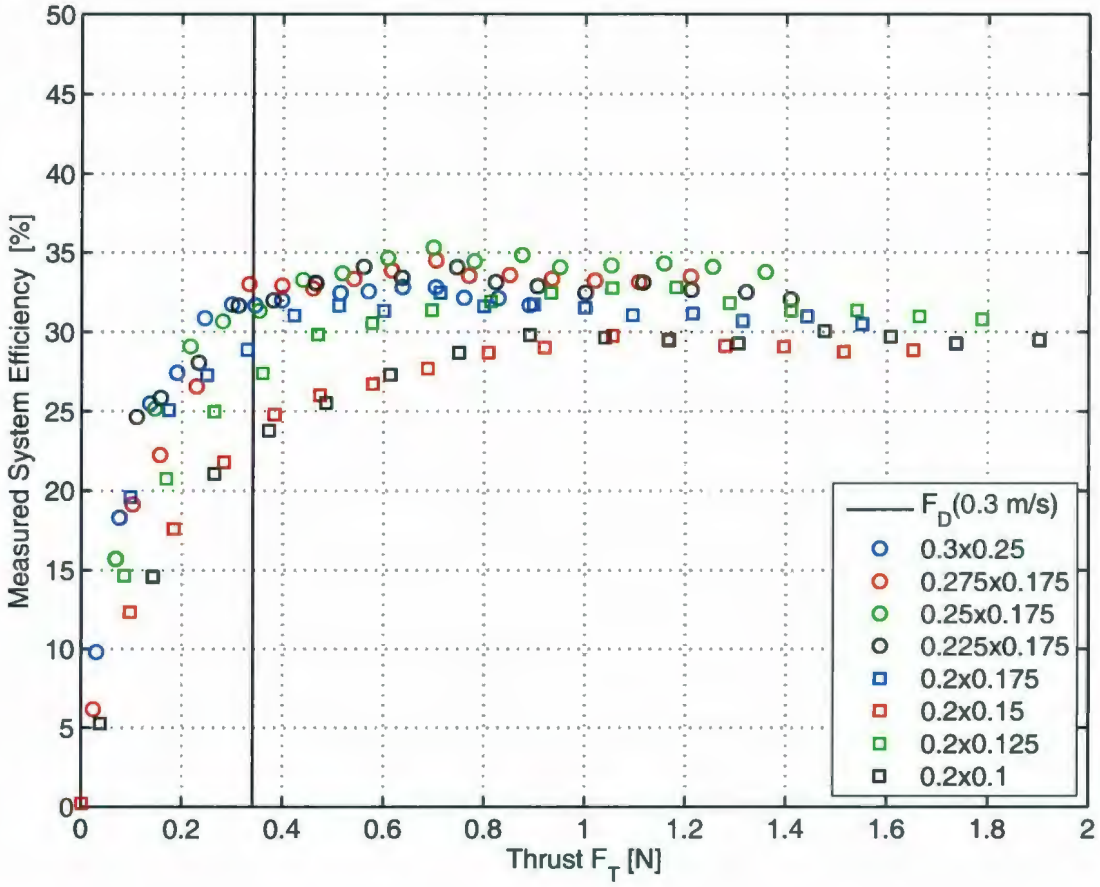


Figure 3.11: Efficiencies of propellers for a given thrust for a flume tank water velocity of 0.3 m/s, the drag force for a glider with an advance velocity of 0.3 m/s is shown as a vertical line

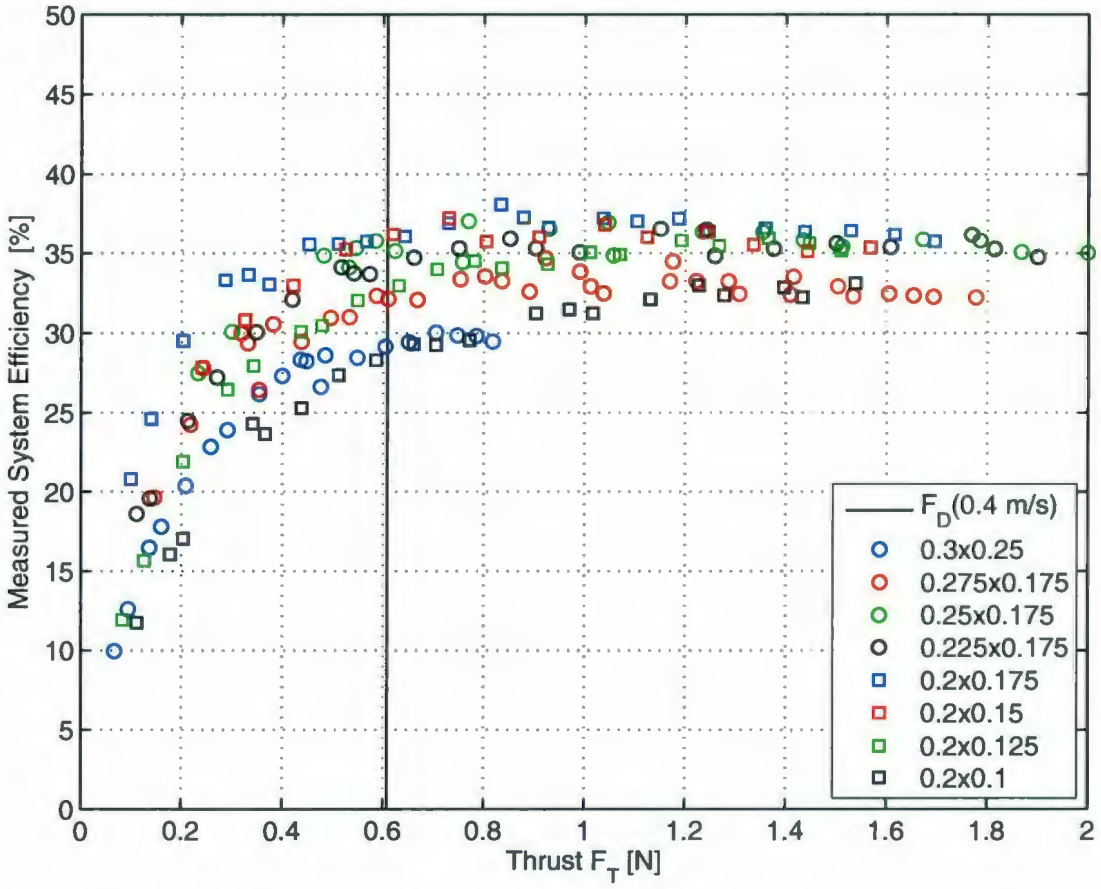


Figure 3.12: Efficiencies of propellers for a given thrust for a flume tank water velocity of 0.4 m/s, the drag force for a glider with an advance velocity of 0.4 m/s is shown as a vertical line

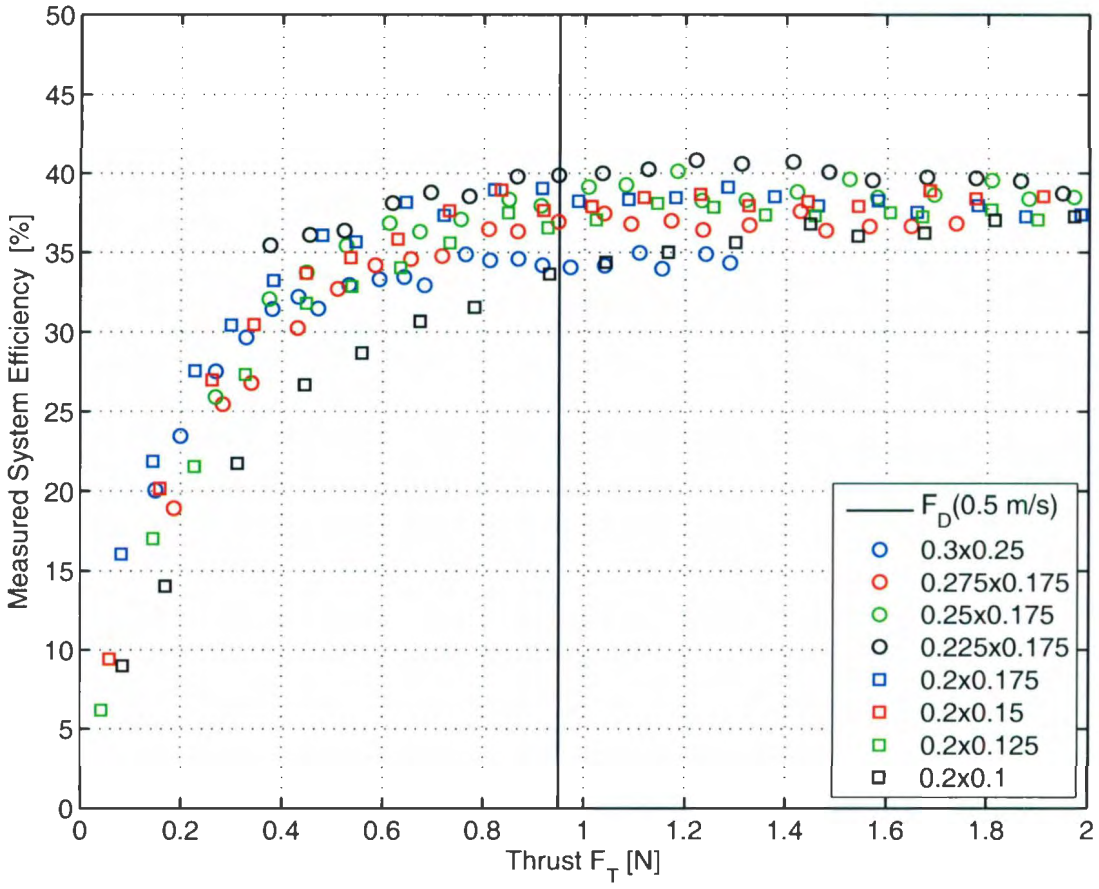


Figure 3.13: Efficiencies of propellers for a given thrust for a flume tank water velocity of 0.5 m/s. the drag force for a glider with an advance velocity of 0.5 m/s is shown as a vertical line

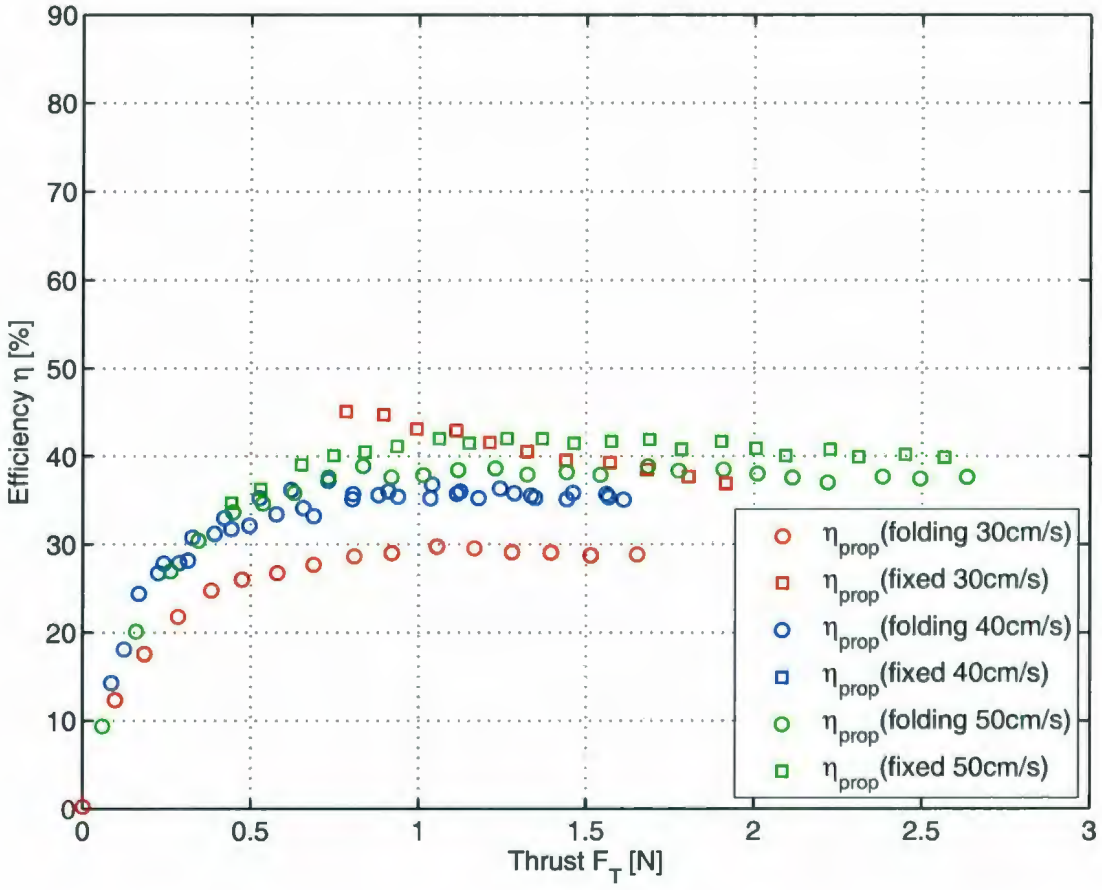


Figure 3.14: Fixed propeller and folding propeller comparison for a propeller with a diameter of 0.2 m and a pitch of 0.15 m at flow speeds of 0.3 m/s and 0.5 m/s.

Figure 3.15: Image showing the differences between the fixed and folding propellers with a diameter of 0.2 m and a pitch of 0.15 m.

propeller. The difference between the fixed and folding propellers is shown in Fig. 3.15

By analysing the peak efficiencies from the data in Fig. 3.11 - 3.13 an optimum propeller of 0.225 m diameter and 0.175 m pitch may be selected for use on the hybrid glider. However, the selection above does not take into account the interaction between the propeller and the hull of the glider. The wake fraction $w$ and thrust deduction $t$ factors affect the performance of the propeller through the hull efficiency $\eta_h$ to give the total propulsive efficiency $\eta_d$ [74] as shown by

$$\eta_d = \eta_{sys}\eta_h = \eta_{sys}\frac{1-t}{1-w} \tag{3.14}$$

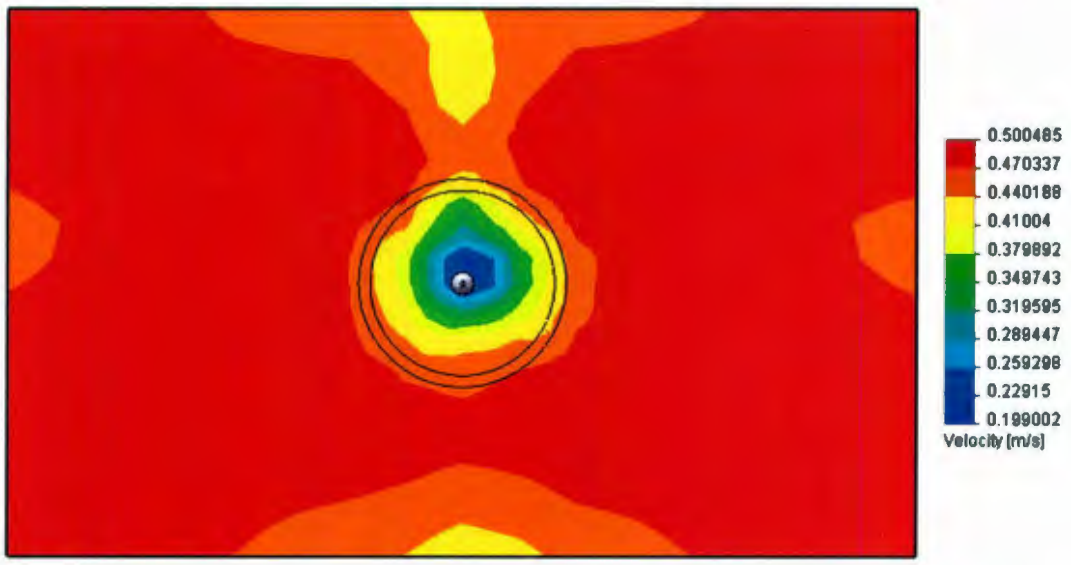


Figure 3.16: Velocity contours for a Slocum glider CFD model shown at the location of the propeller with a 0.2 m and 0.225 m circle overlaid to show the propeller disk area where the advance velocity is 0.5 m/s.

Estimates of the wake fraction from a computational fluid dynamic (CFD) model shown in Fig. 3.16 give values of $w$=0.34 and $w$=0.296 for 0.2 m and 0.225 m diameter propellers for $v_A = 0.5$ m/s. These values combined with an assumed thrust deduction factor of $t = 0.2$ from [74], results in $\eta_h = 1.212$ for the smaller propeller and $\eta_h = 1.136$ for the larger propeller as shown in Fig. 3.17; however, the relative difference in the open water system efficiency from the MUN flume tank tests for these two propellers is only 2 %. Additionally, the torque requirements of the 0.175 m pitch propeller were such that the magnetic coupling stalled at full power. For these reasons, a propeller with 0.2 m diameter and 0.15 m pitch was selected for the propulsion module. The motor and propeller efficiency for this propeller may be extracted from the data presented earlier using (3.13) and (3.6).

In Fig. 3.18 the motor, propeller and system efficiencies for the propulsion module

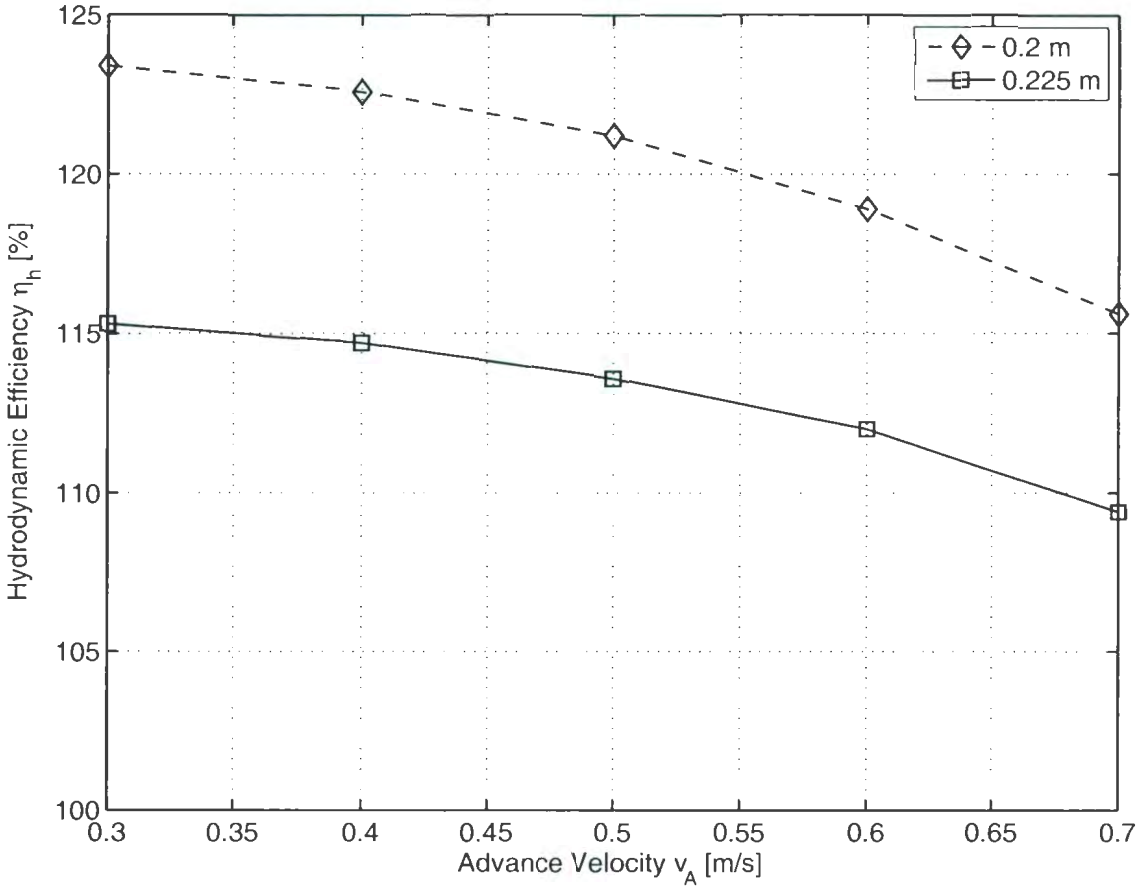


Figure 3.17: Hull efficiency from a computational fluid dynamic model for 0.2 m and 0.225 m diameter propellers.

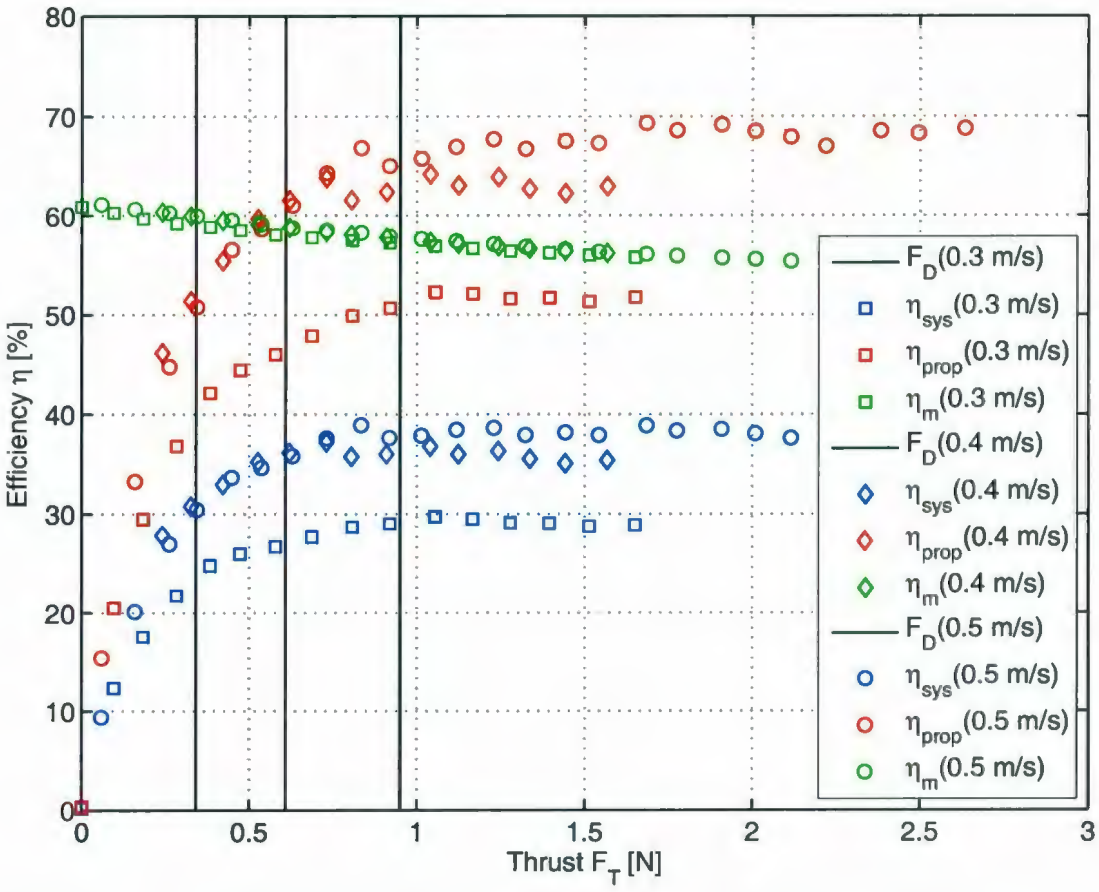


Figure 3.18: Propulsion module efficiencies for a propeller with 0.2 m diameter and 0.15 m pitch at advance velocities of 0.3, 0.4 and 0.5 m/s. The vehicle drag force is overlaid as vertical lines increasing from left to right for a given advance velocity.

in the MUN flume tank are shown. By examining the intersections of the drag force lines with the propeller data for the same velocity the predicted operating point is determined. Using this procedure the propeller efficiency is seen to increase with $v_A$ and the motor efficiency decreases with load resulting in a system efficiency which increases slightly with an increase in advance velocity.

The propeller selection and design is presented using an integrated approach resulting in a system that is well matched to the glider hull form and to the propulsive requirements for the design objectives. A range of small blade area ratio folding propellers were characterised and an appropriate propeller selected using the wake fraction from a CFD model.

# Chapter 4

# System Integration and Modification

The integration of the propulsion module into the glider is presented. From the design requirements this integration was done such that minimal changes would be necessary beyond what is easily accomplished by an experienced glider user.

## 4.1 Mechanical

Mechanically, the propulsion module was designed such that it replaces the 0.5 kg emergency drop weight at the rear of the glider. To this effect, the weight in water of the propulsion module is matched to the weight in water of the drop weight. This location has the added benefit of being directly in line with the centre of buoyancy of the vehicle; however, it currently removes the function of the emergency drop weight. Also, it interferes with the power plug used to turn the glider on and off requiring modification of the plug to make it shorter. Additionally, the cabling for the thruster requires a hole to be made in the drop weight housing. The assembly procedure

of the tail section requires the tail cone to be loosely placed over the tail. The propulsion module is inserted into the drop weight location and the cable connected to bulkhead connector. The tail cone is then secured into location. Future versions of the propulsion module will ease some of the installation and modification requirements as well as either adding an additional drop weight mechanism or incorporating an ejection mechanism into the propulsion module.

## 4.2 Electrical

Electrically, the glider has two Persistors; low power, single board computers, connected by a communications bus. The glider computer handles all control and low level functions while the science computer is used for integration of new payloads and sensors. To avoid changing the existing glider architecture the propulsion module is connected to the power pins on the science computer board used for powering payload instruments.

For testing purposes, the motor of the propulsion module is controlled through an L298N motor controller with the drive voltage being supplied from the science board payload power pins and logic level power from the Persistor stack's 3.3 V supply. A pulse width modulated (PWM) signal is input into the motor controller to control the input voltage to the motor and the logic inputs are fixed high or low to make the motor uni-directional. In future versions the motor will be run off the rail supply voltages in the glider to remove the electrical losses associated with the motor controller.

To measure power into the propulsion module a power monitoring board was developed to measure the input current and voltage using the same hall effect sensor and resistive voltage divider as in Section 3.3. The schematic for this device is included in Appendix B. The voltages were read in using the MAX127 analog to digital converter

(ADC) which is also used elsewhere in the glider allowing for easy integration into the code. This chip uses the serial peripheral interface (SPI) to communicate with the science computer Persistor board and is powered from the 3.3V power bus on the Persistor stack.

A Microstrain 3DM-GX3 inertial measurement unit (IMU) was also integrated into the system to measure the euler angles, angular rates and linear accelerations of the vehicle during the unconstrained open water tests. This device uses a RS-232 bus to interface with the science computer and is powered through a step down linear voltage regulator from payload power pins on the Science board.

## 4.3 Software

In software, interfacing to the science computer requires the use of proglets, which use a manufacturer specified finite state machine template to control science payloads. The hybrid proglet takes one input from the glider computer, the commanded duty cycle for the motor controller. The motor controller is powered on when the proglet is enabled from the glider computer.

The power monitoring proglet utilises the SPI interface to receive the voltage and current data from the ADC. This data is logged on the science computer flash along with the glider time-stamp. By default this data is also sent to the glider at a slower rate but may be disabled. Since the power for the power monitor is supplied from the Persistor stack, the power monitor is powered on with the science computer.

The Microstrain IMU proglet uses one of the RS-232 lines on the science board. Commands are sent to the device and data read back to the Persistor and stored on the science computer flash along with the glider time-stamp. The device is initialised when the science computer turns on and is then put into a low power state until the

proglet is enabled by the glider computer. The complete code listing for the above proglets may be obtained by contacting the author.

# Chapter 5

# System Evaluation and Testing

The testing of the vehicle with the propulsion module is presented. The evaluation of its performance was done incrementally using different test facilities here in St. John's. Validation of the drag model at zero angle of attack is presented. To evaluate the vehicle's stability the tuning of the depth controller is detailed as well.

## 5.1 Tow Tank Self Propulsion Experiments

Self propulsion tests were performed in the tow tank at MUN to evaluate the glider's propulsive capabilities. The experimental setup for these tests involved a tensioned guide wire being strung the length of the tank 1 m below the water surface. The glider was attached to the guide wire such that it was able to move under self propulsion while being constrained directionally. The directional constraints are necessary due to the inability of the magnetic heading reference to function in the tow tank.

For these tests the electrical input voltage and current was measured. The advance velocity of the glider was measured by timing the glider as it moved through a known distance. Several different configurations were tried for fixing the glider to the guide

wire to minimise the friction due to the attachment points. Initial tests used tie-wraps through tie-wrap mount points, however, after bringing the glider out of the water and investigating the state of the tie-wraps significant wear was present. Teflon coated wire taped to the underside of the hull was also used which worked well for several runs until the wire slipped from the tape. The final setup had the tensioned guide cable passing through plastic tubing and tie-wrapped to the tie-wrap mounting points.

This setup allows for testing of many different propulsion configurations to analyse the relative impact of a change in propeller or hull configuration. The standard configuration for comparison to others is the glider with wings attached, the sensor hole on the tail-cone taped over and the power plug placed inside the tail-cone as shown in Fig. 5.1

In this configuration two propellers were tested, a propeller with 0.2 m diameter and 0.15 m pitch and another propeller with 0.225 m diameter and 0.175 m pitch. The smaller propeller, i.e., the propeller selected during the design phase, was run at seven different voltages and the larger propeller at only three different voltages. These results are shown in Fig. 5.2 with the motor duty cycle shown in Fig. 5.3.

In Fig. 5.2 and 5.3 the larger propeller was unable to be run at higher power levels due to torque limits in the magnetic coupling. From these results the larger propeller is capable of higher overall speeds at higher power levels. However, to achieve higher advance velocities the magnetic coupling requires adjusting to increase the pull-out torque.

The influence of sensor holes in the tail-cone, the power plug external to the tail-cone and the removal of the wings were also examined. Each variable was tested individually, only making one change from the standard configuration. To test the sensor hole influence the tape covering the hole was removed. For the power plug test

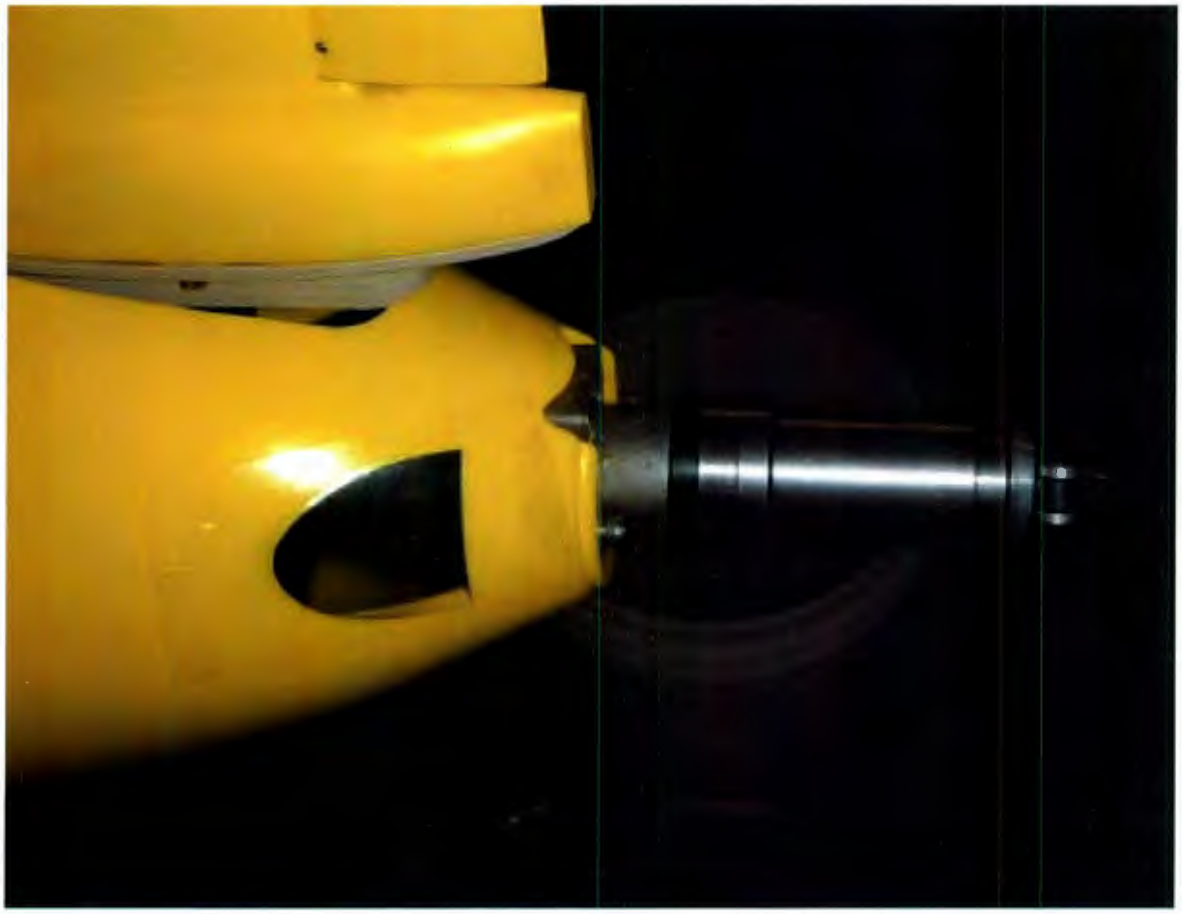

Figure 5.1: Glider 49 showing the standard testing configuration of a taped sensor hole and power plug inside of tail-cone

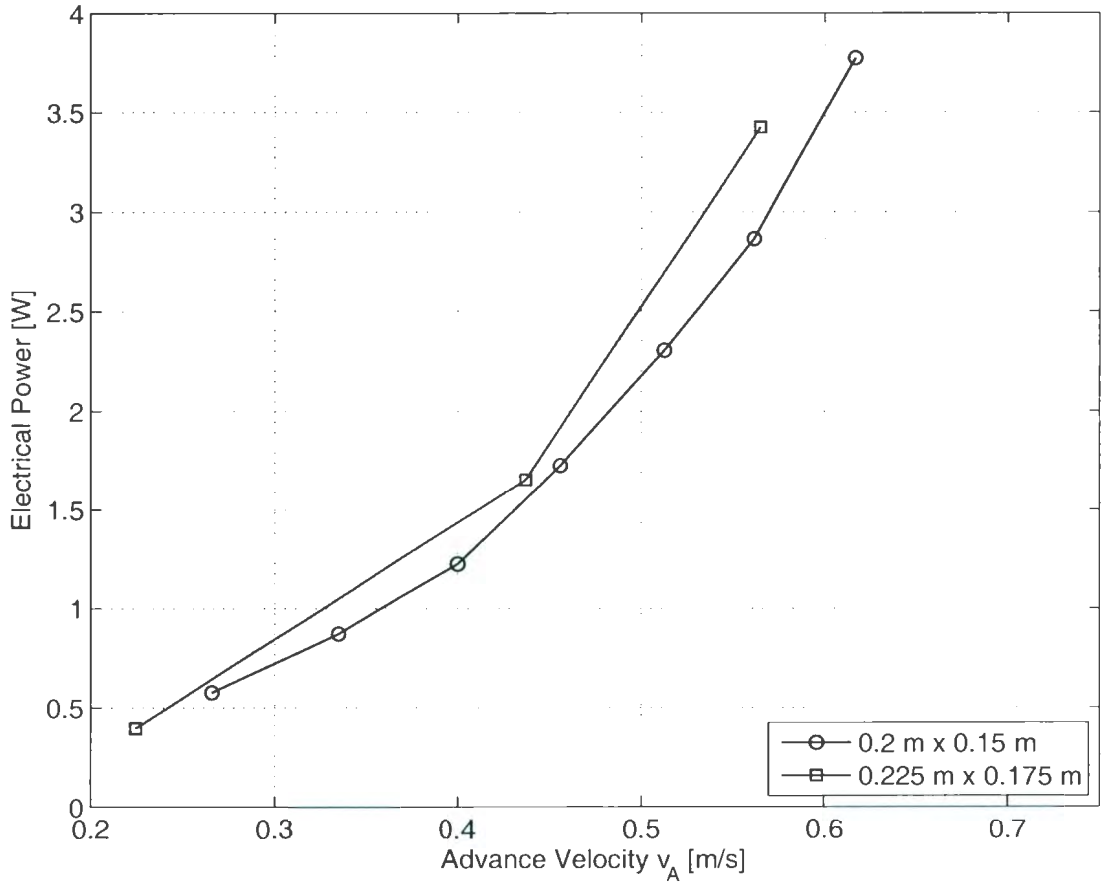


Figure 5.2: Power requirements for a given velocity for different propellers in the Memorial University of Newfoundland tow tank

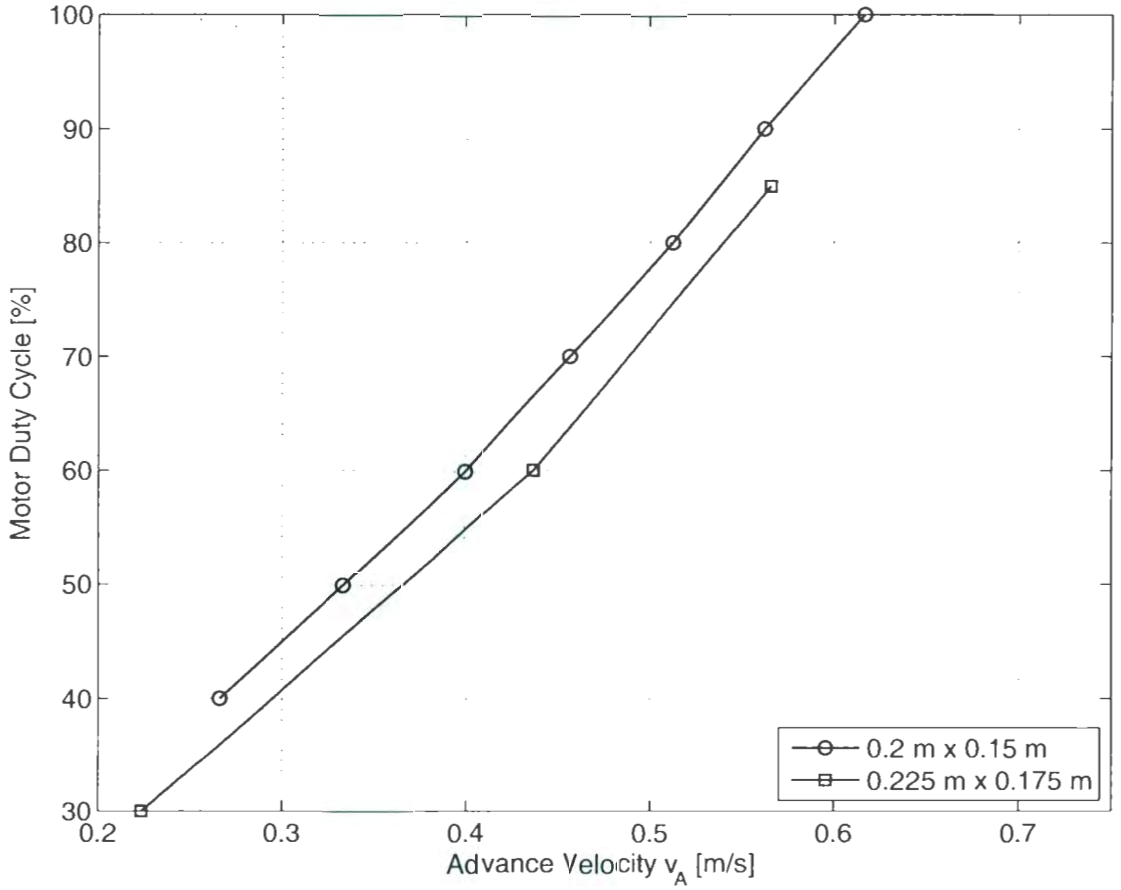


Figure 5.3: Motor duty cycle at a given advance velocity for different propellers where the battery voltage is 13.3 V

the plug was taken out of the tail-cone and placed in its housing above the thruster. The removal of the wings necessitated the re-ballasting of the glider. For this purpose weights were added to the wing attachment rails. The results of these tests are shown in Fig. 5.4.

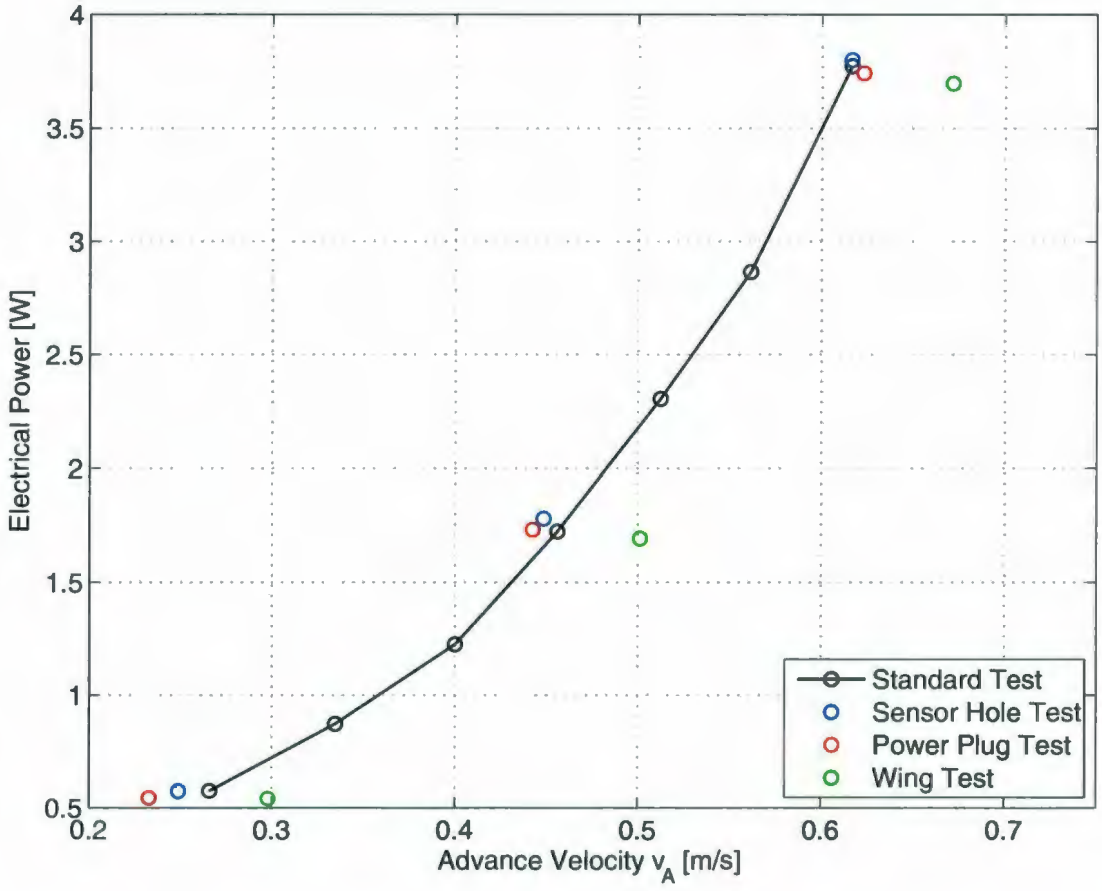


Figure 5.4: Power requirements at a given advance velocity for different external component configurations in the Memorial University of Newfoundland tow tank

From Fig. 5.4 the sensor hole test and the power plug test show higher power requirements for the same velocity when compared with the standard configuration. This increase is attributed to a decrease in propeller performance due to the disturbance of the inflow characteristics. The glider tests with no wings attached shows

lower power requirements for the same velocity when compared to the standard configuration. This reduction in power is attributed to the removal of the wings contribution to the vehicle drag. The tow tank self propulsion tests provide a comparison of the relative benefits of one configuration over another. The results are presented to inform the selection of a configuration warranting further testing.

## 5.2 Flume Tank Drag and Propulsion Tests

Using the selected vehicle configuration from the tow tank self propulsion tests, full scale drag and propulsion tests were performed at the Marine Institute's flume tank with a test section 8 m x 4 m x 22.5 m and capable of generating flow speeds from 0 to 1 m/s. These tests were done to verify the glider's hydrodynamic model and to evaluate its propulsion abilities. The general experimental setup is shown in Fig. 5.5 with an expanded view of the attachments to the glider in Fig. 5.6. In this setup the glider is attached to a guide wire which constrains the glider in yaw, pitch and roll. Drag measurements were then performed through a load cell attached to the forward end of the glider. Additional drag and self propulsion experiments were performed with an additional load cell attached to the aft end of the glider and pre-tensioned with a counterbalance weight. The forward attachment point was through the nose and the aft attachment was through a twin-bridle harness attached well outboard on each wing in order to provide clearance for the propeller to spin freely.

The drag tests were performed for the glider at zero angle of attack with wings, without wings and with wings and the counterbalance weight. Self propulsion tests were performed for the glider with the counterbalance weight by varying the voltage to the motor. These tests were performed for advance velocities of 0.2 to 1.0 m/s in increments of 0.1 m/s. For all tests the motor voltage $v$, electrical current $i$,

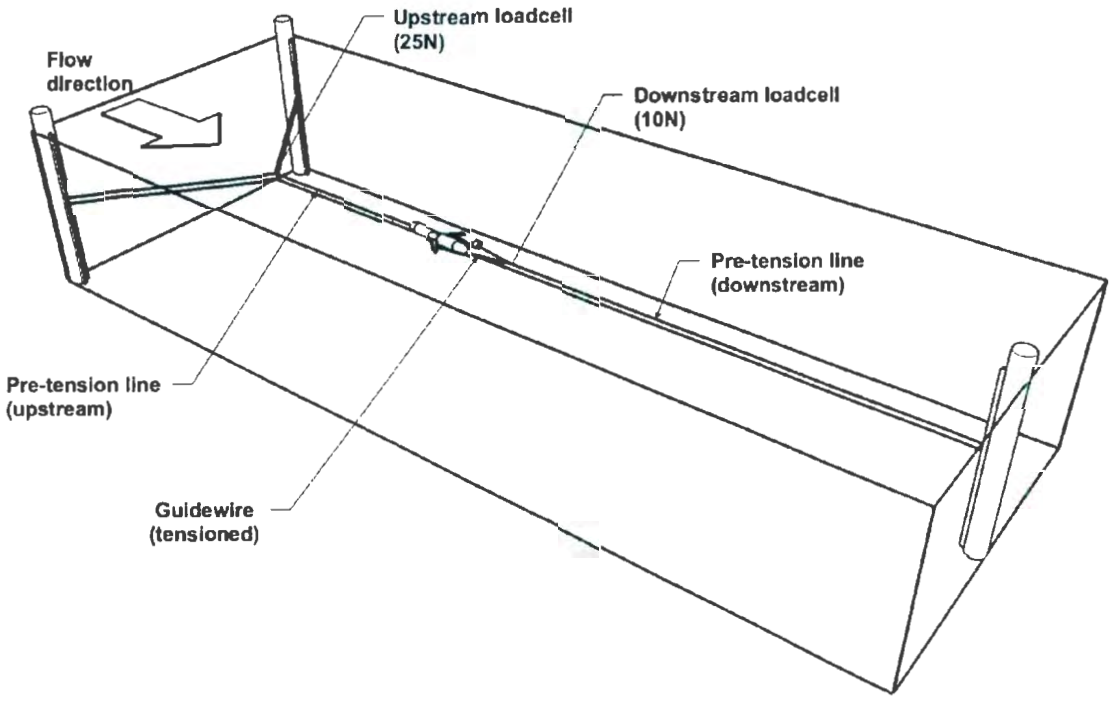


Figure 5.5: Marine Institute 4 m x 8 m x 22 m flume tank experimental setup for full scale glider hydrodynamic and propulsion testing.

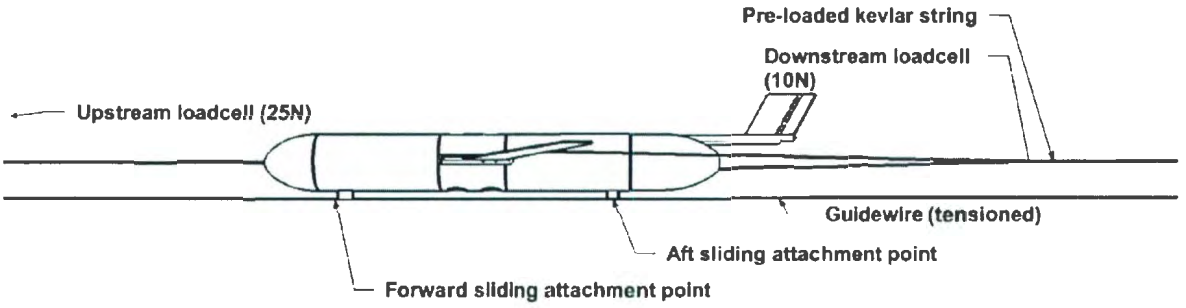


Figure 5.6: Expanded view of the Marine Institute flume tank experimental setup

and glider drag force $F_D$ were recorded. For the counterbalanced measurements, $F_D$ was calculated by subtracting the aft load cell readings from the forward load cell reading to remove the effect of the pre-loading. The Marine Institute's flume tank has been previously calibrated such that the advance velocity was recorded from the commanded set point and not actively measured. The effect of the harness attached to the wings for the counterbalance was quantified through the difference between the drag test with and without the counterbalance. The effect of the wings on the drag at zero angle of attack was also measured. The results of the drag forces exerted on the glider for the different tests are shown in Fig. 5.7.

After the harness drag is removed the measured drag is found to be higher than the drag at zero angle of attack in (2.6). At a speed of 0.3 m/s the measured drag force was 0.5 N and the predicted drag force was 0.34 N, a difference of nearly 50%. This difference can partially be attributed to parasitic drag in the test setup; however, the drag presented in (2.6) is based on indirect measurements and extrapolated to the zero angle of attack condition. Therefore, the measurements presented here are considered to be more accurate for this case. For the no wing tests the harness could not be used as it attaches to the wings. The measurements for this test were therefore subject to higher levels of noise as the force levels were low. Therefore, although the test shows the drag to be lower with the wings not attached, the data is determined to be less reliable.

For the tests with the propulsion module the force difference between the upstream and downstream load cell forces was measured as in Fig. 5.8 Where the force crosses zero in Fig 5.8, shown by crosses, is the electrical power required for the given velocity at steady state. This data as summarised in Fig. 5.9.

The amount of electrical power required for horizontal flight using the auxiliary propulsion module is shown to be

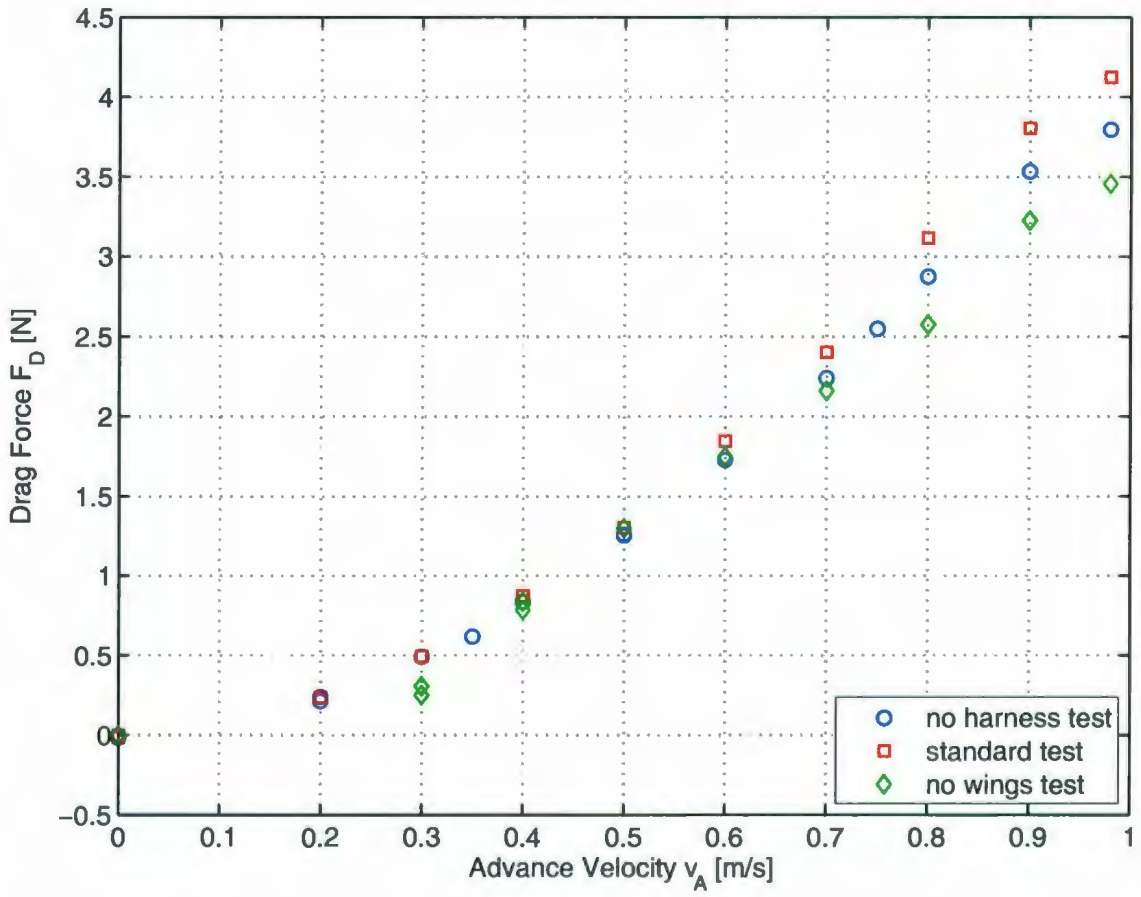


Figure 5.7: Marine Institute flume tank glider hydrodynamic drag force measurement calibration and testing.

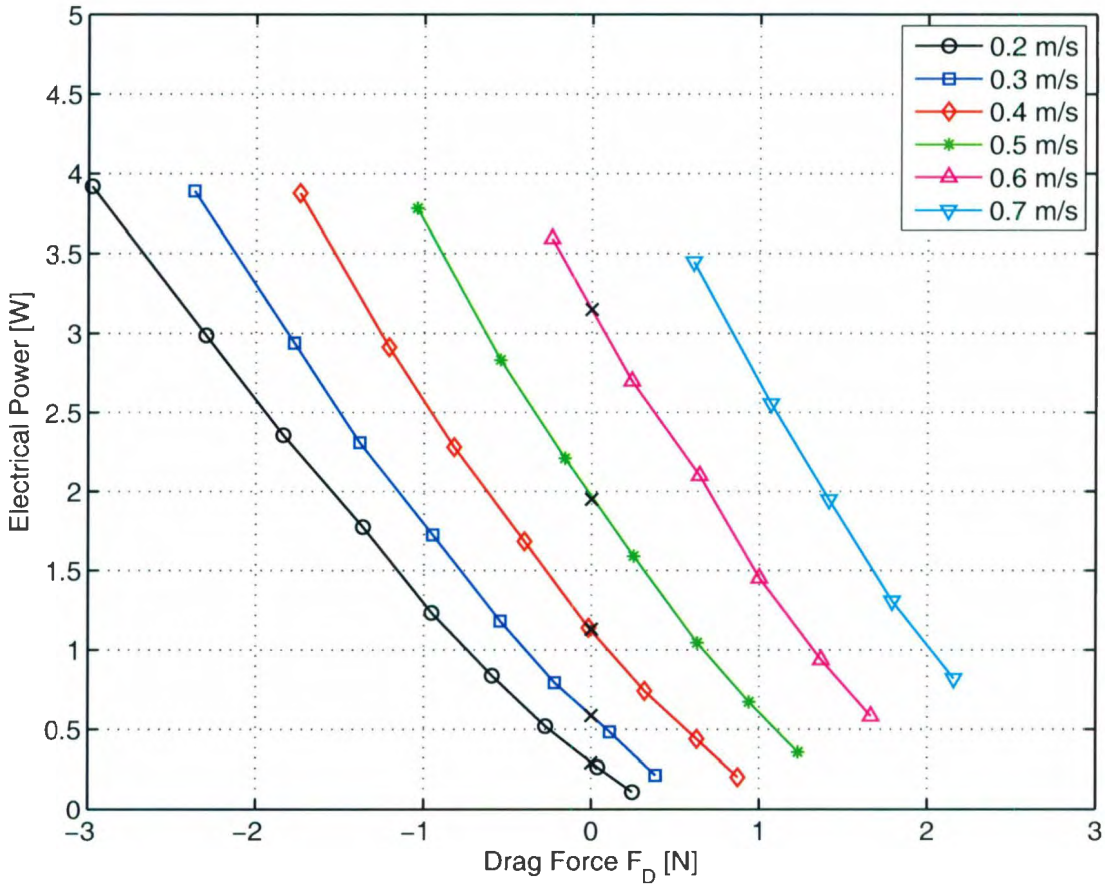


Figure 5.8: Self propulsion test results showing the force difference between the upstream and downstream load cell forces for a given electrical input power. The self propulsion condition for each curve is marked by an 'x'.

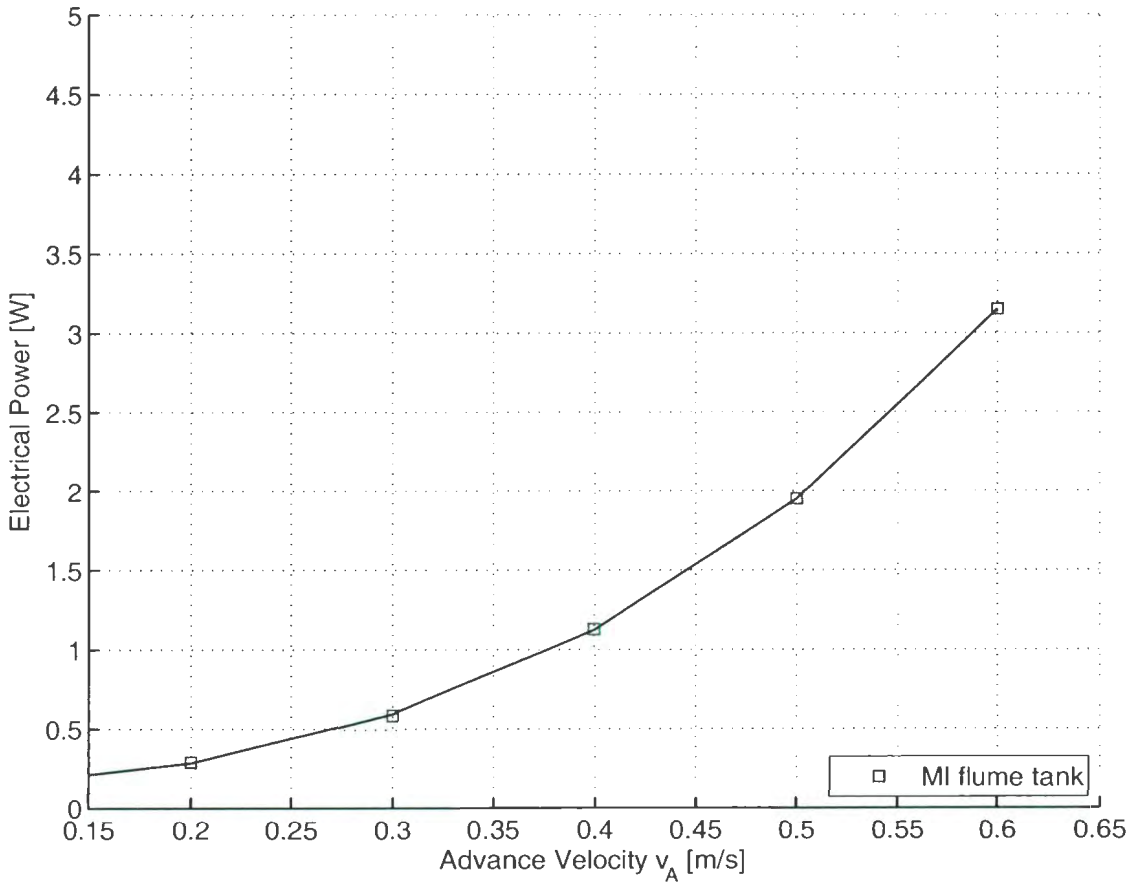


Figure 5.9: Self propulsion test results showing the power required for a given advance velocity at steady state

$$P_{prop} = P_2 v_A + P_3 v_A^2 + P_4 v_A^3 \tag{5.1}$$

using a polynomial cubic fit to the MI flume tank power data in Fig. 5.9. Where the coefficients for (5.1) are defined as in Tab. 5.1

| | |
|---|---|
| $P_2$ | 1.1 kg m/s |
| $P_3$ | -1.0 kg/s |
| $P_4$ | 13.2 kg/m |

Table 5.1: Coefficients for the electrical power to the propeller

From (2.18) and (2.6) a cubic relationship is expected for the hydrodynamic power which is different from the cubic polynomial in (5.1). A cubic polynomial was used as the correlation to the data was much stronger. This difference is attributed to the non simple body form of the vehicle and varied advance velocity resulting in flow transitions around sensors, wings and other body protrusions.

To define the input duty cycle to the hybrid proglet, the duty cycle as a function of glider advance velocity may be plotted as in Fig. 5.10 where the crosses mark where the force crosses zero. The duty cycle as a function of velocity may then be plotted as in Fig. 5.11

## 5.3 Drift at Depth Tests

The trajectory of an underwater glider is typically in a sawtooth-like pattern where the vehicle is gliding downwards and upwards. This pattern is not conducive to flying horizontally using the auxiliary propulsion module. To allow for horizontal flight two of the controllers which must be configured are the depth and pitch controllers. For a

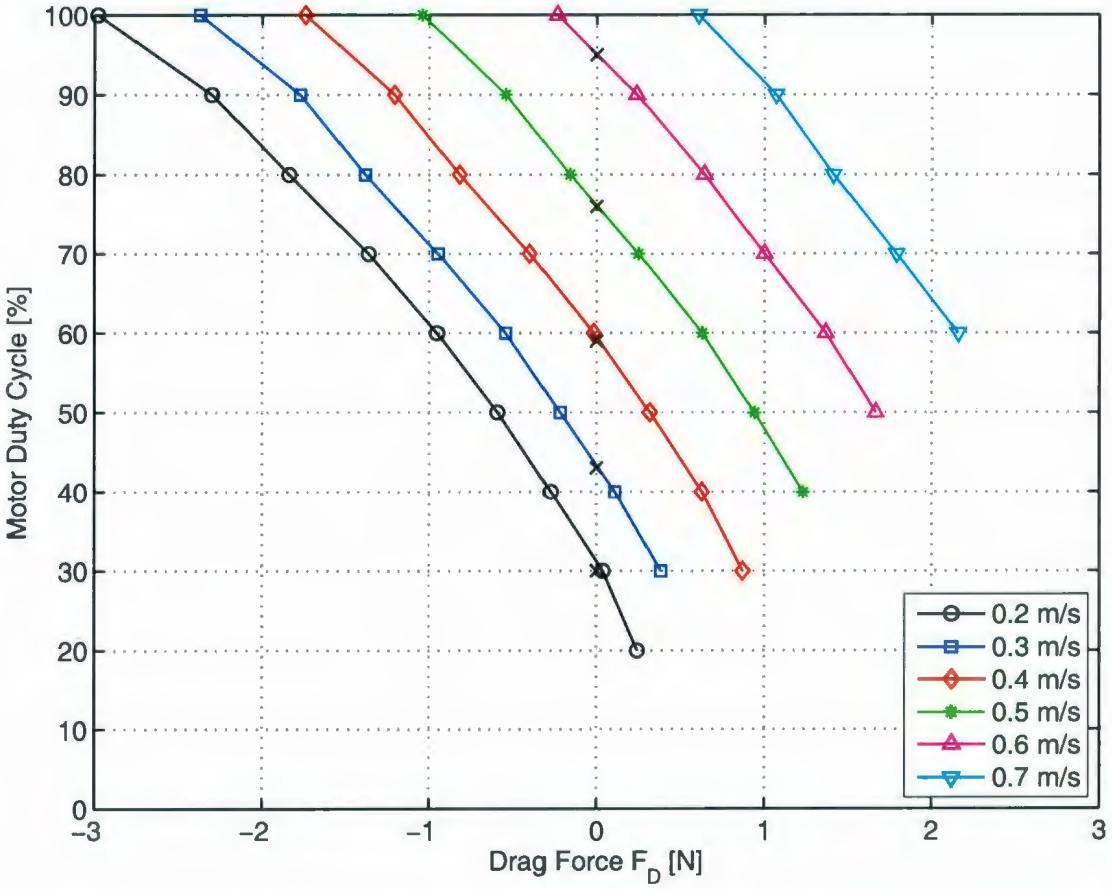


Figure 5.10: Self propulsion test results showing the force difference between the upstream and downstream load cell forces for a given motor duty cycle. The self propulsion condition for each curve is marked by an 'x'.

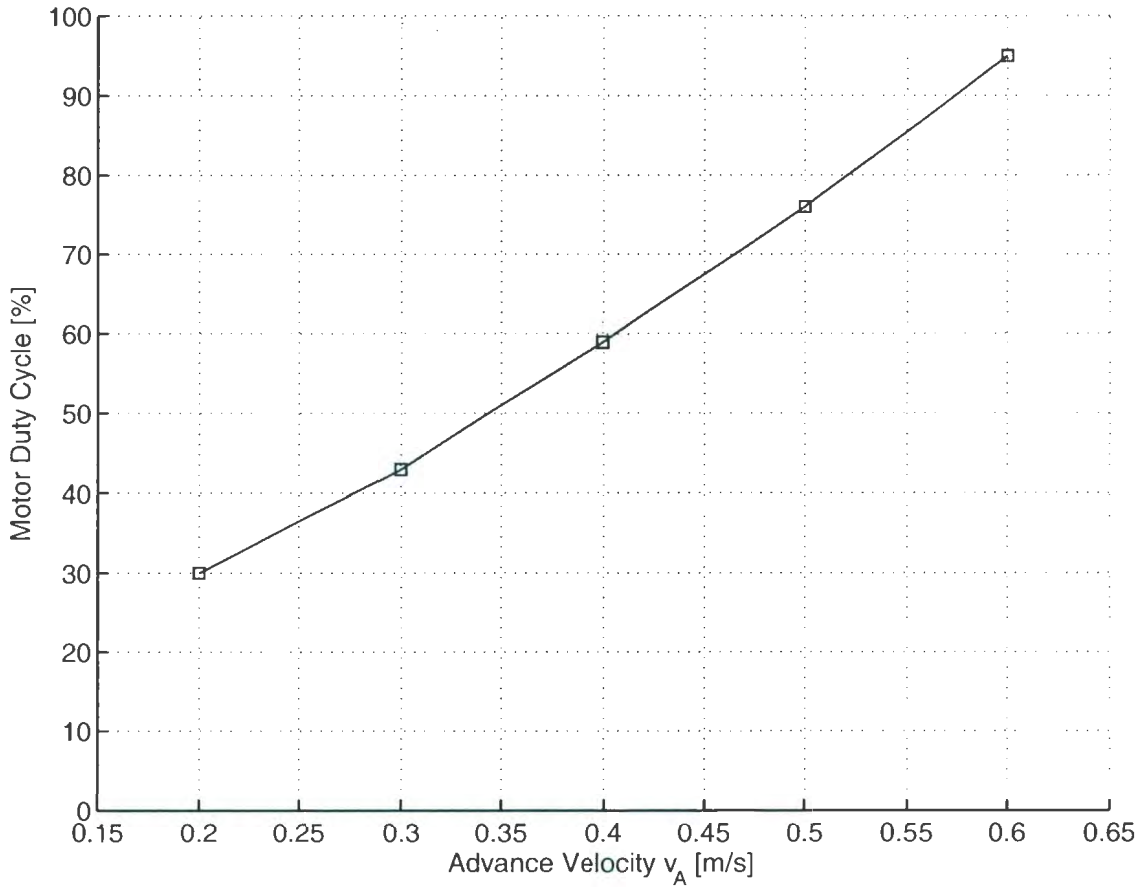


Figure 5.11: Self propulsion test results showing the motor duty cycle required for a given advance velocity at steady state.

glider with zero advance velocity, the pitch and depth controllers may be considered independent. This assumption does not hold for non-zero advance velocities as the pitch and depth are strongly coupled in this case. However, to tune the controllers the assumption is used as a starting point.

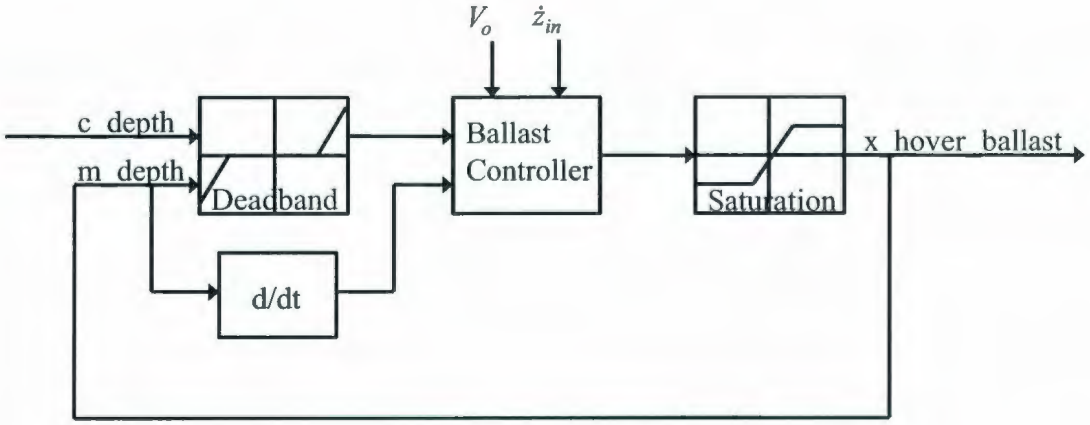


Figure 5.12: Depth controller structure

For testing purposes the drift-at-depth behaviour was used as it includes a pitch controller and depth controller. A diagram of the depth controller structure is shown in Fig. 5.12 where *c_depth* is the desired depth control point and *c_deadband* is the depth deadband for determining the hovering state. Initially, the neutral ballast lookup table mode was used but this did not allow for a predictable start value for *x_hover_ballast*, the output to the ballast system, as the table is unpopulated for the first dive after the glider is turned on making the response unpredictable. Therefore, an initial *x_hover_ballast* value $V_o$ based on experimental tests was used. The controller steps *x_hover_ballast* by the ballast pump delta value $\delta_{bp}$ depending on which state it determines the glider to be in. If the glider is outside of the hovering depth

zone defined by *c_depth* and *c_deadband*, the controller will decrement *x_hover_ballast* if it is above the depth zone and moving up and will increment *x_hover_ballast* if it is below the depth zone and moving down. If the vehicle is inside the depth zone there are two additional states in which the controller will change *x_hover_ballast*, moving down too quickly and moving up too quickly. The controller determines these states by comparing the measured depth rate $\dot{z}$ with the hovering depth rate $\dot{z}_h$ which is calculated using the user configurable maximum depth rate to be considered hovering $\dot{z}_{in}$ as in

$$\dot{z}_h = \frac{3}{4}\dot{z}_f\dot{z}_{in} \tag{5.2}$$

where the factory set hovering depth rate $\dot{z}_f = 0.1425$ m/s by default. If the glider is moving up and $|\dot{z}|$ is greater than the $\dot{z}_h$, the glider is moving up too fast and *x_hover_ballast* is incremented. Similarly, if the glider is moving down and $|\dot{z}|$ is greater than the $\dot{z}_h$, the glider is moving down too fast and *x_hover_ballast* is decremented. If the glider passes through all these states it is assigned to be in or hovering towards the drift depth zone in which the *x_avg_hover_ballast* argument is updated for the neutral ballast lookup table.

The depth controller was tuned experimentally by iterating the input parameters to the controller around the default vehicle parameters. Four tests were run to tune each of the parameters. The ballast pump delta value $\delta_{bp}$ tuning results are shown in Fig. 5.13. From these tests the resultant ballast pump delta value $\delta_{bp} = 2$. These tests also show significant spiking in the depth sensor reading. The intermittent spikes occurring when the vehicle passes 2 m were determined to be a result of the depth state changing from or to the at-surface state. The periodic spikes were determined to be a result of the relay switching the antenna from the GPS receiver to the Iridium

satellite modem while the vehicle was in the at-surface state. The tank's limited depth required changing the default at surface depth of 2 m to 0.5 m which prevents the depth sensor reading from spiking.

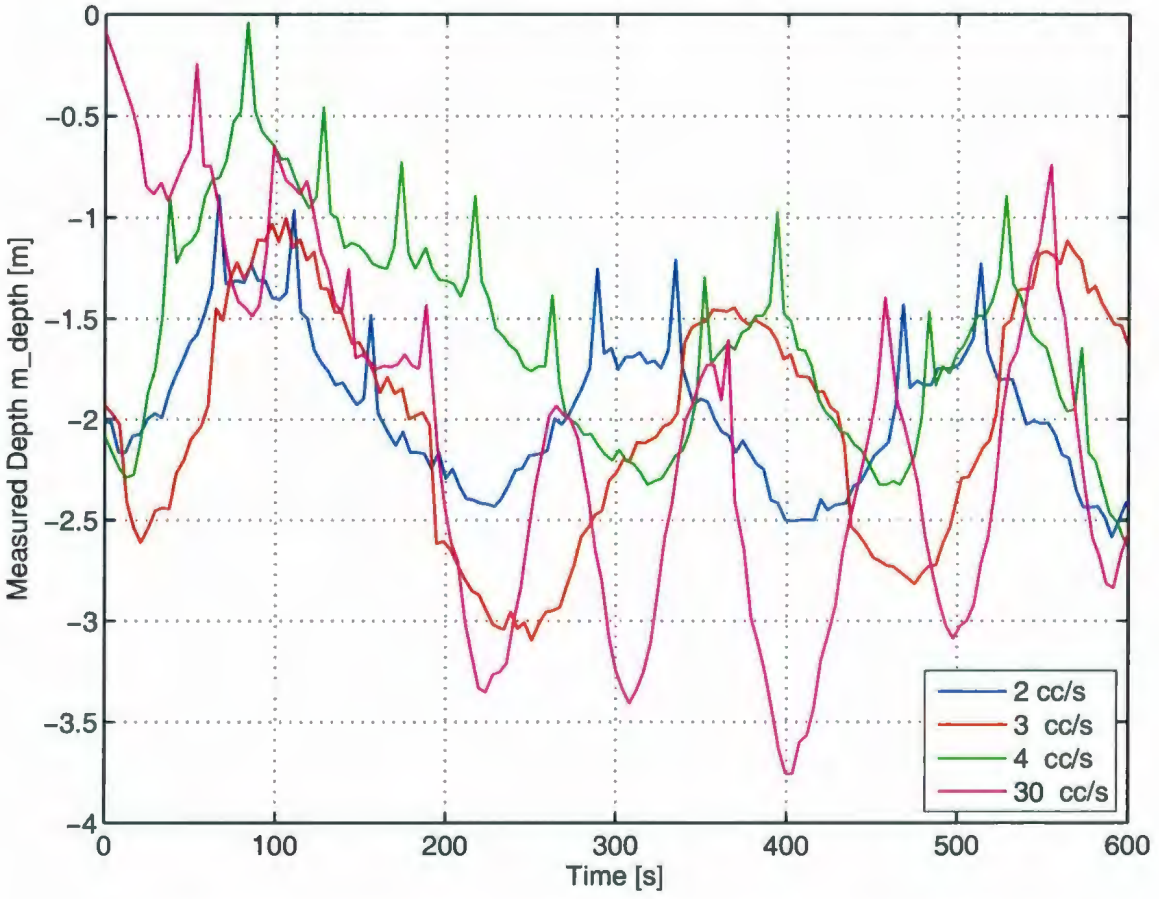


Figure 5.13: Depth controller ballast pump delta $\delta_{bp}$ tuning tests

The maximum hovering depth rate $\dot{z}_{in}$ tuning results are shown in Fig. 5.14.

The ballast bump initial value $V_o$ tuning results are shown in Fig. 5.15.

From these tests the resultant input parameters were taken as the ballast pump delta value $\delta_{bp} = 2$, the ballast pump initial value $V_o$ = -30 cc and $\dot{z}_{in} = 0.1$. It should be noted that the depth reading spiking was discovered half-way through the $\dot{z}_{in}$ tests and was present for all of the $\delta_{bp}$ tests therefore the resultant values may be affected.

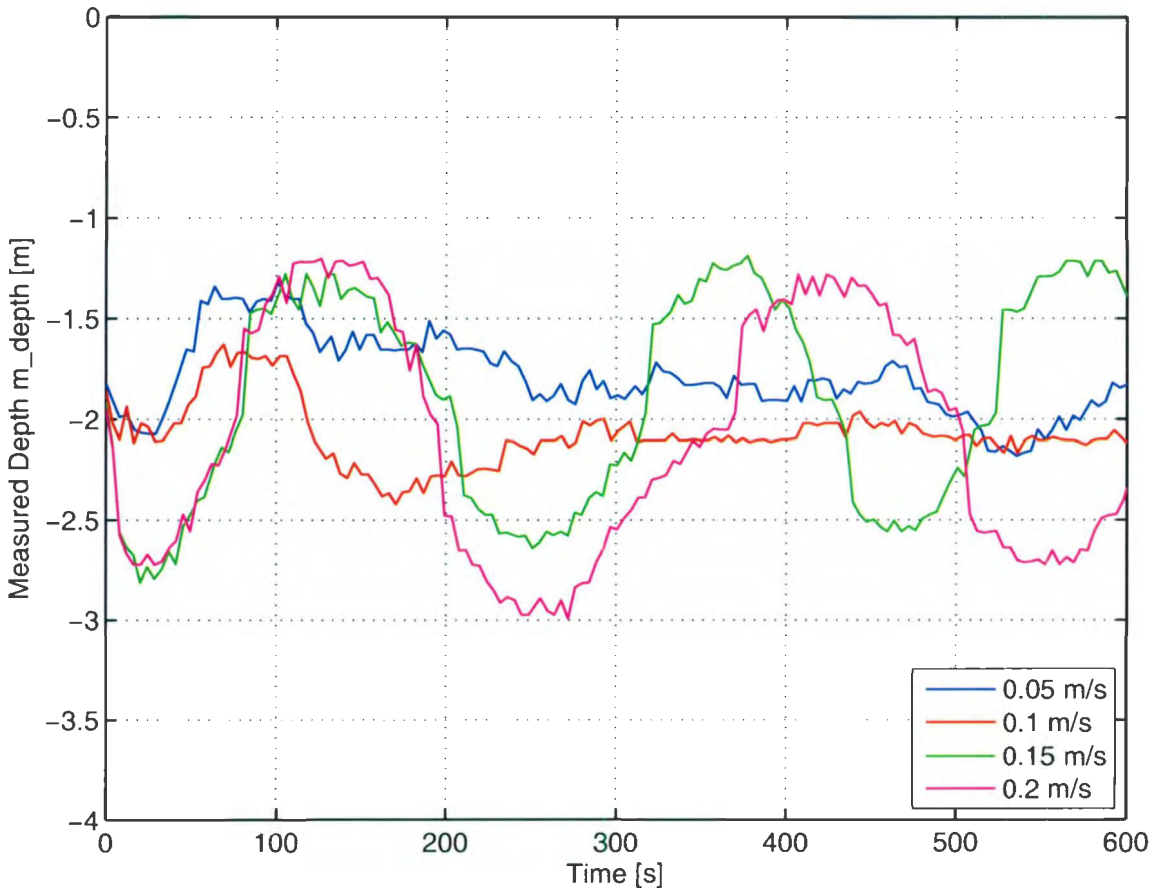


Figure 5.14: Depth controller maximum hovering depth rate $\dot{z}_{in}$ tuning tests

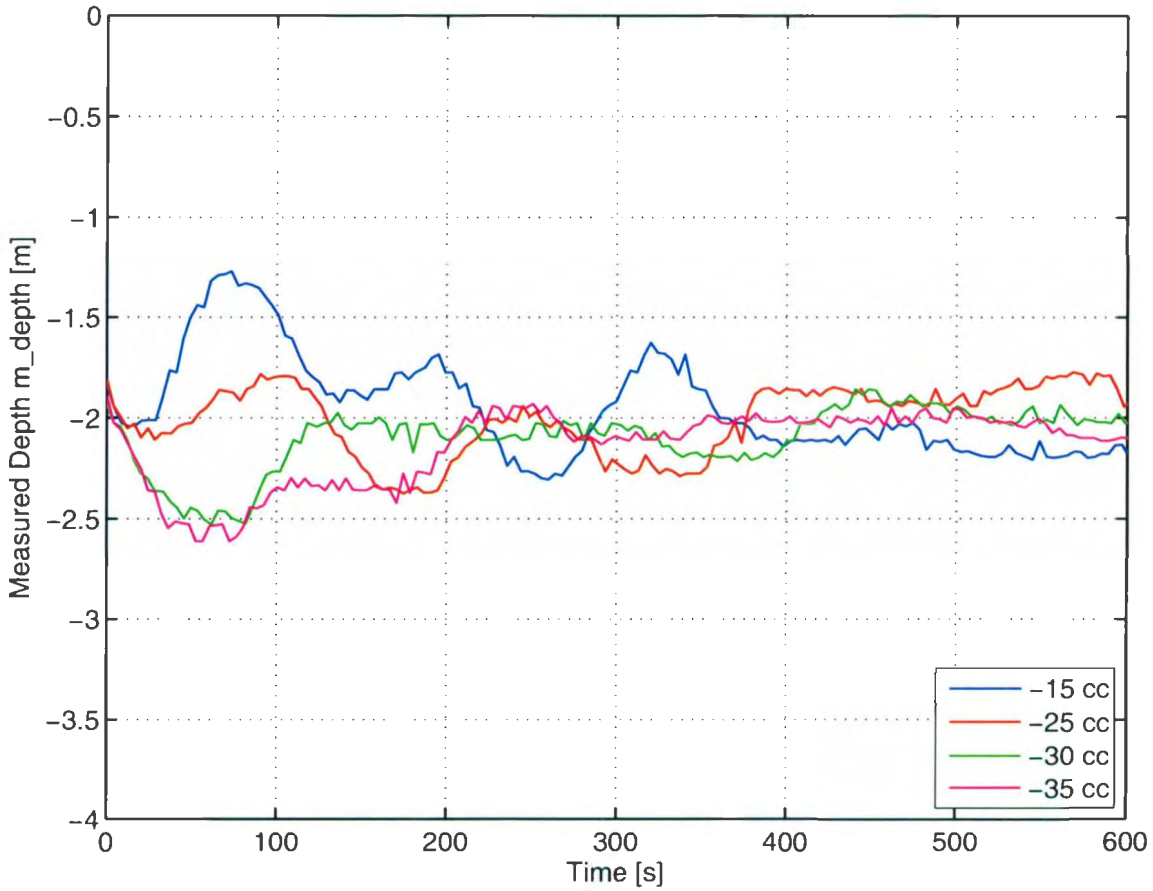


Figure 5.15: Depth controller initial ballast pump volume $V_o$ tuning tests

The pitch controller uses several limits and a proportional gain to maintain a set-point value using an internal mass shifting mechanism [31]. The controller inputs are taken from [31] as *u_pitch_max_delta_battpos* = 0.5 and *u_pitch_ap_gain* = -0.5 where the *u_pitch_max_delta_battpos* argument is the maximum change in inches for the mass shifting actuator and the *u_pitch_ap_gain* argument is the proportional gain for the controller. Additional arguments that were tuned include *u_pitch_ap_deadband* = 0.001 which is the deadband for the input to the controller in radians and *f_battpos_deadzone_width* = 0.03125 which is the deadband for the output to the mass shifter mechanism in inches.

Using these input parameters a test mission was run three times in the deep water tank to verify the stability of the pitch and depth controller. The results of these tests are shown in Fig. 5.16 and in Fig. 5.17.

From Fig. 5.16 it is shown that the depth controller reaches the hover depth zone of 2 m with a dead-band of 0.2 m within 5 minutes in all cases. Additionally, the maximum overshoot is limited to 0.5 m.

During these tests it was noticed that there was a natural pitching resonant frequency where the glider would oscillate slowly when disturbed. The fast Fourier transform (FFT) of the pitch data from Fig. 5.17 is shown in Fig. 5.18.

The FFT calculation shows a spike in the amplitude of the pitch response at frequencies of around 0.05 Hz to 0.06 Hz corresponding to a period of roughly 20 seconds and again around 0.005 Hz corresponding to a period of roughly 200 seconds. The higher frequency period of oscillation is attributed to the separation of the centre of gravity and buoyancy of the glider and the viscous damping of the vehicle while the lower frequency oscillations are the settling frequency of the controller. These tests show the glider's ability to control the pitch and depth under zero advance velocity and give modified values for the depth controller parameters.

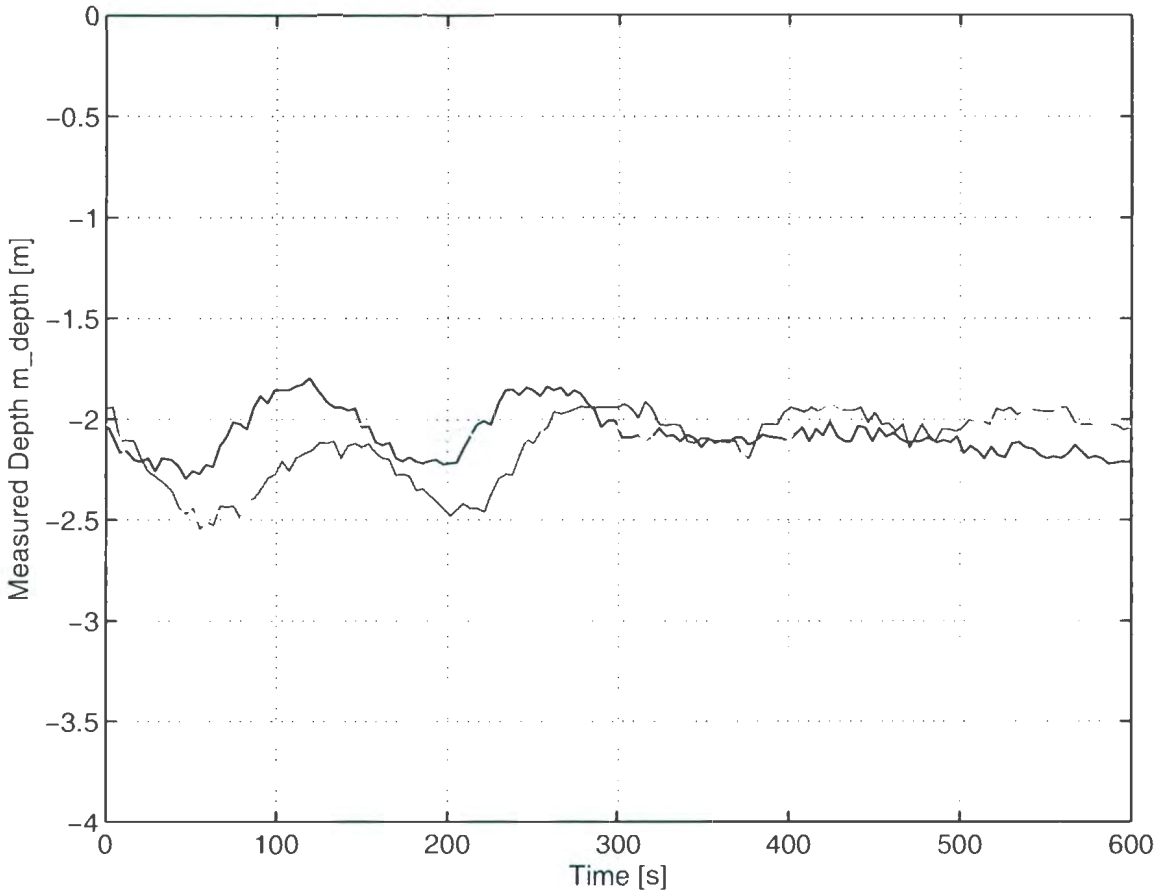


Figure 5.16: Depth measurements during the drift-at-depth test missions in the deep water test tank at Memorial University of Newfoundland

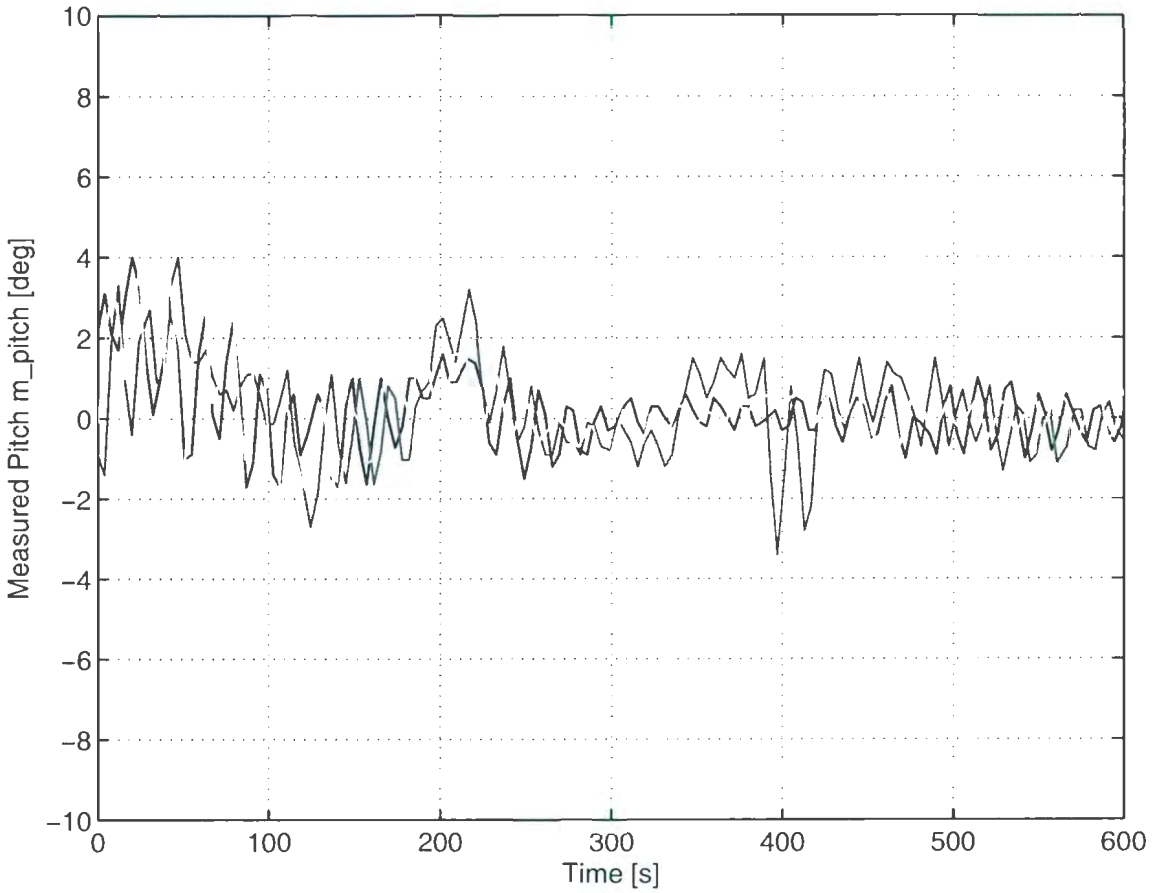


Figure 5.17: Pitch measurements during the drift-at-depth test missions in the deep water test tank at Memorial University of Newfoundland

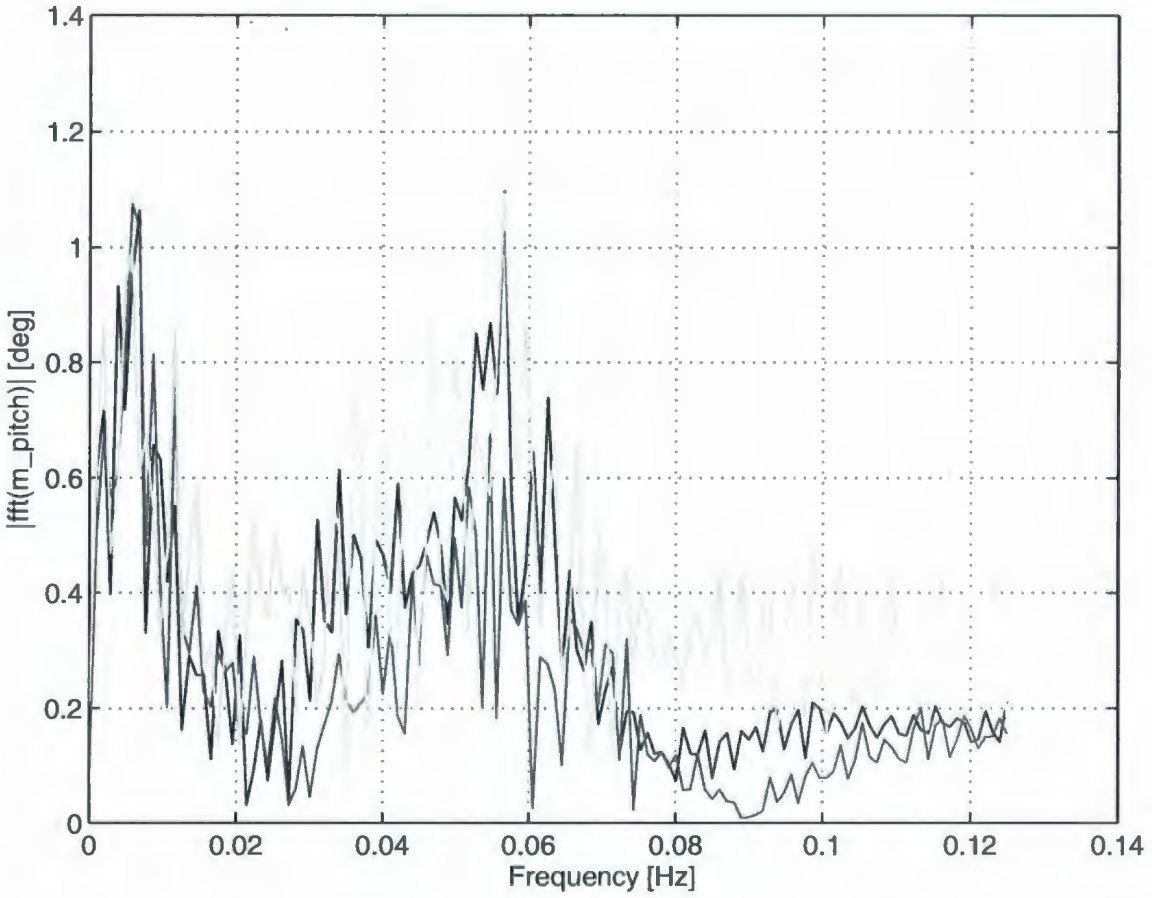


Figure 5.18: Fast Fourier transform of the pitch measurements during the drift-at-depth test missions in the deep water test tank at Memorial University of Newfoundland

## 5.4 Drive at Depth Tests

To evaluate the stability of the hybrid glider during horizontal flight the glider was flown using the auxiliary propulsion module and the tuned drift at depth behaviour from Section 5.3. Using the NRC-IOT's Ocean Engineering Basin (OEB) (L: 70 m, W: 35 m, D: 3 m ) a total of 25 tests were performed. During these tests five different missions were flown, each mission having a different motor setting corresponding to speeds of 0.2 m/s to 0.6 m/s as in Fig. 5.11. The propulsion module for these missions turns on during the hovering state of the mission which lasts for a specific time such that the total distance covered is 30 m. A depth of 1.6 m was set as it is approximately halfway between 0.5 m and 3 m. Tests were flown with a fixed rudder angle of zero degrees for straight ahead travel. The inertial measurement unit was also installed in the vehicle to record the vehicles attitude, angular rates and accelerations. The depth during the hovering behaviour until the behaviour terminates is shown in Fig. 5.19

The results in Fig. 5.19 show the glider's depth is well controlled for the 0.2 m/s test. As the velocity increases the lift on the vehicle increases shown by an increase in the amplitude of the depth oscillations. At slower speeds the lift acts to stabilise the depth controller when compared with the MUN deep water test tank tests in which the glider had zero advance velocity. The pitch results for the same tests are shown in Fig. 5.20

The pitch results show the vehicle is able to control the pitch to zero degrees. There are several instances where a sudden decrease in the pitch for 0.4 and 0.6 m/s is present. This pitching disturbance is also visible in the depth figure for the same velocities as sudden change in depth. However, these disturbances are caught by the controller and corrected. The natural pitching motion of the vehicle is also present

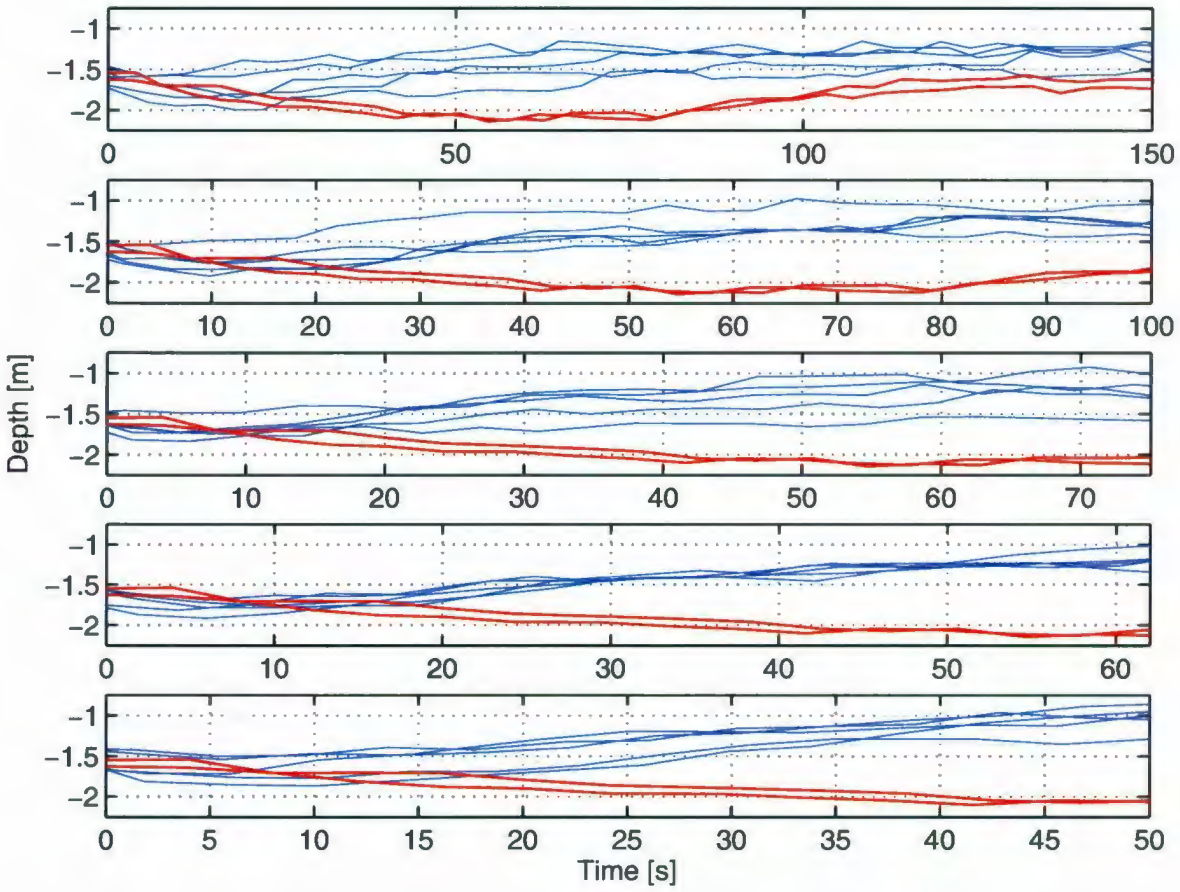


Figure 5.19: Depth results for the hybrid glider flying 30 m horizontally at 1.6 m in the Ocean Engineering Basin shown in blue. From top to bottom the advance velocity of the vehicle is 0.2 m/s, 0.3 m/s, 0.4 m/s, 0.5 m/s and 0.6 m/s. The depth results from the deep water test tank at Memorial University of Newfoundland are overlayed in red and adjusted to the same depth setpoint

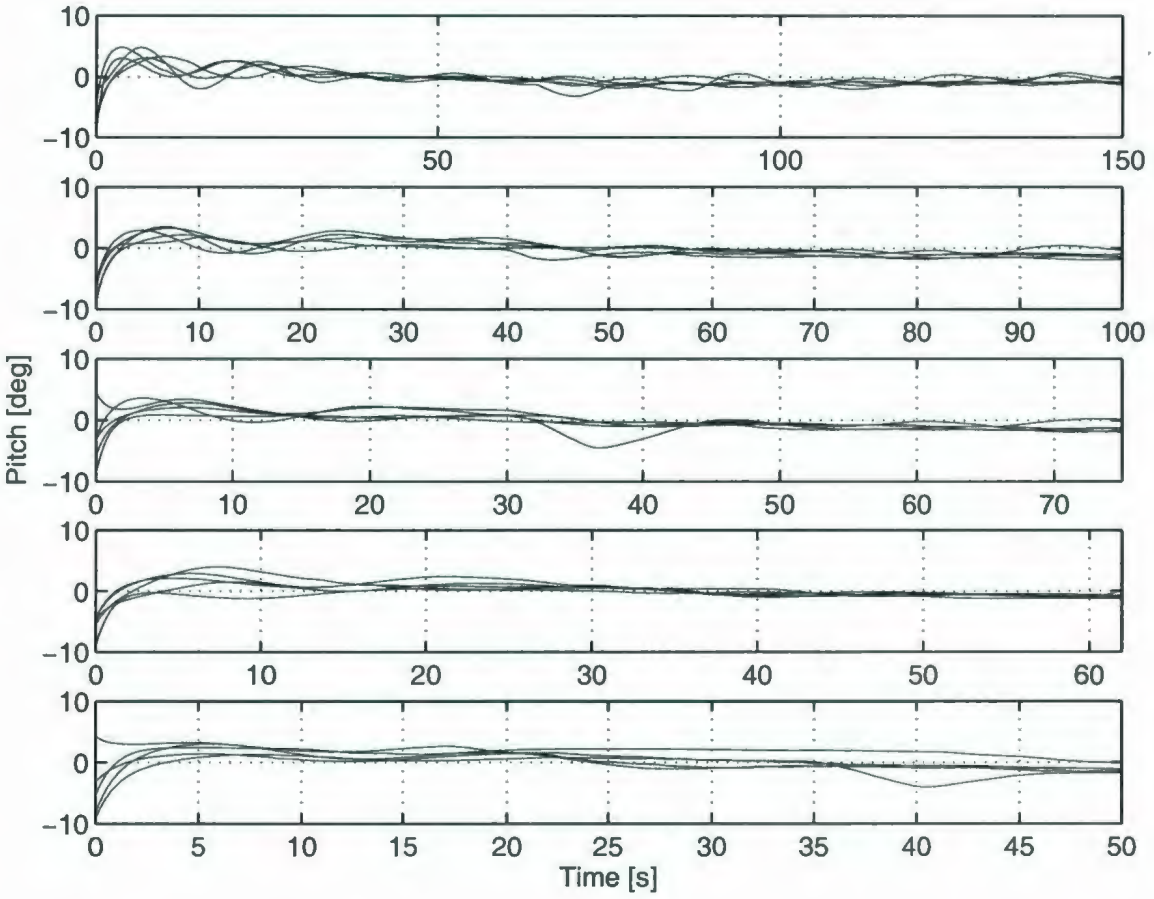


Figure 5.20: Pitch results for the hybrid glider flying 30 m set to a pitch angle of zero degrees. From top to bottom the advance velocity of the vehicle is 0.2 m/s, 0.3 m/s, 0.4 m/s, 0.5 m/s and 0.6 m/s.

in this data as shown by the fast Fourier transform (FFT) of the pitch data shown in Fig. 5.21

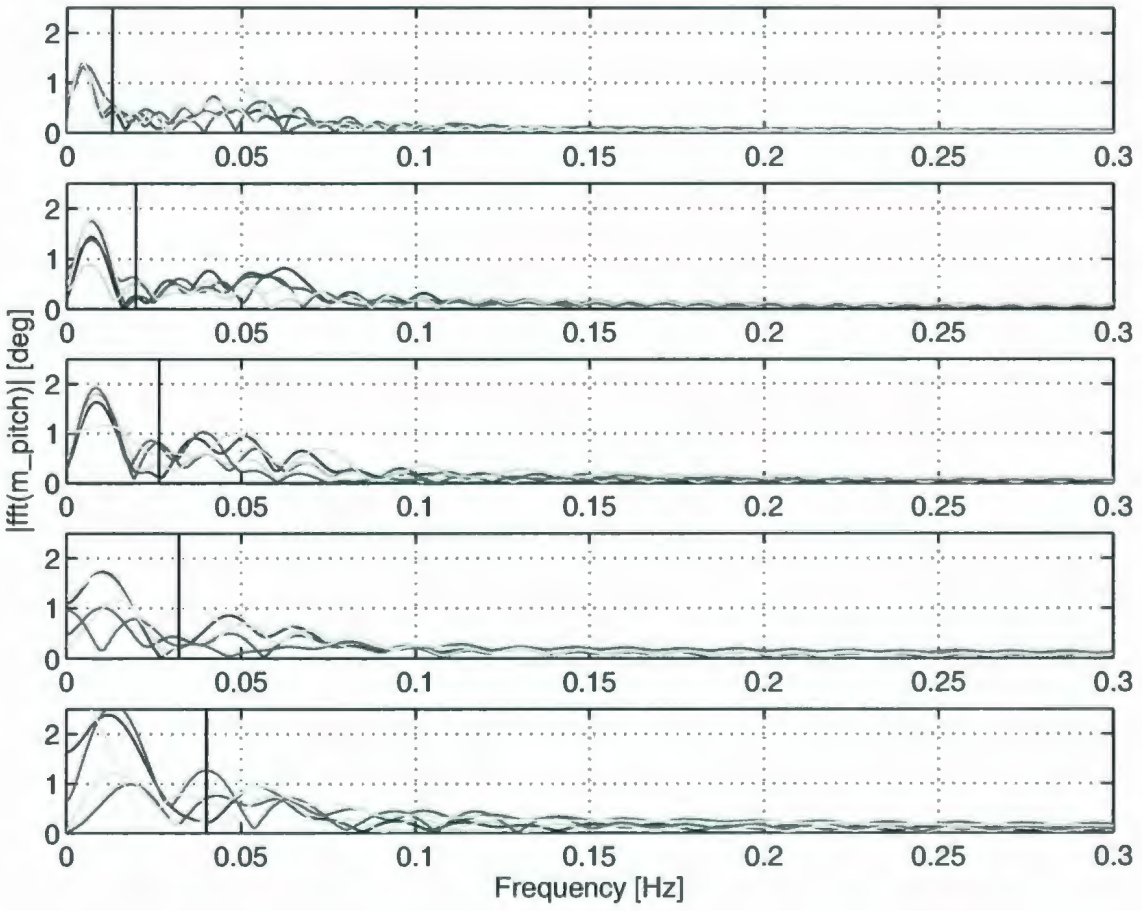


Figure 5.21: Fast Fourier transform results of the pitch data from the Ocean Engineering Basin tank tests. From top to bottom the advance velocity of the vehicle is 0.2 m/s, 0.3 m/s, 0.4 m/s, 0.5 m/s and 0.6 m/s. The black vertical lines indicate the minimum frequency corresponding to a period equal to half of the total sample time

The natural pitching motion peak still appears at around 0.05 Hz corresponding to a period of around 20 s. Additionally, the amplitude of the oscillations increases with increasing advance velocity. However, in the FFT analysis of the pitch data

the total sampling time of each test must be taken into consideration to establish the reliability of the lower end frequencies. It is considered that frequencies corresponding to periods less than half of the total sampling time are not reliable.

Another variable which must be considered is change in roll due to the applied torque from the motor. The raw roll data is plotted as a time series in Fig. 5.22

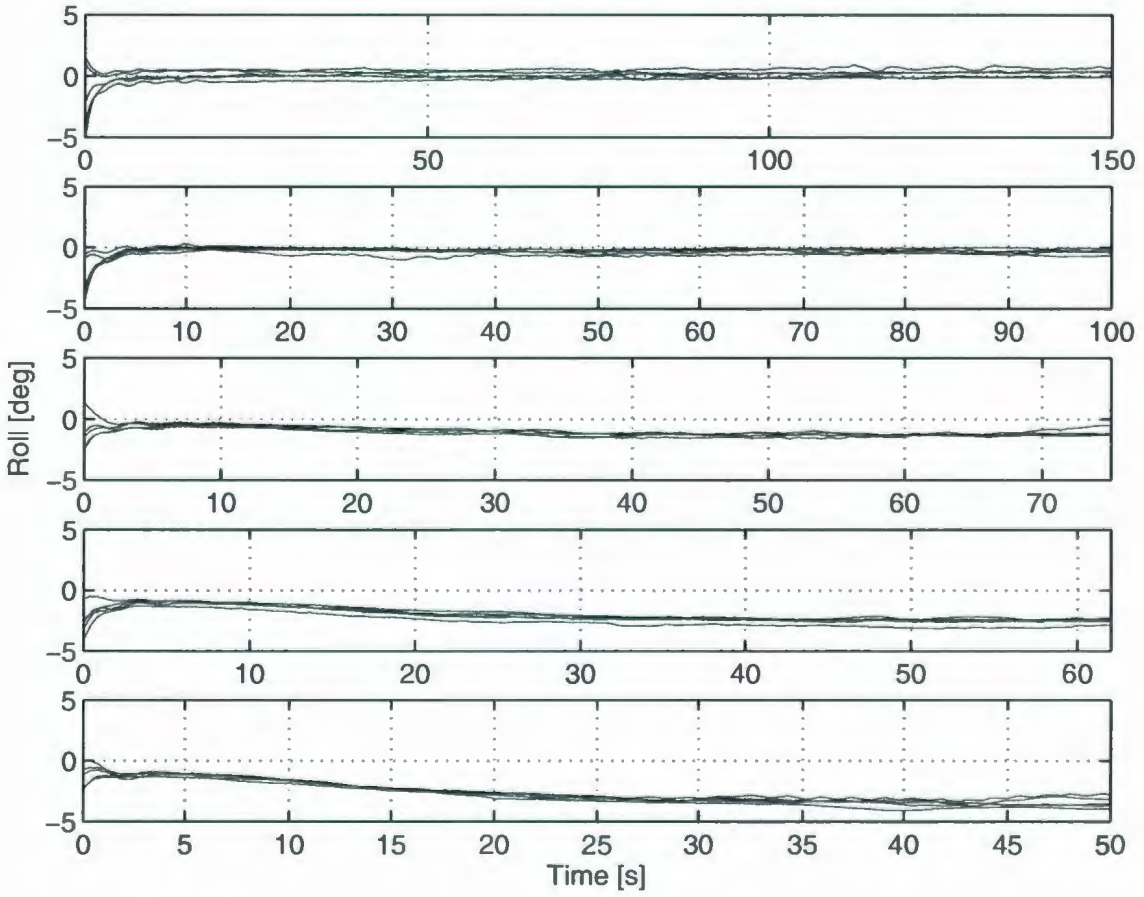


Figure 5.22: Roll results for the hybrid glider flying 30 m in the OEB test tank. From top to bottom the advance velocity of the vehicle is 0.2 m/s, 0.3 m/s, 0.4 m/s, 0.5 m/s and 0.6 m/s.

From Fig. 5.22 the roll of the vehicle is seen to increase with the applied torque. The increase in roll is balanced with the restorative force due to the righting moment.

The righting moment may be calculated in this case as in (5.3)

$$H = \frac{\tau_{sh}}{F_g \sin(\phi)} \tag{5.3}$$

where $H$ is the righting moment arm, $\tau_{sh}$ is the shaft torque, $F_g$ is the force due to gravity and $\phi$ is the roll. This calculation is applied to the data shown in Fig. 5.22 using the measured roll and torque to find the righting moment for the OEB tank tests as in Fig. 5.23. For this calculation the vehicle mass was measured to be 52 kg.

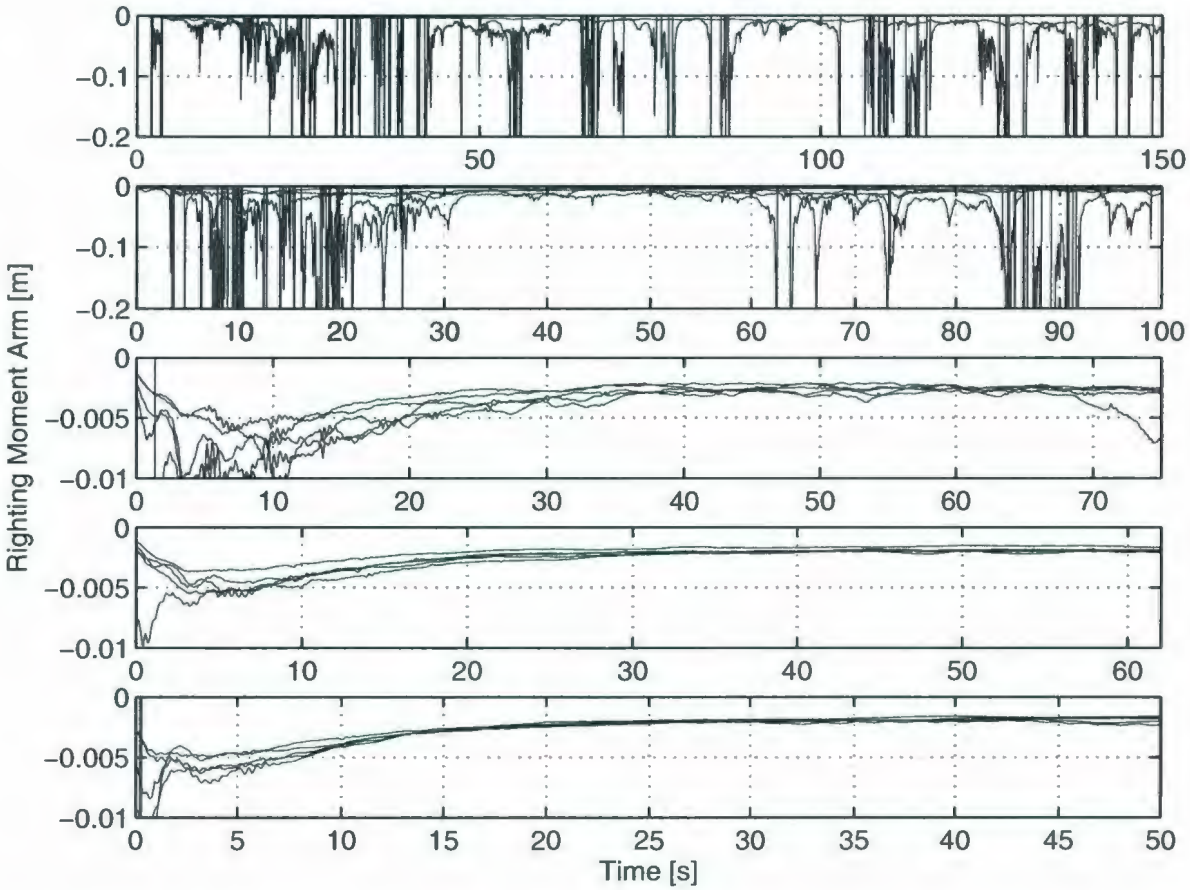


Figure 5.23: Righting moment results for the hybrid glider flying 30 m in the OEB test tank. From top to bottom the advance velocity of the vehicle is 0.2 m/s, 0.3 m/s, 0.4 m/s, 0.5 m/s and 0.6 m/s.

The resultant righting moment is shown to be around 2E-3 m for advance velocities for 0.4-0.6 m/s. However, the noise in the roll measurements caused a significant degree of noise in the calculation results for 0.2 and 0.3 m/s. This noise is attributed to the very small change in roll due to the low applied motor torque, resulting a roll value which remains very close to zero. Since the righting moment is dependant on the inverse of $\sin(\phi)$, a value of the roll $\phi$ close to zero causes unstable values.

These tests show the ability of the hybrid glider to fly at a desired depth in a straight line on the horizontal plane. The length of the OEB testing tank did not allow for a conclusive demonstration of the controllability and stability of the controllers used. The OEB tests show that glider is capable of driving at depth by tuning the glider's existing control parameters and no large instabilities are present.

## 5.5 Range Estimates

The range of an underwater vehicle is a function of the energy available, power consumed and advance velocity [75]. Specifically, the total power consumption in the vehicle divided by the velocity gives the energy consumed per meter. The range is then given by dividing the total energy available by the energy consumed per meter. This calculation may be extended to buoyancy driven gliders where the range $R_{bp}$ becomes

$$R_{bp} = \frac{E\dot{x}}{P_{bpc} + P_h + P_l} \tag{5.4}$$

where the ballast pump load $P_{bpc}$ is the propulsive load from 2.14, the available energy $E = 8$ MJ, the hotel power or computational power $P_h = 0.2$ W and the sensor load $P_l = 1$ W [18]. The glider horizontal velocity $\dot{x}$ is based on the glide path angle $\xi$ and depth rate $\dot{z}$ as in 2.17.

For a propeller driven vehicle the range $R_{prop}$ becomes

$$R_{prop} = \frac{Ev_A}{P_{prop} + P_h + P_l} \tag{5.5}$$

where the propulsion module load $P_{prop}$ is defined as in 5.1. The propulsive velocity $v_A$ varies from 0.2 to 0.67 m/s, the maximum speed from the MUN tow tank self propulsion results. For a glider operating with a bathtub shaped trajectory, the buoyancy engine brings the glider to depth and the propeller is used at that point to move the glider horizontally by a distance $d_{prop}$ until it is time for the next surfacing at which point the buoyancy is increased to bring the glider back to the surface. In this case the range $R_{hybrid}$ is

$$R_{hybrid} = \frac{E(\dot{x}\Delta_{bp} + v_A\Delta_{prop})}{P_{bpc}\Delta_{bp} + P_{prop}\Delta_{prop} + P_h + P_l} \tag{5.6}$$

where $\Delta_{bp}$ and $\Delta_{prop}$ represent the ratio of time for which each propulsion method is active relative to the total time as in

$$\Delta_{bp} = \frac{2t_{bp}}{2t_{bp} + t_{prop}} \tag{5.7}$$

and

$$\Delta_{prop} = \frac{t_{prop}}{2t_{bp} + t_{prop}} \tag{5.8}$$

The time the propeller propulsion is active $t_{prop}$ is defined as

$$t_{prop} = \frac{d_{prop}}{v_A} \tag{5.9}$$

where the horizontal distance travelled $d_{prop}$ =2500 m. The time the ballast pump propulsion is active $t_{bp}$ is taken from (2.15).

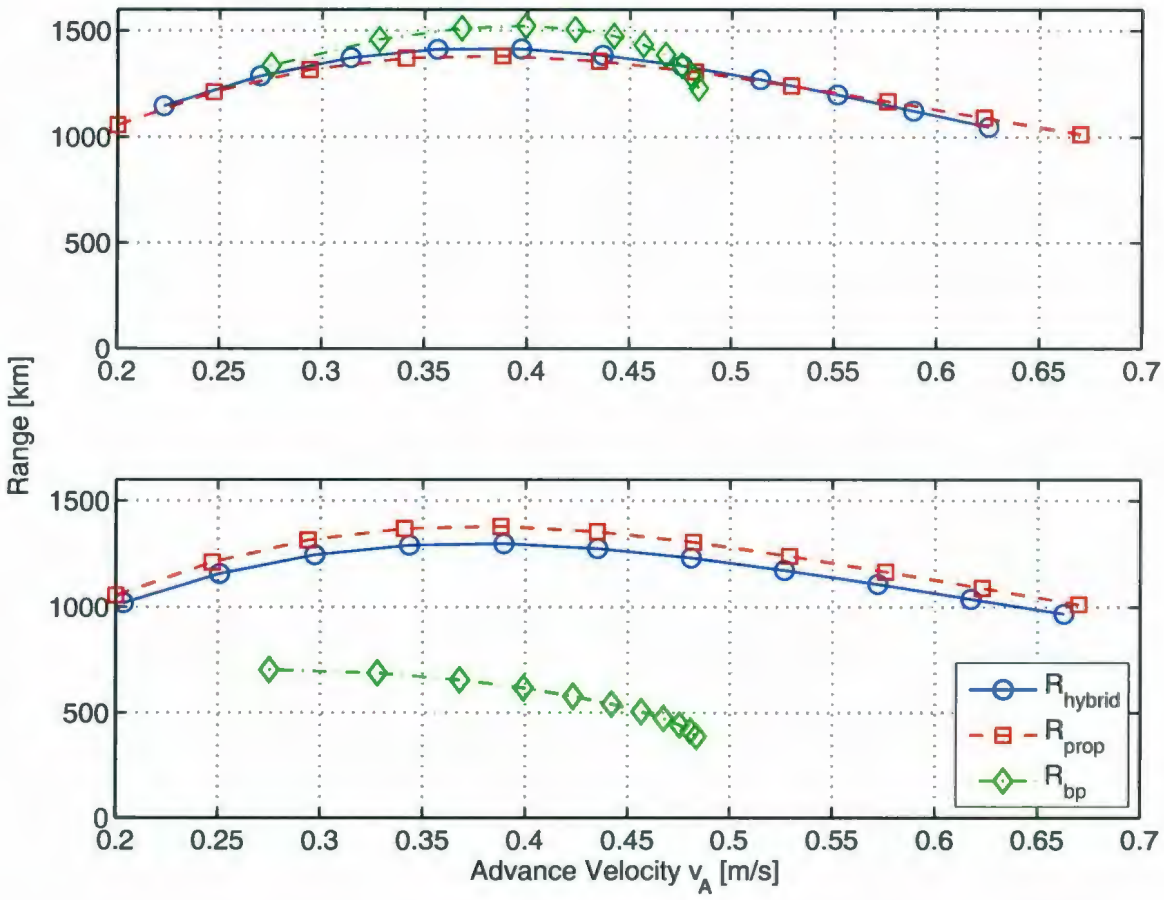


Figure 5.24: Estimated range for a glider operating in hybrid, propeller only and ballast pump only modes where the top is for full 200 m depth dives and the bottom is for 10 m average depth dives

If $R_{bp}$, $R_{prop}$ and $R_{hybrid}$ are plotted as functions of the vehicle's horizontal velocity it can be seen that the buoyancy-driven glider and the hybrid glider exhibit similar range capabilities as shown in part a) of Fig. 5.24 when the glide depth $z$ = 200 m. However, the hybrid glider is capable of travelling at faster overall speeds and has a significantly larger range when compared to a conventional glider with small glide depths of $z$ = 10 m as shown in part b) of Fig. 5.24. It should also be noted that in Fig. 5.24 the horizontal distance travelled while at depth $z$, $d_{prop}$ is set to 2500 m. If $d_{prop}$ is decreased the vehicle spends more time gliding to depth relative to moving horizontally at depth causing $R_{hybrid}$ and the time averaged horizontal velocities decrease towards the $R_{bp}$ curve. To illustrate this behaviour two cases may be examined at the extreme ends, the case of the vehicle with $t_{bp}$ = 0 s and with $t_{prop}$ = 0 s. With $t_{bp}$ = 0 s, the vehicle stays at the surface and the buoyancy engine is not used at all. The range for this case is shown by $R_{prop}$. When $t_{prop}$ = 0 s, the propeller is not used at all and the vehicle behaves as an unmodified glider. The range for this case is shown by $R_{bp}$. This model does not take into account settling times for the vehicle changing between operational modes or at the top or bottom of the inflection of the glide path. Additionally, the time spent on surface is neglected. These omissions become increasingly important for gliding vehicles with shallow inflections as transitions occur with greater frequency. The hybrid glider propulsion module is therefore considered to operate with a similar performance to the buoyancy driven glider.

# Chapter 6

# Summary

An auxiliary propulsion module for a 200 m Slocum glider has been presented. The module greatly enhances the operational abilities of underwater gliders by enabling horizontal flight and increased speed capabilities. A simplified hydrodynamic model under the assumption of a zero angle of attack was used to design the module. Using this model, the initial component selection was accomplished through matching the motor, gearbox and measured propeller efficiencies. The propulsion module's performance was confirmed through propulsion tests in the flume tank at Memorial University of Newfoundland (MUN). Upon integration of the propulsion module into the glider, self propulsion tests were conducted in the 4 m x 8 m x 22 m flume tank at the Marine Institute (MI). Direct measurements of the drag force for the glider at zero angle of attack were also performed in the MI flume tank in order to verify the simplified hydrodynamic model; the measured drag force was found to be 0.5 N for an advance velocity of 0.3 m/s, nearly 50 % higher than the predicted value of 0.34 N at 0.3 m/s. Additional, directionally constrained, self propulsion tests were executed in the 53 m long MUN tow tank to verify the performance of the hybrid glider. The self propulsion tests show that the propulsion module is capable of moving the glider

horizontally at 0.3 m/s while consuming 0.6 W of battery power and at 0.67 m/s using 4.25 W.

To analyse the stability of the vehicle while under horizontal flight the pitch and depth controller were analysed and tuned. These tests were performed in the deep water test tank at MUN. From these tests it was shown that the vehicle exhibits a natural pitching motion. Additionally, it was shown that the depth and pitch of the vehicle were controllable under the zero velocity condition. Using the parameters determined from these tests the vehicle was driven at a constant depth, heading and pitch over a distance of 30 m. These tests showed the controllability of the vehicle at speed.

A comparison of the power requirements for propulsion of conventional gliders with the power consumed by this auxiliary propulsion module shows that the power consumed is about the same for full depth glides to 200 m. When used only for shallow water operations, the time averaged power consumed by this module is less than that by the conventional glider. This performance results in the potential for equal range for hybrid and conventional modes of operation when used appropriately; additionally, the auxiliary propulsion module enables new modes of operation such as movement in the lateral plane and higher overall velocities.

The hybrid glider's expansion of abilities opens up many new roles and opportunities for collaborations using underwater gliders. The auxiliary propulsion module is capable of operating at depths over 1000 m, allowing it to be transferred to 1000 m gliders as well. The 1000 m variant of the Slocum glider would require only some wiring and software additions to integrate the module into its systems. Potential future collaborations will involve investigating the propulsive performance of the auxiliary propulsion versus the deep glider as the ballast system on the deep gliders uses a pump rather than a piston to maintain efficiency in deep water.

Future work with the hybrid glider will involve extended stability testing in the ocean over a longer distance. The navigational behaviours which update the glider mission coordinates need to be developed. Following this work the propulsion module will require testing in the various roles envisioned for it.

# Bibliography


[1] J. Graver, *Underwater gliders: Dynamics, control and design.* PhD thesis, Princeton University, 2005.

[2] C. Williams, R. Bachmayer, and B. deYoung, "Progress in predicting the performance of ocean gliders from at-sea measurements," in *Proc. of IEEE Oceans*, pp. 1–8, Sept. 2008.

[3] J. Graver, R. Bachmayer, N. Leonard, and D. Fratantoni, "Underwater glider model parameter identification," in *Proc. 13th Int. Symp. on Unmanned Untethered Submersible Technology (UUST)*, 2003.

[4] H. Stommel, "Direct measurements of sub-surface currents," *Deep Sea Research (1953)*, vol. 2, no. 4, pp. 284 – 285, 1955.

[5] J. C. Swallow, "A neutral-buoyancy float for measuring deep currents," *Deep Sea Research (1953)*, vol. 3, no. 1, pp. 74 – 81, 1955.

[6] R. Davis, D. Webb, L. Regier, and J. Dufour, "The autonomous lagrangian circulation explorer," *Journal of Atmospheric and Oceanic Technology*, vol. 9, no. 3, pp. 264–285, 1992.

[7] R. E. Davis, P. D. Killworth, and J. R. Blundell, "Comparison of Autonomous Lagrangian Circulation Explorer and fine resolution Antarctic model results in

the South Atlantic," *Journal of Geophysical Research*, vol. 101, pp. 855 884, 1996.

[8] H. Stommel, "The slocum mission," *Oceanography*, pp. 22 25, 1989.

[9] T. B. Curtin, J. G. Bellingham, J. Catipovic, and D.Webb, "Autonomous oceanographic sampling networks," *Oceanography*, vol. 6, pp. 86 94, 1993.

[10] D. Webb, P. Simonetti, and C. Jones, "Slocum: an underwater glider propelled by environmental energy," *Oceanic Engineering, IEEE Journal of*, vol. 26, pp. 447 452, Oct 2001.

[11] P. Simonetti, "Slocum glider: Design and 1991 field trials," tech. rep., Webb Research Corp., 1992.

[12] D. Webb and P. Simonetti, "A simpified approach to the prediction and optimization of performance of underwater gliders," in *Proc. of the 10th Symposium on Unmanned Untethered Submersible Technology in Durham, New Hampshire, USA*, 1997.

[13] E. Creed, J. Kerfoot, C. Mudgal, and H. Barrier, "Transition of slocum electric gliders to a sustained operational system," in *Proc. of IEEE Oceans*, vol. 2, pp. 828-833 Vol.2, Nov. 2004.

[14] J. Sherman, R. Davis, W. Owens, and J. Valdes, "The autonomous underwater glider "spray"," *Oceanic Engineering, IEEE Journal of*, vol. 26, pp. 437 446, Oct 2001.

[15] C. Eriksen, T. Osse, R. Light, T. Wen, T. Lehman, P. Sabin, J. Ballard, and A. Chiodi, "Seaglider: A long-range autonomous underwater vehicle for oceano-

graphic research," *Oceanic Engineering, IEEE Journal of*, vol. 26, no. 4, pp. 424–436, 2001.

[16] R. Davis, C. Eriksen, and C. Jones, *The Technology and Applications of Autonomous Underwater Vehicles*, ch. Autonomous buoyancy driven underwater gliders, pp. 37–58. Taylor and Francis, 2002.

[17] C. Eriksen, "Autonomous underwater gliders," tech. rep., Autonomous and Lagrangian Platforms and Sensors (ALPS) Workshop, Sea Lodge, La Jolla CA, 2003.

[18] D. Rudnick, R. Davis, C. Eriksen, D. Fratantoni, and M. Perry, "Underwater gliders for ocean research," *Marine Technology Society Journal*, vol. 38, pp. 73–84, 2004.

[19] G. Griffiths, C. Jones, J. Ferguson, and N. Bose, "Undersea gliders," *Journal of Ocean Technology*, vol. 2, no. 2, pp. 65–75, 2007.

[20] S. Jenkins, D. Humphreys, J. Sherman, J. Osse, C. Jones, N. Leonard, J. Graver, R. Bachmayer, T. Clem, P. Carroll, P. Davis, J. Berry, P. Berry, P. Worley, and J. Wasyl, *Underwater Glider System Study Technical Report 53*. Scripps Institution of Oceanography, 2003.

[21] K. Kawaguchi, T. Ura, Y. Tomoda, and H. Kobayashi, "Development and sea trials of a shuttle type auv "albac"," in *Proc. of the 8th Int. Symposium on Unmanned Untethered Submersible Tech.*, 1993.

[22] K. Kawaguchi, T. Ura, Y. Tomoda, and H. Kobayashi, "Development of a shuttle auv for oceanographic measurement," in *Proc. of the Conference for Pacific Ocean Environments and Probing (PORSEC) in Okinawa:*, 1992.

[23] C. Guo and N. Kato, "Mini underwater glider (mug) for education," in *the Workshop for Asian and Pacific Universities Underwater Roboticians (APuuRobo 2008)*, 2008.

[24] M. Arima, N. Ichihashi, and T. Ikebuchi, "Motion characteristics of an underwater glider with independently controllable main wings," in *Proc. Oceans - MTS/IEEE Kobe Techno-Ocean*, pp. 1–7, April 2008.

[25] M. Arima, N. Ichihashi, and Y. Miwa, "Modelling and motion simulation of an underwater glider with independently controllable main wings," in *Proc. Oceans-Europe.*, pp. 1–6, May 2009.

[26] J. Graver, J. Liu, C. Woolsey, and N. E. Leonard, "Design and analysis of an underwater vehicle for controlled gliding," in *Proc. 32nd Conference on Information Sciences and Systems*, pp. 801–806, 1998.

[27] N. E. Leonard, "Stability of a bottom-heavy underwater vehicle," *Automatica*, vol. 33, no. 3, pp. 331–346, 1997.

[28] N. Leonard and J. Graver, "Model-based feedback control of autonomous underwater gliders," *Oceanic Engineering, IEEE Journal of*, vol. 26, pp. 633–645, Oct 2001.

[29] J. G. Graver and N. E. Leonard., "Underwater glider dynamics and control," in *Proc. 12th Int. Symposium on Unmanned Untethered Submersible Tech., Durham, NH*, 2001.

[30] P. Bhatta and N. Leonard, "Stabilization and coordination of underwater gliders," in *Proc. of the 41st IEEE Conference on Decision and Control*, vol. 2, pp. 2081–2086, Dec. 2002.

[31] R. Bachmayer, J. Graver, and N. E. Leonard, "Glider control: A close look into the current glider controller structure and future developments," in *Proc. IEEE Oceans*, vol. 2, pp. 951 954, 2003.

[32] P. Bhatta, *Nonlinear Stability and Control of Gliding Vehicles*. PhD thesis, Princeton University, 2006.

[33] P. Bhatta and N. E. Leonard, "Nonlinear gliding stability and control for vehicles with hydrodynamic forcing," *Automatica*, vol. 44, no. 5, pp. 1240 1250, 2008.

[34] R. Moitie and N. Seube., "Guidance and control of an autonomous underwater glider," in *Proc. 12th Int. Symposium on Unmanned Untethered Submersible Tech., Durham, NH.*, 2001.

[35] S. Wood, T. Allan, S. Kuhn, and J. Caldwell, "The development of an autonomous underwater powered glider for deep-sea biological, chemical and physical oceanography," in *Proc. of IEEE Oceans - Aberdeen, Scotland*, 2007.

[36] A. Alvarez, A. Caffaz, A. Caiti, G. Casalino, E. Clerici, F. Giorgi, L. Gualdesi, A. Turetta, and R. Viviani, "Folaga: a very low cost autonomous underwater vehicle for coastal oceanography," in *Proc. 16th IFAC World Conference*, 2005.

[37] A. Alvarez, A. Caffaz, A. Caiti, G. Casalino, L. Gualdesi, A. Turetta, and R. Viviani, "Folaga: A low cost autonomous underwater vehicle combining glider and auv capabilities," *Ocean Engineering*, vol. 36, no. 1, pp. 24 38, 2009. Autonomous Underwater Vehicles.

[38] A. Caiti, A. Munafograve, and R. Viviani, "Adaptive on-line planning of environmental sampling missions with a team of cooperating autonomous underwater vehicles," *International Journal of Control*, vol. 80, pp. 1151 1168, July 2007.

[39] A. Caiti, G. Casalino, A. Munafo, and A. Turetta, "Cooperating auv teams: Adaptive area coverage with space-varying communication constraints," in *Proc. of Oceans - Europe*, pp. 1 7, May 2009.

[40] A. Alvarez, V. Bertram, and L. Gualdesi, "Hull hydrodynamic optimization of autonomous underwater vehicles operating at snorkeling depth," *Ocean Engineering*, vol. 36, no. 1, pp. 105 112, 2009. Autonomous Underwater Vehicles.

[41] Y. L. Page, "Innovative glider technologies," in *Everyones Gliding Observatories*, 2008.

[42] T. Swean, "Liberdade xray advanced underwater glider," tech. rep., Office of Naval Research, 2009.

[43] J. Geisbert, "Hydrodynamic modelling for autonomous underwater vehicles using computation and semi-emperical methods," Master's thesis, Virginia Polytechnic Institute and State University, 2007.

[44] R. Hine, G. Hine, and J. Manley, "The wave glider, a persistent platform for ocean science," in *Proc. of Everyone's Gliding Observatories, Cyprus*, 2009.

[45] C. R. Fralick and J. Manley, "The dart wave glider advanced technology demonstration results," in *Proc. of Everyone's Gliding Observatories, Cyprus*, 2009.

[46] E. Guizzo, "Defense contractors snap up submersible robot gliders," *IEEE Spectrum*, 2008.

[47] R. McGowan, "Teledyne wins 6.2m (52.6m with options) u.s. navy glider contract," tech. rep., Teledyne Technologies Incorporated, 2009.

[48] G. Griffiths, *Realtime Observation Systems for Ecosystem Dynamics and Harmful Algal Blooms*, ch. Gldier and autonomous underwater vehicle observing systems. UNESCO, 2005.

[49] C. Bishop, "Sensor dynamics of autonomous underwater gliders," Master's thesis, Memorial University of Newfoundland, 2008.

[50] M. S. M. P. Stevenson, "A concept design for an ultra-long-range survey class auv," in *Proc. of IEEE Oceans - Europe*, pp. 1 6, June 2007.

[51] S. McPhail, P. Stevenson, M. Pebody, and M. Furlong, "The nocs long range auv project," in *National Marine Facilities Department Seminar Series*, 2008.

[52] S. McPhail and G. Griffiths, "Autosub-long range, a deep-diving long range autonomous underwater vehicle," tech. rep., Nation Oceanography Center, Southampton, UK, 2009.

[53] D. Steinberg, A. Bender, and A. Friedman, "Toward selection of a propulsion method for a long range benthic imaging auv," in *Proc. 16th Int. Symp. on Unmanned Untethered Submersible Technology (UUST)*, 2009.

[54] B. Butler and V. D. Hertog, "Theseus: A cable-laying auv," in *Proc. of the 8th International Symposium on Unmanned Untether Submesible Technology*, 1993.

[55] J. Ferguson, "The theseus autonomous underwater vehicle. two successful missions," in *Proc. of the International Symposium on Underwater Technology*, pp. 109 114, 1998.

[56] J. Ferguson, "Adapting auvs for use in under-ice scientific missions," in *Proc. of IEEE Oceans*, pp. 1 5, 2008.

[57] J. Ferguson, "Under-ice seabed mapping with auvs," in *Proc. of Oceans - Europe*, pp. 1 6, 2009.

[58] D. Research and D. Canada, "Autonomous under-ice surveys for canadian arctic sovereignty: Project cornerstone." Fact Sheet No. MAP0809, 2009.

[59] P. Stevenson, N. W. Millard, S. D. McPhail, J. Riggs, D. White, M. Pebody, J. R. Perrett, and A. T. Webb, "Engineering an autonomous underwater vehicle for under ice operations," *ASME Conference Proceedings*, vol. 2003, no. 36835, pp. 445 452, 2003.

[60] M. Pebody, "Autonomous underwater vehicle collision avoidance for under-ice exploration," *Journal of Engineering for the Maritime Environment*, vol. 222, pp. 53 66, 2008.

[61] G. Griffiths, N. W. Millard, S. D. McPhail, P. Stevenson, and P. G. Challenor, "On the reliability of the autosub autonomous underwater vehicle," *Underwater Technology*, 2001.

[62] D. Shea, N. P. Riggs, R. Bachmayer, and C. Williams, "Preliminary testing of the prototype sqx-1 autonomous underwater vehicle," in *Proc. 16th Int. Symp. on Unmanned Untethered Submersible Technology (UUST)*, 2009.

[63] B. Claus, "Hybrid glider propulsion module implementation and characterization," in *Proc. 16th Int. Symp. on Unmanned Untethered Submersible Technology (UUST)*, 2009.

[64] B. Claus and R. Bachmayer, "Hybrid glider performance characterization," in *Proc. of Everyone's Gliding Observatories, Cyprus*, 2009.

[65] C. Bishop, B. de Young, and R. Bachmayer, "Autonomous underwater glider research at memorial university," *Journal of Ocean Technology*, vol. 4, no. 1, pp. 7–15, 2009.

[66] R. Bachmayer, B. de Young, and D. M. Holland, "Working towards ice profiling using underwater gliders: Operational experience in western greenland (69°13'17" n 51°5'40"w)," in *Proc. 15th Symposium on Unmanned Untethered Submersible Technology (UUST07) in Durham, New Hampshire, USA, August 19-22*, 2007.

[67] A. Bradley, "Low power navigation and control for long range autonomous underwater vehicles," in *Proc. of the Second International Offshore and Polar Engineering Conference, San Francisco, USA*, p. 473, International Society of Offshore and Polar Engineer (ISOPE), 1992.

[68] A. Bradley, M. Feezor, H. Singh, and F. Y. Sorrell, "Power systems for autonomous underwater vehicles," *Oceanic Engineering, IEEE Journal of*, vol. 26, pp. 526–538, Oct 2001.

[69] L. Merckelbach, R. Briggs, D. Smeed, and G. Griffiths, "Current measurements from autonomous underwater gliders," in *Proc. of the IEEE/OES 9th Working Conference on Current Measurement Technology*, pp. 61–67, March 2008.

[70] *Duracell Alkaline-Manganese Dioxide Battery MN1300 Size: D (LR20), Datasheet, June 2008.*

[71] *Maxon DC Motor Catalog, Maxon Motor, Manual, May 2010 edition.*

[72] K. D'Epagnier, H.-L. Chung, M. Stairway, and R. Kimball, "An open source parametric propeller design tool," in *Proc. of IEEE Oceans*, pp. 1–8, Oct. 2007.

[73] E. V. Lewis, *Principles of Naval Architecture, Resistance, Propulsion, and Vibration*, vol. II. The Society of Naval Architects and Marine Engineers, 2005.

[74] J. N. Newman, *Marine Hydrodynamics*. MIT Press: Cambridge MA, 1977

[75] H. Singh, D. Yoerger, and A. Bradley, "Issues in auv design and deployment for oceanographic research," in *Proc. of the IEEE International Conference on Robotics and Automation*, vol. 3, pp. 1857 1862, Apr 1997.

# Appendices

# Appendix A Propeller Comparison Script

```
%general constants
rho = 1000;              %water density [kg/m^3]
u_max = 15;              %maximum motor voltage [V]

%motor constants for REmax-17 4W 12V
k1_1=9.92*0.001;         %Nm/A
k2_1=962;                %rpm/V
k3_1=804*1000;           %rpm/Nm
i0_1=0.00738;            %A

%motor constants for REmax-16 2W 12V
k1_2=13.9*0.001;         %Nm/A
k2_2=685;                %rpm/V
k3_2=1640*1000;          %rpm/Nm
i0_2=0.00427;            %A

%motor constants for EC-16 15W 12V
k1_3=3.3*0.001;          %Nm/A
k2_3=2900;               %rpm/V
k3_3=1110*1000;          %rpm/Nm
i0_3=0.234;              %A

%motor constants for REmax-17 2.5W 12V
k1_4=16.3*0.001;         %Nm/A
k2_4=584;                %rpm/V
```

```
k3_4=825*1000;          %rpm/Nm
i0_4=0.00645;           %A

%motor constants for RE-16 3.2W 12V
k1_5=19*0.001;          %Nm/A
k2_5=502;               %rpm/V
k3_5=404*1000;          %rpm/Nm
i0_5=0.00463;           %A

%motor constants for A-max 16 2W 12V
k1_6=9.17*0.001;        %Nm/A
k2_6=1040;              %rpm/V
k3_6=2620*1000;         %rpm/Nm
i0_6=0.00954;           %A

%motor constants for A-max 16 1.2W 12V
k1_7=10.7*0.001;        %Nm/A
k2_7=893;               %rpm/V
k3_7=2600*1000;         %rpm/Nm
i0_7=0.00969;           %A

%motor constants for A-max 16 1.2W 12V
k1_8=8.23*0.001;        %Nm/A
k2_8=1160;              %rpm/V
k3_8=2320*1000;         %rpm/Nm
i0_8=0.0488;            %A
```

```
%gearbox parameters for GP 16 A
R_1=29;
Reff_1=0.81;

R_2=24;
Reff_2=0.81;

R_3=84;
Reff_3=0.73;

R_4=5.4;
Reff_4=0.90;

%propeller parameters
kq = 0.011;      %torque coefficient
dp = 0.225; %propeller diameter

 %rpm from propeller
omega_prop = (60/(2*pi())).*[41.6215461030311; 83.2430912038465; ...
    54.3535671407506; 28.9490283296888; 21.3758770260448; ...
    17.1676114196556; 14.4260665463082; 12.4851624495464; ...
    11.0368662088487; 9.91608570148360; 9.02568829075550; ...
    8.30398417368966; 7.71012397973262; 7.21600581502827; ...
    6.80116624938808; 6.45079493080424; 6.15369272828412; ...
    5.90126614760881; 5.68680710283808; 5.50500005229578; ...
    5.35157676168959; 5.22324829077582; 5.11690694045159; ...
    5.03030643063675; 4.96147808697379]';
```

```
%efficiencct from propeller
eta_prop = [NaN;NaN;0.549021561695221;0.773121382606497;...
    0.837622560398599;0.869128611712548;0.886536595360214;...
    0.896310380190165;0.901268836447632;0.902816507594973;...
    0.901715703283965;0.898409617882835;0.893169214523670;...
    0.886171427920010;0.877542133303100;0.867379806698027;...
    0.855770868599157;0.842798587303946;0.828548458146559;...
    0.813111180128276;0.796583978693364;0.779075073569666;...
    0.760689303504456;0.741544104505675;0.721757979115252]';
tau_prop = kq.*rho.*(omega_prop./60).^2.*dp.^5;
p_prop = omega_prop.*tau_prop.*(2*pi()/60);

%with gearbox 1
omega_m_1 = omega_prop.*R_1;
tau_m_1 = (tau_prop./(R_1.*Reff_1));
u_m_1 = (omega_m_1+k3_1.*tau_m_1)./k2_1;
i_m_1 = tau_m_1./k1_1 + i0_1;
p_m_1 = u_m_1.*i_m_1;
eta_m_1 = Reff_1.*(tau_m_1.*omega_m_1.*(2*pi()/60))./(p_m_1);
eta_sys_1 = eta_prop.*eta_m_1;

omega_m_2 = omega_prop.*R_1;
tau_m_2 = (tau_prop./(R_1.*Reff_1));
u_m_2 = (omega_m_2+k3_2.*tau_m_2)./k2_2;
i_m_2 = tau_m_2./k1_2 + i0_2;
p_m_2 = u_m_2.*i_m_2;
eta_m_2 = Reff_1.*(tau_m_2.*omega_m_2.*(2*pi()/60))./(p_m_2);
```

```
eta_sys_2 = eta_prop.*eta_m_2;

omega_m_3 = omega_prop.*R_1;
tau_m_3 = (tau_prop./(R_1.*Reff_1));
u_m_3 = (omega_m_3+k3_3.*tau_m_3)./k2_3;
i_m_3 = tau_m_3./k1_3 + i0_3;
p_m_3 = u_m_3.*i_m_3;
eta_m_3 = Reff_1.*(tau_m_3.*omega_m_3.*(2*pi()/60))./(p_m_3);
eta_sys_3 = eta_prop.*eta_m_3;

omega_m_4 = omega_prop.*R_1;
tau_m_4 = (tau_prop./(R_1.*Reff_1));
u_m_4 = (omega_m_4+k3_4.*tau_m_4)./k2_4;
i_m_4 = tau_m_4./k1_4 + i0_4;
p_m_4 = u_m_4.*i_m_4;
eta_m_4 = Reff_1.*(tau_m_4.*omega_m_4.*(2*pi()/60))./(p_m_4);
eta_sys_4 = eta_prop.*eta_m_4;

omega_m_5 = omega_prop.*R_1;
tau_m_5 = (tau_prop./(R_1.*Reff_1));
u_m_5 = (omega_m_5+k3_5.*tau_m_5)./k2_5;
i_m_5 = tau_m_5./k1_5 + i0_5;
p_m_5 = u_m_5.*i_m_5;
eta_m_5 = Reff_1.*(tau_m_5.*omega_m_5.*(2*pi()/60))./(p_m_5);
eta_sys_5 = eta_prop.*eta_m_5;

omega_m_6 = omega_prop.*R_1;
```

```
tau_m_6 = (tau_prop./(R_1.*Reff_1));
u_m_6 = (omega_m_6+k3_6.*tau_m_6)./k2_6;
i_m_6 = tau_m_6./k1_6 + i0_6;
p_m_6 = u_m_6.*i_m_6;
eta_m_6 = Reff_1.*(tau_m_6.*omega_m_6.*(2*pi()/60))./(p_m_6);
eta_sys_6 = eta_prop.*eta_m_6;

omega_m_7 = omega_prop.*R_1;
tau_m_7 = (tau_prop./(R_1.*Reff_1));
u_m_7 = (omega_m_7+k3_7.*tau_m_7)./k2_7;
i_m_7 = tau_m_7./k1_7 + i0_7;
p_m_7 = u_m_7.*i_m_7;
eta_m_7 = Reff_1.*(tau_m_7.*omega_m_7.*(2*pi()/60))./(p_m_7);
eta_sys_7 = eta_prop.*eta_m_7;

omega_m_8 = omega_prop.*R_1;
tau_m_8 = (tau_prop./(R_1.*Reff_1));
u_m_8 = (omega_m_8+k3_8.*tau_m_8)./k2_8;
i_m_8 = tau_m_8./k1_8 + i0_8;
p_m_8 = u_m_8.*i_m_8;
eta_m_8 = Reff_1.*(tau_m_8.*omega_m_8.*(2*pi()/60))./(p_m_8);
eta_sys_8 = eta_prop.*eta_m_8;

j1= find(u_m_1 <15);
j2= find(u_m_2 <15);
j3= find(u_m_3 <15);
j4= find(u_m_4 <15);
```

```
j5= find(u_m_5 <15);
j6= find(u_m_6 <15);
j7= find(u_m_7 <15);
j8= find(u_m_8 <15);

figure
h = axes;
set(h,'FontName','Arial','fontsize',12,'LineWidth',1);
plot(omega_prop(j1:25),eta_m_1(j1:25).*100, '-b', 'LineWidth', 1)
hold on
plot(omega_prop(j2:25),eta_m_2(j2:25).*100, '-r', 'LineWidth', 1)
plot(omega_prop(j3:25),eta_m_3(j3:25).*100, '-g', 'LineWidth', 1)
plot(omega_prop(j4:25),eta_m_4(j4:25).*100, '-m', 'LineWidth', 1)
plot(omega_prop(j5:25),eta_m_5(j5:25).*100, '-.b', 'LineWidth', 1)
plot(omega_prop(j6:25),eta_m_6(j6:25).*100, '-.r', 'LineWidth', 1)
plot(omega_prop(j7:25),eta_m_7(j7:25).*100, '-.g', 'LineWidth', 1)
plot(omega_prop(j8:25),eta_m_8(j8:25).*100, '-.m', 'LineWidth', 1)
plot(omega_prop,eta_prop.*100, '--k', 'LineWidth', 1)
xlabel('\Omega [RPM]'),ylabel('Efficiency [%]')
legend('\eta_{m1} \eta_{gb1}','\eta_{m2} \eta_{gb1}'...
,'\eta_{m3} \eta_{gb1}','\eta_{m4} \eta_{gb1}'...
,'\eta_{m5} \eta_{gb1}','\eta_{m6} \eta_{gb1}'...
,'\eta_{m7} \eta_{gb1}','\eta_{m8} \eta_{gb1}'...
,'\eta_{prop}','Location','SouthEast')
axis([0 450 0 100])
grid on, box on
set(h,'LineWidth',1);
```

```
print -depsc motoreffgb1

%gearbox 2
omega_m_9 = omega_prop.*R_2;
tau_m_9 = (tau_prop./(R_2.*Reff_2));
u_m_9 = (omega_m_9+k3_1.*tau_m_9)./k2_1;
i_m_9 = tau_m_9./k1_1 + i0_1;
p_m_9 = u_m_9.*i_m_9;
eta_m_9 = Reff_2.*(tau_m_9.*omega_m_9.*(2*pi()/60))./(p_m_9);
eta_sys_9 = eta_prop.*eta_m_9;

omega_m_10 = omega_prop.*R_2;
tau_m_10 = (tau_prop./(R_2.*Reff_2));
u_m_10 = (omega_m_10+k3_2.*tau_m_10)./k2_2;
i_m_10 = tau_m_10./k1_2 + i0_2;
p_m_10 = u_m_10.*i_m_10;
eta_m_10 = Reff_2.*(tau_m_10.*omega_m_10.*(2*pi()/60))./(p_m_10);
eta_sys_10 = eta_prop.*eta_m_10;

omega_m_11 = omega_prop.*R_2;
tau_m_11 = (tau_prop./(R_2.*Reff_2));
u_m_11 = (omega_m_11+k3_3.*tau_m_11)./k2_3;
i_m_11 = tau_m_11./k1_3 + i0_3;
p_m_11 = u_m_11.*i_m_11;
eta_m_11 = Reff_2.*(tau_m_11.*omega_m_11.*(2*pi()/60))./(p_m_11);
eta_sys_11 = eta_prop.*eta_m_11;
```

```
omega_m_12 = omega_prop.*R_2;
tau_m_12 = (tau_prop./(R_2.*Reff_2));
u_m_12 = (omega_m_12+k3_4.*tau_m_12)./k2_4;
i_m_12 = tau_m_12./k1_4 + i0_4;
p_m_12 = u_m_12.*i_m_12;
eta_m_12 = Reff_2.*(tau_m_12.*omega_m_12.*(2*pi()/60))./(p_m_12);
eta_sys_12 = eta_prop.*eta_m_12;

omega_m_13 = omega_prop.*R_2;
tau_m_13 = (tau_prop./(R_2.*Reff_2));
u_m_13 = (omega_m_13+k3_5.*tau_m_13)./k2_5;
i_m_13 = tau_m_13./k1_5 + i0_5;
p_m_13 = u_m_13.*i_m_13;
eta_m_13 = Reff_2.*(tau_m_13.*omega_m_13.*(2*pi()/60))./(p_m_13);
eta_sys_13 = eta_prop.*eta_m_13;

omega_m_14 = omega_prop.*R_2;
tau_m_14 = (tau_prop./(R_2.*Reff_2));
u_m_14 = (omega_m_14+k3_6.*tau_m_14)./k2_6;
i_m_14 = tau_m_14./k1_6 + i0_6;
p_m_14 = u_m_14.*i_m_14;
eta_m_14 = Reff_2.*(tau_m_14.*omega_m_14.*(2*pi()/60))./(p_m_14);
eta_sys_14 = eta_prop.*eta_m_14;

omega_m_15 = omega_prop.*R_2;
tau_m_15 = (tau_prop./(R_2.*Reff_2));
u_m_15 = (omega_m_15+k3_7.*tau_m_15)./k2_7;
```

```
i_m_15 = tau_m_15./k1_7 + i0_7;
p_m_15 = u_m_15.*i_m_15;
eta_m_15 = Reff_2.*(tau_m_15.*omega_m_15.*(2*pi()/60))./(p_m_15);
eta_sys_15 = eta_prop.*eta_m_15;

omega_m_16 = omega_prop.*R_2;
tau_m_16 = (tau_prop./(R_2.*Reff_2));
u_m_16 = (omega_m_16+k3_8.*tau_m_16)./k2_8;
i_m_16 = tau_m_16./k1_8 + i0_8;
p_m_16 = u_m_16.*i_m_16;
eta_m_16 = Reff_2.*(tau_m_16.*omega_m_16.*(2*pi()/60))./(p_m_16);
eta_sys_16 = eta_prop.*eta_m_16;

j9= find(u_m_9 <15);
j10= find(u_m_10 <15);
j11= find(u_m_11 <15);
j12= find(u_m_12 <15);
j13= find(u_m_13 <15);
j14= find(u_m_14 <15);
j15= find(u_m_15 <15);
j16= find(u_m_16 <15);

figure
h = axes;
set(h,'FontName','Arial','fontsize',12,'LineWidth',1);
plot(omega_prop(j9:25),eta_m_9(j9:25).*100, '-b', 'LineWidth', 1)
hold on
```

```
plot(omega_prop(j10:25),eta_m_10(j10:25).*100, '-r', 'LineWidth', 1)
plot(omega_prop(j11:25),eta_m_11(j11:25).*100, '-g', 'LineWidth', 1)
plot(omega_prop(j12:25),eta_m_12(j12:25).*100, '-m', 'LineWidth', 1)
plot(omega_prop(j13:25),eta_m_13(j13:25).*100, '-.b', 'LineWidth', 1)
plot(omega_prop(j14:25),eta_m_14(j14:25).*100, '-.r', 'LineWidth', 1)
plot(omega_prop(j15:25),eta_m_15(j15:25).*100, '-.g', 'LineWidth', 1)
plot(omega_prop(j16:25),eta_m_16(j16:25).*100, '-.m', 'LineWidth', 1)
plot(omega_prop,eta_prop.*100, '--k', 'LineWidth', 1)
xlabel('\Omega [RPM]'),ylabel('Efficiency [%]')
legend('\eta_{m1} \eta_{gb2}','\eta_{m2} \eta_{gb2}'...
    ,'\eta_{m3} \eta_{gb2}','\eta_{m4} \eta_{gb2}'...
    ,'\eta_{m5} \eta_{gb2}','\eta_{m6} \eta_{gb2}'...
    ,'\eta_{m7} \eta_{gb2}','\eta_{m8} \eta_{gb2}'...
    ,'\eta_{prop}','Location','SouthEast')
axis([0 450 0 100])
grid on, box on
set(h,'LineWidth',1);
print -depsc motoreffgb2

%gearbox 2
omega_m_17 = omega_prop.*R_3;
tau_m_17 = (tau_prop./(R_3.*Reff_3));
u_m_17 = (omega_m_17+k3_1.*tau_m_17)./k2_1;
i_m_17 = tau_m_17./k1_1 + i0_1;
p_m_17 = u_m_17.*i_m_17;
eta_m_17 = Reff_3.*(tau_m_17.*omega_m_17.*(2*pi()/60))./(p_m_17);
eta_sys_17 = eta_prop.*eta_m_17;
```

```
omega_m_18 = omega_prop.*R_3;
tau_m_18 = (tau_prop./(R_3.*Reff_3));
u_m_18 = (omega_m_18+k3_2.*tau_m_18)./k2_2;
i_m_18 = tau_m_18./k1_2 + i0_2;
p_m_18 = u_m_18.*i_m_18;
eta_m_18 = Reff_3.*(tau_m_18.*omega_m_18.*(2*pi()/60))./(p_m_18);
eta_sys_18 = eta_prop.*eta_m_18;

omega_m_19 = omega_prop.*R_3;
tau_m_19 = (tau_prop./(R_3.*Reff_3));
u_m_19 = (omega_m_19+k3_3.*tau_m_19)./k2_3;
i_m_19 = tau_m_19./k1_3 + i0_3;
p_m_19 = u_m_19.*i_m_19;
eta_m_19 = Reff_3.*(tau_m_19.*omega_m_19.*(2*pi()/60))./(p_m_19);
eta_sys_19 = eta_prop.*eta_m_19;

omega_m_20 = omega_prop.*R_3;
tau_m_20 = (tau_prop./(R_3.*Reff_3));
u_m_20 = (omega_m_20+k3_4.*tau_m_20)./k2_4;
i_m_20 = tau_m_20./k1_4 + i0_4;
p_m_20 = u_m_20.*i_m_20;
eta_m_20 = Reff_3.*(tau_m_20.*omega_m_20.*(2*pi()/60))./(p_m_20);
eta_sys_20 = eta_prop.*eta_m_20;

omega_m_21 = omega_prop.*R_3;
tau_m_21 = (tau_prop./(R_3.*Reff_3));
```

```
u_m_21 = (omega_m_21+k3_5.*tau_m_21)./k2_5;
i_m_21 = tau_m_21./k1_5 + i0_5;
p_m_21 = u_m_21.*i_m_21;
eta_m_21 = Reff_3.*(tau_m_21.*omega_m_21.*(2*pi()/60))./(p_m_21);
eta_sys_21 = eta_prop.*eta_m_21;

omega_m_22 = omega_prop.*R_3;
tau_m_22 = (tau_prop./(R_3.*Reff_3));
u_m_22 = (omega_m_22+k3_6.*tau_m_22)./k2_6;
i_m_22 = tau_m_22./k1_6 + i0_6;
p_m_22 = u_m_22.*i_m_22;
eta_m_22 = Reff_3.*(tau_m_22.*omega_m_22.*(2*pi()/60))./(p_m_22);
eta_sys_22 = eta_prop.*eta_m_22;

omega_m_23 = omega_prop.*R_3;
tau_m_23 = (tau_prop./(R_3.*Reff_3));
u_m_23 = (omega_m_23-k3_7.*tau_m_23)./k2_7;
i_m_23 = tau_m_23./k1_7 + i0_7;
p_m_23 = u_m_23.*i_m_23;
eta_m_23 = Reff_3.*(tau_m_23.*omega_m_23.*(2*pi()/60))./(p_m_23);
eta_sys_23 = eta_prop.*eta_m_23;

omega_m_24 = omega_prop.*R_3;
tau_m_24 = (tau_prop./(R_3.*Reff_3));
u_m_24 = (omega_m_24+k3_8.*tau_m_24)./k2_8;
i_m_24 = tau_m_24./k1_8 + i0_8;
p_m_24 = u_m_24.*i_m_24;
```

```
eta_m_24 = Reff_3.*(tau_m_24.*omega_m_24.*(2*pi()/60))./(p_m_24);
eta_sys_24 = eta_prop.*eta_m_24;

j17= find(u_m_17 <15);
j18= find(u_m_18 <15);
j19= find(u_m_19 <15);
j20= find(u_m_20 <15);
j21= find(u_m_21 <15);
j22= find(u_m_22 <15);
j23= find(u_m_23 <15);
j24= find(u_m_24 <15);

figure
h = axes;
set(h,'FontName','Arial','fontsize',12,'LineWidth',1);
plot(omega_prop(j17:25),eta_m_17(j17:25).*100, '-b', 'LineWidth', 1)
hold on
plot(omega_prop(j18:25),eta_m_18(j18:25).*100, '-r', 'LineWidth', 1)
plot(omega_prop(j19:25),eta_m_19(j19:25).*100, '-g', 'LineWidth', 1)
plot(omega_prop(j20:25),eta_m_20(j20:25).*100, '-m', 'LineWidth', 1)
plot(omega_prop(j21:25),eta_m_21(j21:25).*100, '-.b', 'LineWidth', 1)
plot(omega_prop(j22:25),eta_m_22(j22:25).*100, '-.r', 'LineWidth', 1)
plot(omega_prop(j23:25),eta_m_23(j23:25).*100, '-.g', 'LineWidth', 1)
plot(omega_prop(j24:25),eta_m_24(j24:25).*100, '-.m', 'LineWidth', 1)
plot(omega_prop,eta_prop.*100, '--k', 'LineWidth', 1)
xlabel('\Omega [RPM]'),ylabel('Efficiency [%]')
legend('\eta_{m1} \eta_{gb3}','\eta_{m2} \eta_{gb3}'...
```

```
    ,'\eta_{m3} \eta_{gb3}','\eta_{m4} \eta_{gb3}'...
    ,'\eta_{m5} \eta_{gb3}','\eta_{m6} \eta_{gb3}'...
    ,'\eta_{m7} \eta_{gb3}','\eta_{m8} \eta_{gb3}'...
    ,'\eta_{prop}','Location','SouthEast')
axis([0 450 0 100])
grid on, box on
set(h,'LineWidth',1);
print -depsc motoreffgb3

%gearbox 2
omega_m_25 = omega_prop.*R_4;
tau_m_25 = (tau_prop./(R_4.*Reff_4));
u_m_25 = (omega_m_25+k3_1.*tau_m_25)./k2_1;
i_m_25 = tau_m_25./k1_1 + i0_1;
p_m_25 = u_m_25.*i_m_25;
eta_m_25 = Reff_4.*(tau_m_25.*omega_m_25.*(2*pi()/60))./(p_m_25);
eta_sys_25 = eta_prop.*eta_m_25;

omega_m_26 = omega_prop.*R_4;
tau_m_26 = (tau_prop./(R_4.*Reff_4));
u_m_26 = (omega_m_26+k3_2.*tau_m_26)./k2_2;
i_m_26 = tau_m_26./k1_2 + i0_2;
p_m_26 = u_m_26.*i_m_26;
eta_m_26 = Reff_4.*(tau_m_26.*omega_m_26.*(2*pi()/60))./(p_m_26);
eta_sys_26 = eta_prop.*eta_m_26;

omega_m_27 = omega_prop.*R_4;
```

```
tau_m_27 = (tau_prop./(R_4.*Reff_4));
u_m_27 = (omega_m_27+k3_3.*tau_m_27)./k2_3;
i_m_27 = tau_m_27./k1_3 + i0_3;
p_m_27 = u_m_27.*i_m_27;
eta_m_27 = Reff_4.*(tau_m_27.*omega_m_27.*(2*pi()/60))./(p_m_27);
eta_sys_27 = eta_prop.*eta_m_27;

omega_m_28 = omega_prop.*R_4;
tau_m_28 = (tau_prop./(R_4.*Reff_4));
u_m_28 = (omega_m_28+k3_4.*tau_m_28)./k2_4;
i_m_28 = tau_m_28./k1_4 + i0_4;
p_m_28 = u_m_28.*i_m_28;
eta_m_28 = Reff_4.*(tau_m_28.*omega_m_28.*(2*pi()/60))./(p_m_28);
eta_sys_28 = eta_prop.*eta_m_28;

omega_m_29 = omega_prop.*R_4;
tau_m_29 = (tau_prop./(R_4.*Reff_4));
u_m_29 = (omega_m_29+k3_5.*tau_m_29)./k2_5;
i_m_29 = tau_m_29./k1_5 + i0_5;
p_m_29 = u_m_29.*i_m_29;
eta_m_29 = Reff_4.*(tau_m_29.*omega_m_29.*(2*pi()/60))./(p_m_29);
eta_sys_29 = eta_prop.*eta_m_29;

omega_m_30 = omega_prop.*R_4;
tau_m_30 = (tau_prop./(R_4.*Reff_4));
u_m_30 = (omega_m_30+k3_6.*tau_m_30)./k2_6;
i_m_30 = tau_m_30./k1_6 + i0_6;
```

```
p_m_30 = u_m_30.*i_m_30;
eta_m_30 = Reff_4.*(tau_m_30.*omega_m_30.*(2*pi()/60))./(p_m_30);
eta_sys_30 = eta_prop.*eta_m_30;

omega_m_31 = omega_prop.*R_4;
tau_m_31 = (tau_prop./(R_4.*Reff_4));
u_m_31 = (omega_m_31+k3_7.*tau_m_31)./k2_7;
i_m_31 = tau_m_31./k1_7 + i0_7;
p_m_31 = u_m_31.*i_m_31;
eta_m_31 = Reff_4.*(tau_m_31.*omega_m_31.*(2*pi()/60))./(p_m_31);
eta_sys_31 = eta_prop.*eta_m_31;

omega_m_32 = omega_prop.*R_4;
tau_m_32 = (tau_prop./(R_4.*Reff_4));
u_m_32 = (omega_m_32+k3_8.*tau_m_32)./k2_8;
i_m_32 = tau_m_32./k1_8 + i0_8;
p_m_32 = u_m_32.*i_m_32;
eta_m_32 = Reff_4.*(tau_m_32.*omega_m_32.*(2*pi()/60))./(p_m_32);
eta_sys_32 = eta_prop.*eta_m_32;

j25= find(u_m_25 <15);
j26= find(u_m_26 <15);
j27= find(u_m_27 <15);
j28= find(u_m_28 <15);
j29= find(u_m_29 <15);
j30= find(u_m_30 <15);
j31= find(u_m_31 <15);
```

```
j32= find(u_m_32 <15);

figure
h = axes;
set(h,'FontName','Arial','fontsize',12,'LineWidth',1);
plot(omega_prop(j25:25),eta_m_25(j25:25).*100, '-b', 'LineWidth', 1)
hold on
plot(omega_prop(j26:25),eta_m_26(j26:25).*100, '-r', 'LineWidth', 1)
plot(omega_prop(j27:25),eta_m_27(j27:25).*100, '-g', 'LineWidth', 1)
plot(omega_prop(j28:25),eta_m_28(j28:25).*100, '-m', 'LineWidth', 1)
plot(omega_prop(j29:25),eta_m_29(j29:25).*100, '-.b', 'LineWidth', 1)
plot(omega_prop(j30:25),eta_m_30(j30:25).*100, '-.r', 'LineWidth', 1)
plot(omega_prop(j31:25),eta_m_31(j31:25).*100, '-.g', 'LineWidth', 1)
plot(omega_prop(j32:25),eta_m_32(j32:25).*100, '-.m', 'LineWidth', 1)
plot(omega_prop,eta_prop.*100, '--k', 'LineWidth', 1)
xlabel('\Omega [RPM]'),ylabel('Efficiency [%]')
legend('\eta_{m1} \eta_{gb4}','\eta_{m2} \eta_{gb4}'...
    ,'\eta_{m3} \eta_{gb4}','\eta_{m4} \eta_{gb4}'...
    ,'\eta_{m5} \eta_{gb4}','\eta_{m6} \eta_{gb4}'...
    ,'\eta_{m7} \eta_{gb4}','\eta_{m8} \eta_{gb4}'...
    ,'\eta_{prop}','Location','SouthEast')
axis([0 450 0 100])
grid on, box on
set(h,'LineWidth',1);
print -depsc motoreffgb4
```

# Appendix B Power Monitor Schematic

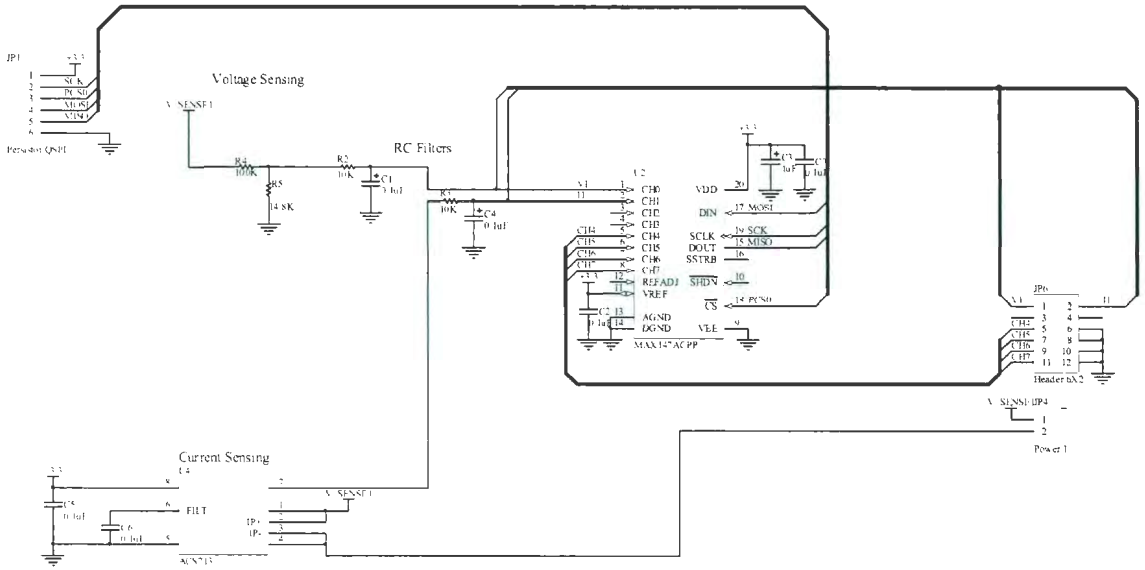
Voltage Sensing
RC Filters
Current Sensing
MAX147ACPP
Header 6X2
Power 1
GLIDER POWER MONITOR
Size
Number
Revision
REV 4
Legal
Date: 10/06/2010
Sheet of
File: C:\Documents and Settings\...\power_monitor.SCHDOC
CLAUS